Arjan Çiftja

Solar silicon refining; Inclusions, settling, filtration, wetting

Thesis for the degree of Philosophiae Doctor

Trondheim, February 2009

Norwegian University of Science and Technology
Faculty of Natural Sciences and Technology
Department of Materials Science and Engineering

NTNU
Norwegian University of
Science and Technology

Preface

This work was carried out at Department of Materials Science and Engineering of the Norwegian University of Science and Technology between January 2006 and January 2009. The first two years of the research had no founding and the financial support of the author was provided by Lånekassen as a student scholarship under "Quota Program". Department of Materials Science and Engineering of NTNU contributed with the equipment and analyzing techniques.

The last year was part of the research project "ThermoTech" funded by Research Council of Norway. The 2 month research study on removal of SiC particles by settling was financed by SINTEF Materials and Chemistry as a part of the Foxy project.

Filtration of solar cell silicon scrap was the starting point of this study. Preliminary research on this field was carried out in 2005 during a Master study where I served as technical supervisor. The promising results obtained paved the path to carry out successful experimental and theoretical research. The top-cut silicon scrap and the pure poly-crystalline silicon were donated by Rec-Scan Wafer, while the C and SiC filters were supplied by Foseco AB and Eger-Sørensen.

For this work the following honors have been received:

1. **TMS 2009 Young Leader Professional Development Award** in Light Metals, TMS Society, USA.

2. **Graduate Student Award** – 18th Workshop on Crystalline Silicon Solar Cells & Modules: Materials and Processes, August 2008, NREL, Colorado, USA.

3. **Dr.ing. Haakon Styri's Studiefond** for qualified researchers in the field of materials science, April 2008, Trondheim, Norway.

Acknowledgements

I am deeply grateful to my supervisors Prof. Merete Tangstad and Prof. Thorvald Abel Engh for the successful guidance, useful suggestions and fruitful discussions. I would like to profoundly thank them for introducing me to materials science and giving me the chance to work in this field.

I would like to thank Anne Kvithyld for all the precious help that she provided during my thesis. Her cooperation was most appreciated and I learned much from her experience in the field. Sean Gaal is thanked for all the technical help with the equipment employed in the thesis. I am grateful to Arlinda Fejzo (Ciftja) for taking over much of the microscopic analysis for obtaining the particle size distributions and to Eivind J. Øvrelid for conducting the settling experiments.

Many thanks go to the NTNU staff for the valuable support especially to Jan Arve Baatnes and to Pål Ulseth for always being available throughout my study. SINTEF colleagues are appreciated for the cooperation and consideration that they showed towards my work. Jorunn Voje and Elkem Aluminum are acknowledged for their interest and support.

I would like to thank all my friends of the SiManTiAl "gang" for the wonderful time we spent together.

Last but not least I am very grateful and obliged to my parents, my dear Lina and my "lille" ILIRA. They are my motivation and inspiration for every achievement.

Trondheim, January, 2009

Arjan Çiftja

List of Publications

Reports

1. A. Ciftja, T. A. Engh, M. Tangstad, *Refining and Recycling of Silicon: A Review*, NTNU report, Trondheim, February 2008. 40 pages, ISBN: 978-82-997357-2-8.

2. A. Ciftja, M. Tangstad, T. A. Engh, *Wettability of Silicon with Refractory Materials: A Review*, NTNU report, Trondheim, February 2008, 37 pages. ISBN: 978-82-997357-1-1.

Conference papers

1. Arjan Ciftja, Merete Tangstad, Thorvald Abel Engh, *Wetting properties of molten silicon with graphite materials*, to be published at 24th European Photovoltaic Solar Energy Conference, September 21-25, 2009, Hamburg, Germany.

2. Arjan Ciftja, Thorvald Abel Engh, Merete Tangstad, *Filtration with foam filters*, to be published at the 3rd International Workshop on Crystalline Silicon Solar Cells, June 3-5, 2009, Trondheim, Norway.

3. Arjan Ciftja, Eivind J. Øvrelid, Merete Tangstad, Thorvald Abel Engh, Arlinda Fejzo, *Settling of particles in molten silicon before directional casting of a solar grade silicon ingot*, Solar Cell Silicon: Production and Recycling, Supplemental Proceedings, Volume 2, TMS 2009, pp.261-268.

4. Arjan Ciftja, Thorvald Abel Engh, Merete Tangstad, Anne Kvithyld, *Recycling of silicon scrap by filtration*, Proceedings of the 23rd European Photovoltaic Solar Energy Conference, 1-5 September 2008, Valencia, Spain, pp.1274-1277.

5. Arjan Ciftja, Thorvald Abel Engh, Merete Tangstad, Anne Kvithyld, *Recycling of silicon scrap by filtration*, Proceedings of 18th Workshop on Crystalline Silicon Solar Cells & Modules: Materials and Processes, 2008, August 3 – 6, Vail, CO, USA, pp.101-104.

6. Arjan Ciftja, Eivind J. Øvrelid, Merete Tangstad, Thorvald Abel Engh, *Settling of solid particles in molten silicon as a refining step from metallurgical grade to solar grade silicon*, Proceedings of the Third Nordic Symposium for Young Scientists in Metallurgy, 2008, May 13 – 15, Espoo, Finland, Vol.1, pp.77-81. ISBN: 978-951-22-9495-4.

7. L. Zhang, A. Ciftja, L. Damoah, *Removal of non-metallic inclusions from molten aluminum*, Proceedings of EMC (European Metallurgical Conference) 2007, June 11 - 14, Dusseldorf, Germany, Vol.3, pp.1413-1424.

8. A. Ciftja, L. Zhang, T. A. Engh, *Removal of SiC and Si_3N_4 particles from silicon scrap by foam filters*, Recycling and Waste Processing, TMS annual meeting 2007, Orlando, FL., 67-76.

9. A. Ciftja, A. Kvithyld, L. Zhang, T.A. Engh, *Removal of inclusions from silicon by filtration*, Silicon for the chemical industry VIII, Trondheim, Norway, 2006, pp.63-70.

10. A. Kvithyld, D. Chithambaranadhan, A. Ciftja, E. Øvrelid, T. A. Engh, *Filtration of solar cell silicon scrap*. EDP Congress 2006, TMS annual meeting 2006, March, pp.919-928.

Peer review journals

1. Arjan Ciftja, Thorvald Abel Engh, Merete Tangstad, *A model of foam filters*, to be published at Metallurgical and Materials Transactions B.

2. Arjan Ciftja, Merete Tangstad, Thorvald Abel Engh, *Removal of inclusions from silicon*, to be published at JOM, November 2009.

3. Arjan Ciftja, Merete Tangstad, Thorvald Abel Engh, *Investigation on settling, pushing and engulfment of SiC particles in molten silicon*, to be published at Metallurgical and Materials Transactions B.

4. Arjan Ciftja, Merete Tangstad, Thorvald Abel Engh, *Wettability of molten silicon with graphite refractories; selection of materials for usage in PV industry*, to be published at Journal of Solar Energy Materials & Solar Cells, 2009.

5. L. Zhang, A. Ciftja, *Recycling of Solar Cell Silicon Scraps through Filtration, Part I: Experimental Investigation*, Solar Energy Materials & Solar Cells 92, 2008, pp 1450-1461.

6. A. Ciftja, L. Zhang, T. A. Engh, A. Kvithyld, *Purification of Solar Cell Silicon Materials Through Filtration*, Rare Metals, Vol.25, Special issue, June, 2006, pp.180-185.

Summary

The main objective of the present work is the removal of inclusions from silicon scrap and metallurgical grade silicon. To reach this goal, two various routes are investigated. First, settling of SiC particles from molten silicon followed by directional solidification is reported in this thesis. Then, removal of SiC and Si_3N_4 inclusions in silicon scrap by filtration with foam filters and wettabilities of silicon on graphite materials are studied.

To supply the increasing needs of the photovoltaic industry it is necessary to produce a low cost silicon feedstock. One of the many routes established from the industry is the Solsilc project. This project aims to produce solar-grade silicon by carbothermal reduction of silicon, based on the use of very pure raw materials. The high carbon content of about 700 mass ppm of the silicon in the form of SiC particles, needs to be removed before the Solsilc silicon could be used as a feedstock to PV industry. Settling of SiC particles in molten silicon was investigated. This part of the work was in cooperation with SINTEF Materials & Chemistry. Two experiments were conducted and the cast silicon ingots were analyzed by light microscopy and LECO carbon analyzer. The results showed that the number of inclusions in the middle of the ingots was less than in the bottom and top. The removal efficiency was above 96% in the middle part of an ingot and the total carbon content measured by LECO was < 25 mass ppm. The difference in density between the particles and the melt gives the SiC particles a relatively high settling velocity leading to a high removal efficiency. Pushing and engulfment of SiC particles by solidification front was also studied. Directional solidification of silicon that followed settling pushes the particles to the top of the ingot. The presence of SiC particles in the middle of the ingot is explained by engulfment.

Top-cut silicon scrap represents a considerable loss of the PV silicon. Removal of inclusions from the silicon scrap would make it possible to recycle it to feedstock in the PV cell production. This was carried out by filtration with ceramic foam filters.

Carbon and SiC foam filters with various pore sizes were employed in the filtration experiments. They were provided by Eger-Sørensen, a Norwegian company and Foseco AB in Sweden. The top-cut silicon scrap came from REC-Scan Wafer.

Characterization of inclusions in silicon scrap before and after filtration experiments took place. Two techniques were developed and used in this work. First, extraction of inclusions by acid dissolution of the silicon was carried out. The SiC and Si_3N_4 particles collected afterwards were analyzed and counted by automated light microscopy. In the second technique, silicon samples were ground and polished with diamond paste. Microscopic analysis consisted of measuring the surface area of the inclusions found in the silicon samples. Results show that inclusions in top-cut solar cell silicon scrap are needle-like Si_3N_4 particles and round SiC inclusions. The removal efficiency for a 30 ppi SiC filter is more than 99%. The inclusions remaining after filtration are mainly SiC particles smaller than 10 μm. The experiments show that the filtration efficiency increases with decreasing filter pore size. Some filter cakes that mainly consist of large Si_3N_4 inclusions are found on the top surface of the filter.

Deep bed filtration is the mechanism responsible for the removal of small particles. After taking into consideration various models for the foam filters the main conclusion is that interception seems to be the main removal mechanism of inclusions in silicon. Settling appears to play a minor role for our system. A new model named branch model explains better the experimental results. Due to the low wetting angle between molten metal and the filter material, capillary forces drive the melt through the filter. Therefore, the melt velocity through the filter is high. This justifies the usage of potential flow in the branch model.

It is shown that molten silicon may be contaminated in contact with the refractories. Since purity for solar cell silicon is crucial, contamination must be minimized. Graphite crucibles may be a source of relatively high levels of Al, Fe, and P. In the filtration process, wettability of the molten silicon with the filter material is very important. Thus, spreading and infiltration of molten silicon into the graphite substrates were also investigated in this thesis. Five different graphites were provided by Svenska Tanso AB. They are in use as refractories in the PV industry and vary from each other in porosity, density, and average pore size. The sessile drop technique is employed to study the

wetting behavior of molten silicon on the graphite materials. The measured contact angles show that molten silicon does not initially wet carbon materials. However, due to the chemical reaction between Si and C, a SiC layer is formed in the interface between molten silicon and the graphite. Formation of this layer lowers the contact angles finally reaching equilibrium wetting angles of molten silicon with SiC materials. Spreading of molten silicon is affected not only by the reaction formed SiC layer, but also by the surface finish. The final contact angles, also called equilibrium contact angles, decrease with increasing surface roughness of the graphites. Infiltration of silicon into graphites is mainly related to the average pore size of graphite materials. Materials with large pores are penetrated deeper by the liquid silicon. Zero contact angles of the silicon with graphites are found in materials with both high surface roughness and large average pore size. These results indicate that graphites for use in the PV industry should have a small average pore size. The surface of the graphite in direct contact with silicon should be smooth (low roughness).

List of Abbreviations and Symbols

CFF	Ceramic foam filters
CI	Cascade impactor
CVD	Chemical vapor deposition
DLS	Dynamic light scattering
DS	Directional solidification
EBIC	Electron beam induced current
EDS	Energy dispersive X-ray spectrometer
EFG	Edge defined film fed growth
EPMA	Electron probe micro analyzer
FTIR	Fourier transform infra red spectroscopy
GDMS	Glow discharge mass spectrometer
IR	Infra red
LD	Laser diffraction
MG	Metallurgical grade
mc	Multi-crystalline
ppm	Parts per million
ppma	Parts per million atoms
ppm mass	Parts per million by mass
ppi	Pores per linear inch
PV	Photovoltaic
sc	Single crystalline
SEM	Scanning electron microscope
S/L	Solid liquid
SoG	Solar grade
STDV	Standard deviation
TOF	Time of flight
V	Void
VHL	Variable heat leak
WDS	Wavelength dispersive X-ray spectrometers

XRD	X-ray diffraction	

A	Interfacial contact area	m^2
A_p	Particle projected area	m^2
a	Particle radius	m
a_0	Atomic diameter	m
a_s	Surface area of collector per unit volume of melt	m^2
b	Ratio of the collector surface area projected in the z-direction to the total collector surface area	
C_0	Concentration of impurities	kg m^{-3}
C_l	Concentration in liquid phase	kmol m^{-3}
C_s	Concentration in solid phase	kmol m^{-3}
C_∞	Initial concentration	kmol m^{-3}
c	Inclusion content	m^{-3}
c_{in}	Number per unit volume at inlet	m^{-3}
c_0	Number per unit volume at outlet	m^{-3}
D	Diameter,	m
	or pore diameter,	m
	or lateral infiltration distance	m
D_l	Diffusivity in liquid	m^2s^{-1}
d, d_p	Particle diameter	m
d_0	Interatomic distance	m
d_b	Mean filter branch diameter	m
d_c^*	Dimensionless constriction diameter	
d_g, d_{max}	Grain (collector) diameter	m
d_w	Mean filter window diameter	m
E	Filtration efficiency	
E_b	Filtration efficiency for the branch model	
$F(\theta)$	Function of θ given in Eq. (5.32)	
F_d	Drag force	N

F_g	Gravity force	N
F_M	Magnus force	N
F_r	Repulsive force	N
F_S	Saffman force	N
f	Friction factor for flow in conduits	
f_N	Number size distribution of inclusions	m^{-4}
f_s	Fraction solid	
g	acceleration of gravity	ms^{-2}
ΔH	Enthalpy change	J mol^{-1}
H	Filter depth	m
H	Infiltration depth	m
Δh	Ferrostatic pressure head	m
h	Ingot height	m
K^*	$= \lambda_p/\lambda_l$	
k	Constant	
k_0	Partition ratio	
k_B	Boltzmann constant	
k_{eff}	Effective value of k_0	
k_t	Coefficient for transfer of particles	
k_w	Kinetic constant	
L	Branch length	m
l	Mean pore height	m
m_p	Particle mass	kg
N	Number of particles	
N_R	$= d_p/d_g$	
n	Constant	
n_1	Agglomerate orientation	
ΔP_h	Pressure by a liquid column with height Δh	N m^{-2}
Q	Volume rate of flow	m^3 s^{-1}
R	Gas constant,	J mol^{-1} K^{-1}
	or particle radius	m

	or equivalent sphere radius,	m
	or collector radius	m
R_a	Surface roughness	m
R_b	Branch radius	m
R_c	Shape factor	
Re	Reynold's number	
r	Distance from axis	m
S, S_i	Surface area	m^2
	or inclusion projected area	m^2
S_i^m	Inclusion measured surface area	m^2
T	Temperature	K
T_m	Melting point	K
t	Time	s
U	Spreading rate	$m\ s^{-1}$
u	Mean particle velocity	$m\ s^{-1}$
u_r	Settling velocity	$m\ s^{-1}$
u_c	Critical velocity	$m\ s^{-1}$
V	Volume	m^3
V_h	Hyperboloid volume	m^3
X	Fractional composition,	
	or Polar function given by Eq. (5.37)	
x	Spatial coordinate	
y	Spatial coordinate,	
	or height of peaks and valleys of a surface	
z	Spatial coordinate	
ε	Void fraction (porosity)	
δ	Boundary layer thickness,	m
	or growth rate	$m\ s^{-1}$
ϕ	Friction factor	
ϕ_p	Particle volume fraction	

γ	Surface energy	N m^{-1}
γ^{sl}	Surface energy between solid and liquid phases	N m^{-1}
γ^{sg}	Surface energy between solid and gas phases	N m^{-1}
η	Collision probability	
η_{filter}^{count}	Filtration efficiency based on inclusion count	
$\eta_{filter}^{surface}$	Filtration efficiency based on surface area of inclusions	
η_i^E	Collector efficiency due to interception for isolated sphere model given by Eq. (5.9)	
η_i^P	Collector efficiency for constricted-tube model	
η_i^T	Collector efficiency for isolated sphere model given by Eq. (5.11)	
η_{sett}, η_s	Removal efficiency of settling	
χ	Polar angle	
λ_0	Filtration coefficient	
λ_p	Particle thermal conductivity	W m^{-1} K^{-1}
λ_l	Melt thermal conductivity	W m^{-1} K^{-1}
μ	Viscosity	kg m^{-1} s^{-1}
μ_0	Pure melt viscosity	kg m^{-1} s^{-1}
v	Constant, or relative velocity between the melt and collector	m s^{-1}
v_∞	Approach velocity of flow	m s^{-1}
$\Delta\rho$	Difference in density between particle and melt	
ρ	Density	kg m^{-3}
ρ_l	Density of liquid	kg m^{-3}
ρ_m	Density at melting point	kg m^{-3}
ρ_s	Density of solid	kg m^{-3}
$\Delta\sigma_0$	Surface tension difference	
σ^{lg}	Liquid surface tension	N m^{-1}
θ	Contact angle, or polar angle	

θ_F	Final (equilibrium) contact angle
θ_P	Contact angle of reaction product
ψ	Stream function

TABLE OF CONTENTS

Chapter 1

INTRODUCTION

Solar cells have been an attractive technology for power generation due to its clean and non-polluting nature [Sarti & Einhaus, 2002]. The photovoltaics (PV) industry has grown fast in the recent years. Forecasts for the average global growth give a 48% increase for the PV market up to 2012, with the global market volume of newly installed PV systems rising from 4 GW in 2008 to 125 GW in 2020 [Sarasin, 2008].

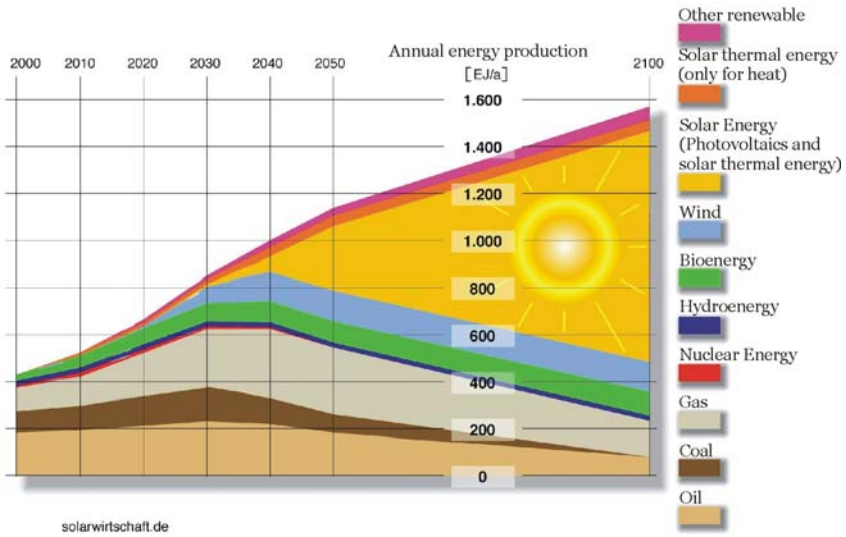

Figure 1.1: Prediction from the scientific council of the German federal government for the future annual energy production [www.solarwirtschaft.de].

Is it predicted that much of the energy production for next the decades will be solar energy produced by photovoltaics as shown in Figure 1.1 [solarwirtschaft.de]. Wafer-based crystalline silicon, including multicrystalline silicon and monocrystalline silicon, is the dominant PV technology by far with a market share of 91% in 2005 [Wyers, 2007b], [Swanson, 2007]. The overriding goal of the PV industry nowadays is to generate energy at competitive price. This can be achieved by lowering the production cost for Si modules.

Silicon accounts for approximately 25 – 50% or more (depending on the technology and the type of silicon used) of the cost of processed solar cells [Istratov *et al*. 2006]. The cost of raw silicon is determined by its purity and the current silicon shortage has focused the spotlight on poly silicon [Wyers, 2007b]. While metallurgical grade (MG-Si) silicon costs not more than US$ 1 – 1.50 kg^{-1}, semiconductor grade poly-crystalline silicon can cost anywhere from US$ 35 to 200 depending on the market conditions [Istratov *et al*. 2006].

To supply the increasing needs of the photovoltaic industry it is necessary to develop a low cost silicon feedstock. An approach to produce solar grade silicon is to upgrade metallurgical grade silicon [Flamant *et al*. 2006]. This has been a subject of worldwide research. Several companies (Elkem, FerroAtlantica, Dow Corning, Fesil and others) claim to have developed a metallurgical route to produce low cost SoG-Si [Wærnes *et al*. 2005]. This route for production can be five times more energy efficient than the conventional Siemens process that uses more than 200 kWh kg^{-1} [Braga *et al*. 2008].

The Solsilc project aims to produce solar-grade silicon by carbothermal reduction of silicon, based on the use of very pure raw materials. The raw materials for this process are ultrapure quartz and carbon black. This could give silicon with low boron content (controlled in the selection of the quartz) and a low concentration of phosphorus. A limitation of the process is the residual carbon originating from the reduction process [Braga *et al*. 2008]. This carbon is in the form of SiC particles which should be removed from the silicon before it can be used as a feedstock to PV industry. This can be accomplished by settling of the inclusions and by subsequent directional

solidification. Settling of SiC particles in molten silicon and the effect of pushing and engulfment of these particles by the solid/liquid interface were studied here.

Multicrystalline silicon is cast in a silicon nitride (Si_3N_4)-coated quartz crucible and is subsequently directionally solidified. Crystallization is realized by slowly moving downward the liquid silicon-containing crucible out of the inductively heated hot zone of the process chamber, as shown in Figure 1.2. This is the so-called conventional Bridgman technique that still is mainly used for the fabrication of multicrystalline ingots. A Si_3N_4 coating which prevents the adhesion of the silicon ingot to the quartz crucible walls, is the source of the silicon nitride inclusions in the silicon ingot. The lining refractory and graphite heating elements may be an additional source for SiC particles.

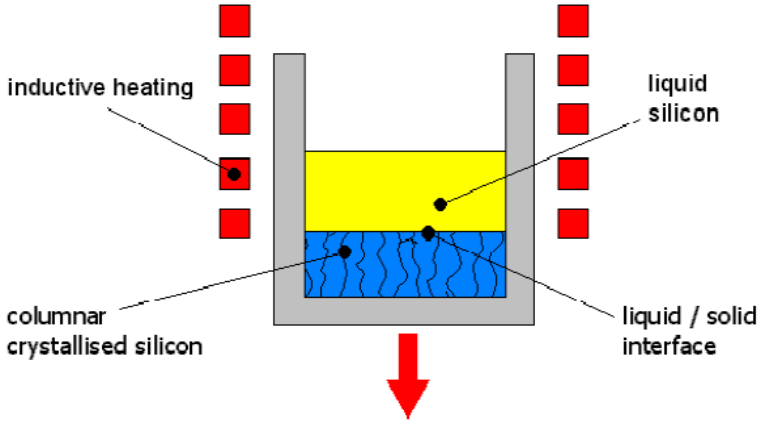

Figure 1.2: Conventional Bridgman technique for multicrystalline silicon production [Bultman & Geerligs, 2005].

After directional solidification the parts containing solid particles are cut off from the top of the ingot. Usually slices of 10 - 20 mm depth are removed. These regions have a high concentration of impurities such as iron, aluminium, SiC, Si_3N_4, etc. While the bottom and sides are recycled and used again in the solidification process, the top-cut is sold as low value scrap [Koch *et al*, 2003]. If SiC and Si_3N_4 particles can be removed from the top-cut scrap, the silicon scrap can be mixed with pure silicon from Siemens process and thus, can be used as feedstock in fabrication of multicrystalline ingots for PV cell production. Filtration with ceramic foam filters has already proved to be efficient in removing harmful particles from liquid aluminum, magnesium and steel.

The main goal of this thesis was to investigate the removal of solid inclusions in the top-cut silicon scrap by filtration with ceramic foam filter.

In the filtration process, wettability of the molten silicon with the filter material is very important. A systematic and comprehensive investigation of the wetting behavior in the liquid-silicon/solid-carbon system is still lacking. The reason for this might be difficulties of studying the system, because wetting is accompanied by chemical reaction between silicon and carbon with the formation of solid silicon carbide at the silicon/carbon interface, leading to an irreversible change in the physico-chemical nature of interface [Li & Hausner, 1996]. If the molten metal did not wet the filter, the inclusions are less likely to be removed by the filter. In such conditions it may be difficult for the melt to flow through the filter pores, particularly when filters with relatively small pore size are employed. Good wetting of the filter material by liquid silicon is an important requirement for efficient filtration.

The wettability of ceramics by liquid metals is also a key factor in many fields of high temperature materials science and engineering [Yuan *et al*. 2004]. In the processes developed for refining and casting of silicon, crucibles, dies, and substrates of various materials may be used. Graphite is a common material used for the production of crucibles in the PV industry [Dezellus *et al*. 2005]. Due to the open porosity, the molten silicon infiltrates into the graphite material. The infiltration depth depends on the physical properties of the graphites. It is a prerequisite that the infiltration of molten silicon into the refractory materials be kept to a low level so that the re-contamination of the liquid silicon stays at a minimum [Deike & Schwerdtfeger, 1995]. For these reasons, wetting and infiltration of molten silicon with graphite materials are also studied here.

Chapter 2

LITERATURE REVIEW

This Chapter consists of the literature review needed to interpret and discuss the results of the study. Solubility of carbon and nitrogen in liquid and solid silicon are given first. Then, impurities in silicon with the emphasis on the SiC and Si_3N_4 inclusions and their effect on the PV cells follow. Inclusions removal by settling, directional solidification, pushing and filtration are treated separately. Finally, the literature on wetting of molten silicon with graphites and silicon carbide materials is presented.

2.1 Solubility of carbon and nitrogen in silicon

2.1.1 Solubility of carbon in liquid silicon

The solubility of carbon in liquid silicon has been investigated by several researchers. They agree that the only phase to be considered besides liquid and solid solution is β-SiC and that the three-phase equilibrium, is eutectic [Durand & Duby, 2000].

By measuring the amount of dissolved carbon in the silicon at different temperatures, a relation for the carbon solubility as a function of temperature is

obtained. A number of researchers have studied the solubility of carbon in liquid silicon. They have often used various experimental set-ups and different analyzing techniques which resulted in a considerable variation in the measured carbon level. The results, reviewed by Søiland [2004], are summarized in Figure 2.1 in addition to the latest results. Carbon is slightly soluble in liquid and solid silicon, and according to Nozaki *et al*. [1970] the solubility in liquid Si at the melting point is 4×10^{18} atoms cm^{-3} (34 mass ppm). Durand & Duby [2000] claim that there is a problem concerning the determination of the C content in the samples. According to them, infrared measurements do not take into account the C present in the form of precipitates formed after solidification or particles resulting from an eutectic solidification step. On the other hand, the wet chemical analyses are considered to give overestimates of the C solubility since they give the total carbon content. Table 2.1 summarizes the experimental results on solubility of C in liquid Si; the method for determining the C content is indicated, together with the material used as a container, and the way the C is added to the liquid.

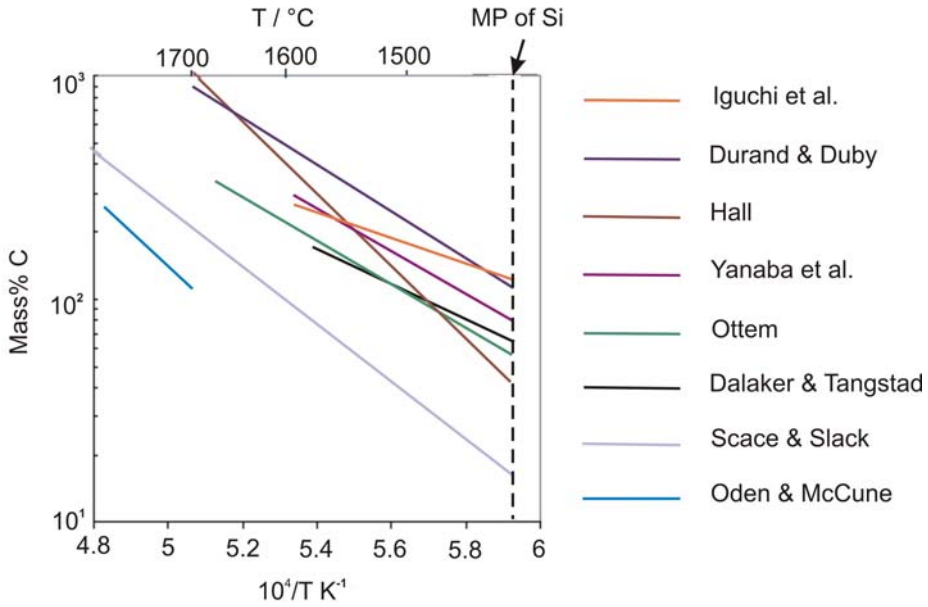

Figure 2.1: The solubility of carbon in liquid silicon as function of temperature [Søiland, 2004].

Table 2.1: Experiments on solubility of carbon in liquid silicon, review by Durand & Duby [2000], and Søiland [2004] and including the latest results.

Year	Reference	Container	Analyzing technique	Solub. at m.p. [mass ppm]
1958	Hall	Silica	Mass loss	41
1958	Dash	Si-pedestal	Mass loss	56
1959	Scace & Sclack	Graphite	Mass of residue	16
1960	Dolloff	Graphite	Wet chemical analysis	
1970	Nozaki	-	Charged particle act. analysis + IR absorption	34
1971	Bean & Newman	-	IR absorption	55
1987	Oden & McCune	Graphite	Combustion + gas analysis	5.7
1993	Kleykamp & Schumacher	Zirkonia	Combustion + gas analysis	
1993	Ottem	Silica	Mass loss	56
1993	Iguchi & Narushima	SiC	Combustion IR absorption	123
1997	Yanaba	SiC	Combustion IR absorption	79
2000	Durand & Duby	-	-	110
2008	Dalaker & Tangstad	Graphite	Combustion IR absorption	65

2.1.2 Solubility of carbon in solid silicon

Data on carbon solubility in solid silicon are given by Davies & Newman [1994] in a review updating data collected by Bean & Newman [1971]. This solubility is limited by the formation of β-SiC precipitates. Measurements were performed by infrared absorption techniques. The calibration constant for the infrared measurements is modified following subsequent work by Endo *et al*. With this correction, the solubility of C in solid Si is given by:

$$X_C^S \text{ (in atoms cm}^{-3}) = 3.31 \times 10^{24} \exp\left(\frac{\Delta H_{SS}}{RT}\right) \qquad (2.1)$$

with ΔH_{SS} = 2.3 ± 0.25 eV/atom = 221.900 J/mol. Extrapolation to the melting point of Si gives the maximum C concentration in solid solution, for T = 1414 °C = 1687 K:

$$X_C^{S,E} = 4.5 \times 10^{17} \text{ atoms cm}^{-3} = 3.8 \text{ mass ppm} \quad (2.2)$$

Nozaki *et al*. [1970] reported the solubility of carbon in solid silicon to be 3.5×10^{17} cm^{-3} (3 mass ppm) at the melting point. Bean & Newman [1971] found that the solid solubility C_s varies with temperature as:

$$C_s = 4 \times 10^{24} \exp(-2.4\text{eV}/kT) \quad (2.3)$$

which, at the melting point of silicon, gives 2.7×10^{17} atoms cm^{-3} (2.3 mass ppm). Narushima *et al*. [2002] measured the carbon solubility in solid silicon at 1673 K to be 24 ± 13 mass ppm which is very high compared to the data reported from the others. This high value of carbon solubility could be explained by oxygen content in silicon. Their experiments were performed in Ar-5%CO atmosphere at 1673 K. According to Newman [1996] carbon solubility is enhanced by the presence of oxygen atoms in silicon crystals which expand the lattice of the silicon crystal.

2.1.3 Solubility of nitrogen in liquid and solid silicon

Nitrogen is an important impurity in crystalline silicon and its properties have been extensively studied. There are four methods of doping silicon with nitrogen: melting of silicon with Si_3N_4, melting silicon in an atmosphere which includes nitrogen or ammonia, annealing silicon in nitrogen gas, and ion-implantation.

The solubility of nitrogen in silicon has mainly been studied by the first two methods. It was first studied by Kaiser & Thurmond [1959] by melting silicon in an atmosphere which included nitrogen or ammonia. They determined the solubility of nitrogen to be about 10^{19} atoms cm^{-3} (100 mass ppm) in molten silicon by vacuum fusion gas analysis. Yatsurugi *et al*. [1973] determined it using the floating zone method of hemicylindrical silicon rods sandwiching Si_3N_4. The solubility of nitrogen in the liquid silicon was determined to be about 6×10^{18} atoms cm^{-3} (60 mass ppm) by charged particle analysis. Narushima *et al*. [1994] measured nitrogen solubility at the melting point of silicon to be around 4×10^{17} atoms cm^{-3} (4 mass ppm), which is one order of magnitude smaller than the reported values by Kaiser & Thurmond [1959] and,

Yatsurugi *et al*. [1973]. The latest results reported by Dalaker [2008] give that the solubility of nitrogen at the melting point of silicon is 42 mass ppm.

Nitrogen solubility in solid silicon reported by Yatsurugi *et al*. [1973] is $(4.5 \pm 1.0) \times 10^{15}$ atoms cm^{-3} (about 45 mass ppb).

2.2 Impurities in silicon

Impurities in silicon influence solar-cell properties in a variety of ways. For example, crystal growth can be perturbed resulting in defects, inclusions, precipitates, or poly-crystalline structure. The bulk properties of the silicon may be altered by electrically active impurity centers which reduce the minority-carrier diffusion length either by increased re-combination or by scattering-induced mobility loss. Additionally, impurities may induce contact and contact interface degradation, series- or shunt-resistance effects, as well as precipitation and other junction defect mechanisms [Davis *et al.* 1980].

A vast number of impurities are present in commercial multi-crystalline (mc) Si. Light elements such as oxygen, nitrogen and carbon are the impurities present at by far the highest levels, generally in the ppm range [Stokkan, 2004]. However, these impurities are not the predominant sources of lifetime degradation. Transition metal impurities, which are found in concentrations as high as $10^{14} – 10^{16}$ cm^{-3} in most mc-Si materials, play a large role in decreasing mc-Si device performance relative to single-crystalline (sc) Si. In mc-Si materials, grain boundaries are now understood to be the locations where metals are found in the highest concentrations, aside from isolated inclusions [Buonassisi *et al*, 2006], [Mjøs, 2006]. Veritable lifetime killers are wolfram, molybdenum and titanium. These are also slowly diffusing elements, which mean they are difficult to remove by gettering. Fortunately they are not often present in the production environment, and they segregate efficiently during crystallization. Iron is considered the most important metallic impurity as it has a pronounced lifetime limiting effect. Usually it is present in large quantities and is in a middle range with regards to diffusivity [Stokkan, 2004].

2.2.1 SiC and Si_3N_4 particles in mc-silicon and their impact on solar cells

The major sources of carbon contamination in Si crystals are the graphite support (an extruded or molded graphite cylinder into which the SiO_2 crucible is placed) and accessories such as heat shields which may react with O_2, H_2O or SiO gases or the SiO_2 crucible itself to form gaseous carbon compounds that are incorporated into the melt through vapor phase transport.

The carbon impurities are generally found on substitutional sites. Even though carbon is electrically inactive, it may influence the behavior of oxygen, e.g. by inhibiting thermal donor formation at 450°C and enhancing SiO_2 nucleation and precipitation rates. If the carbon level exceeds the solubility in dislocation-free crystals, SiC particles may form and produce polycrystalline growth. The maximum solubility of carbon in oxygen-rich pulled ingots may be ~10^{18} cm^{-3} (8.5 mass ppm), and it is found that SiO_2 and Si_3N_4 precipitates may act as nucleation sites for SiC precipitation. Precipitation may also occur during the crystallization process if the liquid phase is enriched in carbon. In multi-crystalline material, SiC may form during the casting process. Moeller *et al*. [2008] reported massive SiC and Si_3N_4 precipitates from the melt in form of filaments, tubes, needles and spherical precipitates along the growth directions. A picture is shown in Figure 2.2.

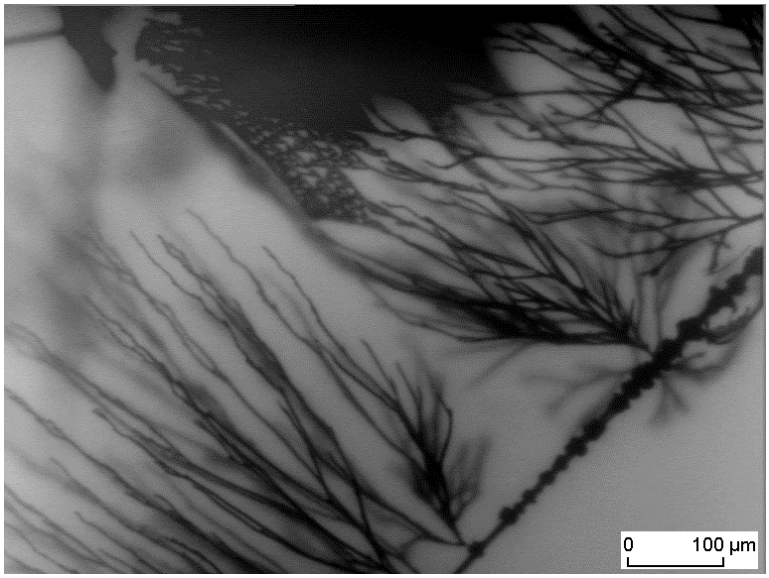

Figure 2.2: SiC and Si_3N_4 precipitates in forms of filaments, tubes, needles and spherical precipitates along the growth directions. (Foto taken with IR microscopy) [Möller *et al*. 2008].

Carbon precipitation in edge-defined-film-fed-growth (EFG) material has been connected to twinning formation [Moeller *et al*. 2008]. Formation of SiC layers in twin boundaries at the melt interface has been observed. The reason for that might be accumulation of carbon by diffusion in the melt. SiC that has precipitated during this process generates high internal stresses in the material.

2.2.1.1 Electrical effects of SiC and Si_3N_4 inclusions

Hari Rao *et. al*. [1976] observed directly the electrical effects of SiC inclusions in silicon using a scanning electron microscope (SEM) operated in the electron-beam-induced current (EBIC) mode. The EBIC analysis displayed the recombination effects around the particles. Both point source and linear recombination centers are distributed around the SiC particles. Both the maximum power output per unit area and the fill factor displayed a nearly linear dependence on SiC particle density, whereas the short circuit current and the reverse leakage currents appear to be relatively independent of the SiC particle density. The open-circuit voltage of the solar cells is only slightly influenced by SiC particle density up to a density of three particles per solar cell beyond which a dramatic reduction in the voltage is noted with increasing particle density.

Experimental observations of electrical effects associated with SiC particles suggest that in addition to the possible direct effect of the particles in functioning as local regions of low resistivity, the more detrimental effect of the particles is their influence on the distribution of lifetime killing impurities in the silicon. The data on cell performance as influenced by particles suggest that the specific detrimental effects of the SiC particles are almost entirely due to the accumulation of impurities around the particles, rather than due to the particles themselves. According to Möller *et al*. [2008] SiC inclusions create more shunting than Si_3N_4 because SiC are more conductive.

Areas with a high number of dislocations are known to reduce the free carrier lifetime severely. Solid inclusions are one of the sources that create dislocations. Dislocations are punched out during cooling from around an inclusion with a different thermal expansion coefficient than the surrounding matrix. The nucleation of dislocations results from the stress produced around the inclusion due to the different contraction of the crystal and the inclusion [Ryningen *et al*. 2008]. Ryningen *et al*. [2008] observed more dislocations around the SiC particles than around Si_3N_4 particles thus, concluding that SiC is more detrimental than Si_3N_4 when it comes to nucleation of dislocations. Figure 2.3 shows dislocation clusters around a SiC particle and Figure 2.4 shows a Si_3N_4 particle surrounded by dislocations in a multicrystalline silicon wafer [Ryningen *et al*. 2008]. The wafer was polished and etched in Sopori etch.

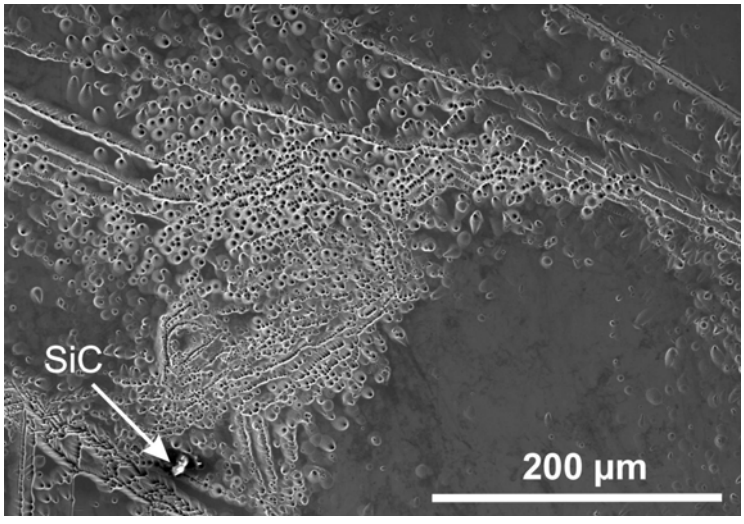

Figure 2.3: SEM image of a dislocation cluster around a SiC inclusion. The wafer is polished and etched in Sopori etch [Ryningen *et al*. 2008].

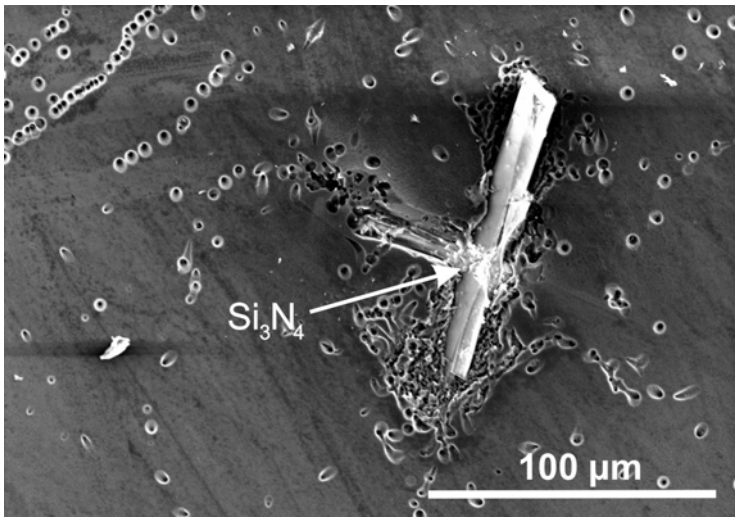

Figure 2.4: SEM image of dislocations around a Si_3N_4 inclusion. The wafer is polished and etched in Sopori etch [Ryningen *et al*. 2008].

2.2.1.2 Effects of SiC and Si_3N_4 in wire sawing

Du *et al*. [2008] studied the effect of SiC and Si_3N_4 inclusion in wire sawing process of mc-silicon. The presence of SiC particles is responsible for the formation of wire-sawing defects on the mc-Si wafers, while Si_3N_4 rods can be readily sawed across without introducing wire-sawing defects during the wire-sawing process. The dimension of the SiC clusters and Si_3N_4 rods was found to be up to hundreds of micrometers, and they can extend from one surface of a mc-Si wafer to the other [Du *et al*. 2008]. A sawing wire could break due to the presence of SiC particles.

2.3 Removal of elements and solid particles

2.3.1 Settling of inclusions

Settling in molten metals is one of the refining steps for removal of harmful inclusions. Inclusions may be lighter than the molten metal (this situation is usually found in steelmaking and ferroalloys), or they may be heavier than the melt as is often the case for aluminum. The inclusions that float up are collected by a slag or dross phase while heavy inclusions accumulate as slurry in the lower parts of the furnace (a

holding or settling furnace). In either case the removal mechanism is gravity coupled with the density difference (negative or positive) between the particle and the surrounding melt. The term "settling" in this thesis is used only when particles sink. The gravity force acting on a particle is given by:

$$F_g = (\rho_s - \rho_l)gV \tag{2.4}$$

where V and ρ_s is the volume and density of the particle, ρ_l is the density of the liquid metal, and g is the acceleration of gravity. The drag force F_d on the particle is usually calculated in terms of an empirical friction factor ϕ:

$$F_d = \rho u_r^2 A_p \phi \tag{2.5}$$

u_r is the relative velocity between the surrounding melt and the particle. The terminal settling velocity of a particle is determined by the balance between the opposing forces F_g and F_d:

$$(\rho_s - \rho_l)gV = \rho u_r^2 A_p \phi \tag{2.6}$$

which can be arranged in the form:

$$u_r^2 = \frac{(\rho_s - \rho_l)gV}{\phi \rho_l A_p} \tag{2.7}$$

For spherical particles

$$V = \pi d^3/6, \qquad A_p = \pi d^2/4 \quad \text{and} \quad \phi = 12/\mathrm{Re} \quad \text{if} \quad \mathrm{Re} < 2 \tag{2.8}$$

$\mathrm{Re} = u_r d\rho_l/\mu$. Thus, for spherical particles under laminar flow conditions, we get the Stokes' equation:

$$u_r = \frac{d^2(\rho_s - \rho_l)g}{18\mu} \tag{2.9}$$

where d is the diameter of the spherical inclusion and μ is the viscosity of the liquid metal.

2.3.2 Directional solidification of mc-Si

Directional solidification is a well known method for producing multicrystalline silicon for the PV industry. In this method a planar front, achieved during solidification, results in a clearly defined interface between the solid and the liquid phase. The solubility of major impurities is higher in the liquid than in the solid phase. Therefore,

directional solidification will work as a purification process where the impurities are retained in the liquid phase. The maximum purification is given by Scheil equation:

$$C_l = C_0 \cdot (1 - f_s)^{k_0 - 1} \tag{2.10}$$

where C_l is the concentration of impurities in the liquid phase at a given fraction solid f_s, C_0 is the concentration of impurities when solidification begins. k_0 is the partition ratio defined by $k_0 = C_s / C_l$, where C_s is the impurity concentration in the solid phase. Equation 2.10 assumes thermodynamic equilibrium at the solid-liquid interface, no diffusion of impurities in the solid phase and complete mixing in the liquid phase. For most systems the assumption of equilibrium at the solid-liquid interface and no diffusion in the solid are fulfilled. However, in a relatively stagnant melt, mixing in the liquid is only partial. Impurities will build up in a boundary layer close to the solidification front with increased concentration of impurities. These various effects tend to give a reduced "effective" value of k_0, k_{eff}:

$$k_{eff} = \frac{k_0}{k_0 + (1 - k_0)\,\mathrm{e}^{-(v\delta / D_l)}} \tag{2.11}$$

Where v is the growth rate, δ is the thickness of the boundary layer and D_l is the element diffusivity in silicon. It is seen that when $v \to 0$, $k_{eff} \to k_0$. Data on partition ratio, k_0 and diffusivity for carbon and nitrogen are given in Table 2.2.

Table 2.2: Properties of carbon and nitrogen in silicon

Property	C	N	Ref.
Diffusivity, D_l	$1.9 \times e^{(-3.1/k_BT)}$ [cm^2s^{-1}]	$0.87 \times e^{(-3.29/k_BT)}$ [cm^2s^{-1}]	[Scase & Slack 1959];
Partition ratio, k_0	0.07 ± 0.01	7×10^{-4}	[Nozaki et al. 1974]; [Yatsurugi et al. 1973]

Kvande *et al*. [2005] and Ryningen *et al*. [2008] investigated the carbon content in two multicrystalline silicon cast ingots. These ingots were directionally solidified with different cooling rates after solidification was completed, 190°C/hr and 50°C/hr. Substitutional carbon concentration as a function of ingot height was measured by Fourier transform – infra red spectroscopy (FTIR). The results were compared with the carbon values calculated from the Scheil equation with a partition ratio of 0.058

suggested by Kolbesen & Mühlbauer [1982] (see Figure 2.5). The start concentration was set at 1.7 ppma. Their results show that the carbon distribution in the two ingots was similar with a concentration of about 4 ppma in the middle of the ingots. The measured carbon concentrations fit well with the concentration profile calculated from Scheil equation.

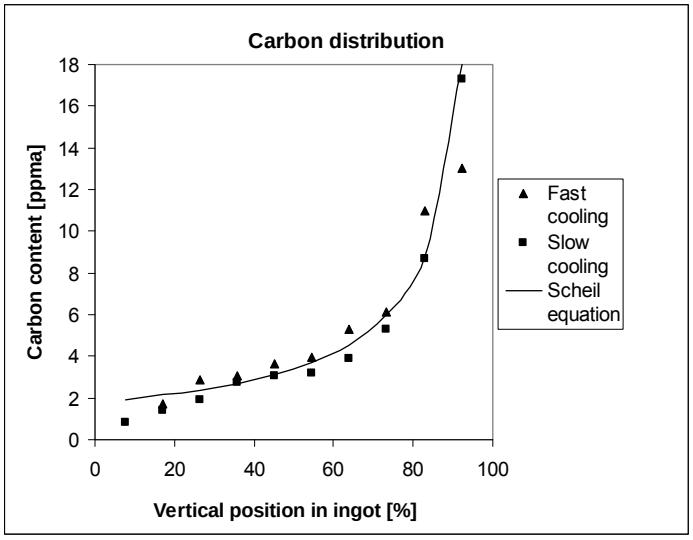

Figure 2.5: Carbon content as a function of vertical position in ingot measured by FTIR and calculated from Scheil equation using a partition ratio of 0.058 [Kvande *et al*. 2005].

2.3.3 The solid liquid interface

The form of the solid-liquid interface during solidification has considerable influence on the material quality. If the interface breaks up and columnar cells start to grow, both grain size and impurity distribution will be largely influenced. Solidification velocity, temperature gradients in the melt and, impurity concentrations are the growth conditions which may cause interface breakdown [Kvande, 2008].

2.3.3.1 Interface breakdown

The original concepts for understanding interface instabilities are contained in the work of Rutter & Chalmers [1953]. They studied the formation of the cellular substructure found in slightly impure metals. The cellular substructure consists of a honey-comb-like structure, elongated in the growth direction, with a more or less regular hexagonal pattern on the interface. According to Rutter & Chalmers [1953], this

structure results from an instability of the interface. Due to the fact that the boundary layer near the interface is rich in impurities rejected by the growing crystal, the melting point of the liquid at the interface is depressed. Therefore, the liquid ahead of the growing interface could be supercooled even though it is at a higher temperature than the interface. They suggested that this condition caused the instability and named it Constitutional Supercooling [Rutter & Chalmers, 1953]. Since $k_0 < 1$, the solute element will be rejected into the liquid and be enriched at the solidification front. A concentration gradient will then develop in front of the interface causing a local variation of liquidus temperatures. The diffusion process in the liquid ahead of the interface is treated in a one-dimensional coordinate system moving with the interface [Jackson, 2004]. The equation for steady-state diffusion in a one-dimensional coordinate system moving with the interface at a velocity v is:

$$D_l \frac{\mathrm{d}^2 C_l}{\mathrm{d}z^2} + v \frac{\mathrm{d}C_l}{\mathrm{d}z} = 0 \tag{2.12}$$

where C_l is the composition in the liquid, D_l is the diffusion coefficient, and z is the distance from the interface. The concentration distribution which is a solution to this equation is:

$$C = C_\infty + C_\infty \left(\frac{1}{k_0} - 1 \right) \exp\left(- \frac{vz}{D_l} \right) \tag{2.13}$$

where C_∞ is the initial concentration of the liquid, and k_0 is the partition ratio. The concentration distribution given by equation (2.13) is illustrated in Figure 2.6.

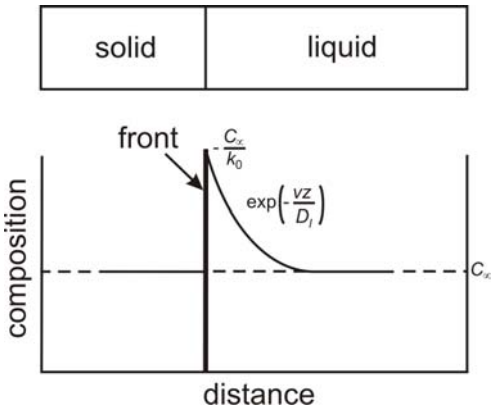

Figure 2.6: The steady-state concentration distribution ahead of a moving interface [Jackson, 2004].

Under conditions of directional solidification the stable-solid liquid interface is planar. Above a critical velocity, u_c, the plane front breaks down to form cellular patterns. Further increase of u_c results in the development of dendritic microstructures and finally, at very high rates, in a reverse transition from dendrites to cells and finally to plane front [Kurz & Fisher, 1989], [Ludwig & Kurz, 1996].

Boettinger & Warren [1999] studied the solid-liquid (SL) interface breakdown during directional solidification of a binary alloy. The build-up of solute in the liquid ahead of the interface was the main reason for planer front breakdown. As it can be seen from Figure 2.7 the interface becomes a cellular front. The concentration of the solute above the solidification front as well as the profile produced in the solid, are shown. Perturbations of the interface begin to be amplified in Figure 2.7b. By Figure 2.7f, a quasi-steady cellular structure has been formed.

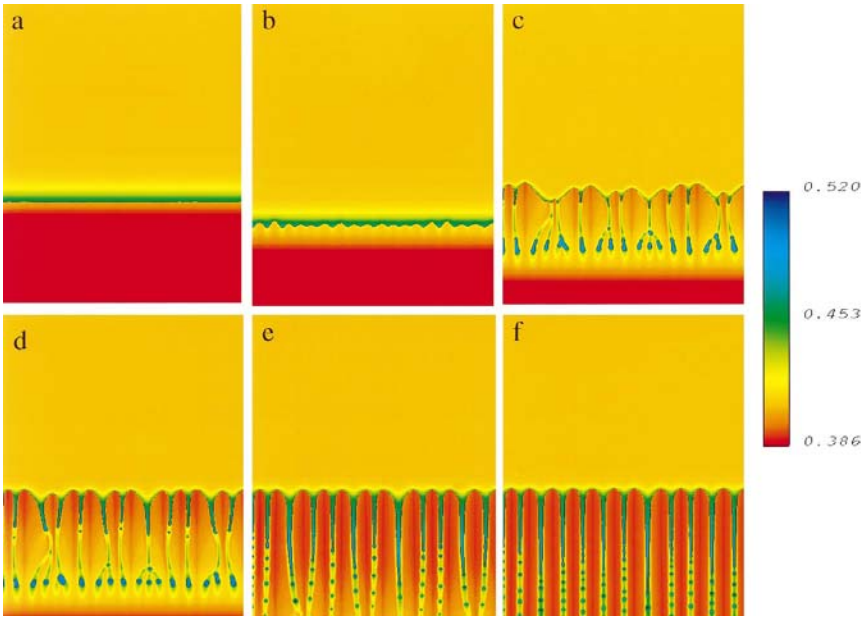

Figure 2.7: Computer simulation of the interface breakdown from planar into cellular. The concentration profile of the solute is shown in atomic fraction. The solidification growth velocity is 0.5 cm/s [Boettinger & Warren, 1999].

Fujiwara *et al*. [2002] observed the crystal growth behavior of low undercooled silicon melt using a confocal scanning laser microscope. The morphology of the

interface changed from planar to facet (Figure 2.8) and the measured critical velocity, u_c, was approximately 30 μm/s.

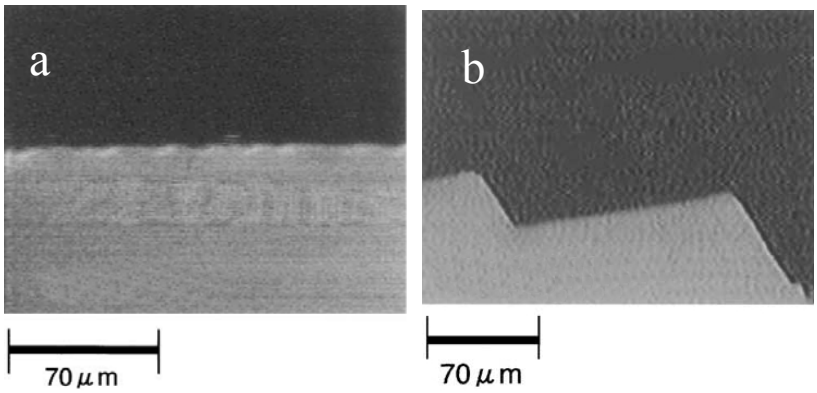

Figure 2.8: a) Planar interface of mc-Si cooled at 3 K/min with a growth rate of 32 μm/s; b) facet interface of mc-Si cooled at 25 K/min with a growth rate of 167 μm/s [Fujiwara *et al*. 2002].

2.3.4 Pushing of inclusions by directional solidification front

The behavior of solid particles at the solid/liquid (S/L) interface of an advancing solidification front is a phenomenon of practical importance in metallurgy. Location of the particles with respect to grain boundaries at the end of solidification, metal matrix composites produced by casting or spray forming techniques, inclusion management in steels etc. are some of the issues concerned with this phenomenon. When a liquid containing an insoluble particle is solidified, three distinct interaction phenomena have been observed: engulfment of particles, continuous pushing, and particle pushing followed by engulfment [Catalina *et al.* 2000]. When the solidification front is cellular or dendritic, entrapment of the particles may happen. The term "engulfment" is used to describe incorporation of a particle by a planar interface, and the term "entrapment" is used for particle incorporation by a cellular or dendritic interface, because the mechanisms are rather different (see Figure 2.9). Indeed, for entrapment to occur, particles must be pushed by the growing dendrites into the interdendritic regions [Juretzko *et al*. 1998].

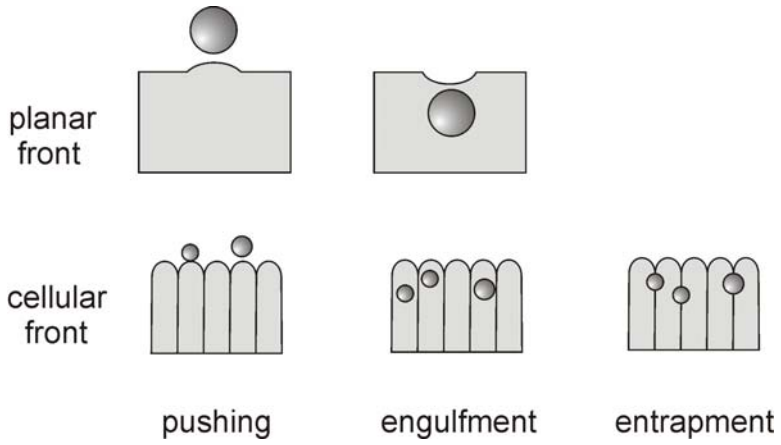

Figure 2.9: Schematic representation of particle-interface interaction as a function of interface morphology [Juretzko *et al*, 1998].

Numerous models for particle behavior at the S/L interface have been proposed. The basic assumptions of most kinetic models assume spherical and inert particles and a macroscopically planar S/L interface [Dhindaw, 2000]. All the models agree that there exists a critical velocity of the planar S/L interface, below which particles are pushed ahead of the advancing interface and above which particle engulfment occurs. This velocity is a function of the solidification velocity and some material parameters.

Søiland [2004] calculated the critical velocity for pushing / engulfment, u_c, as a function of particle radius for the system Si-SiC based on the model of Stefanescu *et al.* [1988] (see Figure 2.10). According to this model the critical velocity for pushing / engulfment of particles is:

$$u_c = \frac{\Delta\sigma_0 d_0}{6(n-1)\mu R}\left(2 - \frac{\lambda_p}{\lambda_l}\right) \tag{2.14}$$

where $\Delta\sigma_0$ is the surface tension difference, $\Delta\sigma_o = \sigma_{ps} - \sigma_{pl} - \sigma_{ls}$, d_0 is the interatomic distance in the melt, μ is viscosity of the melt, R is the particle radius, λ_p is the thermal conductivity of the particle and λ_l is the thermal conductivity of the melt and, n is equal to 2. The parameter values used by Søiland [2004] are shown in Table 2.3.

Based on these calculations, at a growth velocity of 5.55 μm/s, which is the common growth rate in industry, engulfment will occur for a particle with radius 1296 μm or above.

Table 2.3: Parameter values used by Søiland [2004] in Equation (2.14) in calculating V_{cr}.

Parameter	Value
μ	9.4×10^{-4} Nsm^{-2}
$\Delta\sigma_0$	0.1 Nm^{-1}
d_0	2.6×10^{-10} m
λ_p	24 Wm^{-1}K^{-1}
λ_l	55 Wm^{-1}K^{-1}

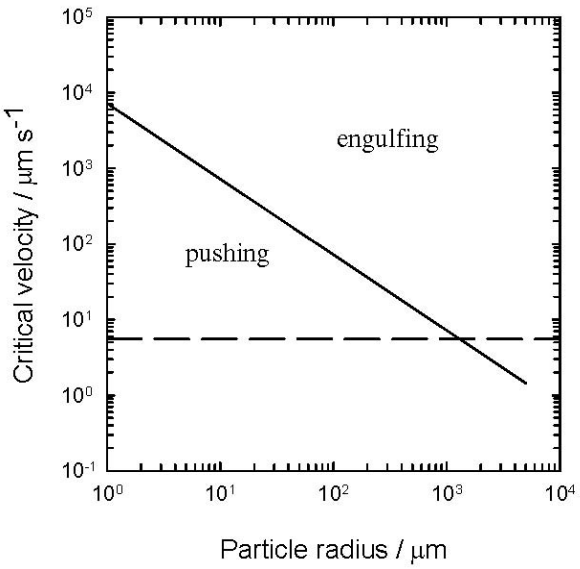

Figure 2.10: u_c as a function of particle radius for the system Si(l)-SiC(s). Dashed line represents a mean growth rate in industry (5.55 μm/s) [Søiland, 2004].

In many instances the particles form agglomerates in the melt which are then distributed within the grains or at the grain boundaries. Sen *et al.* [1999] suggested a modified model of that given by Stefanescu *et al*. [1988] and [1998] to predict u_c for a particle cluster or agglomerate:

$$u_c = \left(\frac{1}{3} \frac{\Delta\gamma_0 a_0^2 n_1}{\mu K^*} \frac{R}{R_c} \right)^{1/2} \tag{2.15}$$

where u_c is expressed now as a function of the agglomerate orientation, n_1 and its shape factor R_c, $\Delta\gamma_0$ is the surface energy difference between particle/solid and particle/liquid,

a_0 is the atomic diameter, $K^* = \lambda_p/\lambda_l$ is the ratio between the thermal conductivity of the particle and of the liquid. The presence of the particles in the melt affects the melt viscosity:

$$\mu = \mu_0(1 + 2.5\phi_p + 10\phi_p^2) \tag{2.16}$$

where μ_0 is the viscosity of the melt without the particles, ϕ_p is the volume fraction of the particles [Kim & Rohatgi, 1998].

The interaction of particles with the S/L interface is significantly altered by convective flow in the vicinity of the interface. Numerous experimental results clearly suggest the presence of lift forces due to fluid flow. The flow in the case of pure materials is attributed to density gradients in the melt, which in turn are caused by thermal gradients. For alloys, there is an additional contribution from solute effects [Mukherjee & Stefanescu, 2004]. Han and Hunt [1995] developed a model to calculate the critical flow rate required to push the particles ahead of the interface and compared the results with experiments. In their model, particle pushing is considered to be a result of fluid flow rather than surface energy interactions. However, the pushing / engulfment transition has been observed in experiments performed under microgravity conditions [Stefanescu *et al.* 1998], where liquid convection effects are negligible. This suggests that surface energy interactions cannot be neglected. The full implications of the surface energy have been recently discussed by Kaptay [2001]. Under normal gravity conditions, liquid convection effects play a dominant role and have to be considered along with the pushing force exerted on the particles due to surface energy interactions. Mukherjee & Stefanescu [2004] considered the liquid convection effects on the pushing / engulfment of particles and gave an expression for the liquid velocity profile ahead of S/L interface. They showed that the level of convection determines the behavior of the particles. For high-convection levels (Re > 0.6), the particles are swept away from the S/L interface and there is no interaction between the particles and the S/L interface because the lift forces are much greater than the interface force. For moderate-convection levels (0.1 < Re < 0.6), the critical velocity of engulfment increases with the increase in convection level. When the convection level further decreases, the system can be considered to be in the low-convection regime (Re < 0.1), in which the critical velocity for engulfment is independent of the convection level. In this regime, the lift

forces due to liquid convection are negligible compared to the interface pushing force [Mukherjee & Stefanescu, 2004]. As a conclusion to their model three distinct convection regimes were identified:

High convection regime	no particle-interface interaction	Re > 0.6
Moderate convection regime	increased critical velocity	0.1 < Re < 0.6
Low convection regime	no effect on critical velocity	Re < 0.1

2.3.5 Filtration of inclusions with ceramic foam filters

Filtration in metallurgy is a process of removing inclusions by forcing molten metal through a porous material. The most important characteristic of a filter is the filtration efficiency E defined by:

$$E = 1 - \frac{c_0}{c_{in}} \tag{2.17}$$

where c_{in} is the number of inclusions per unit volume that enters the filter, while c_0 is the number per unit volume that leaves [Engh, 1992]. It is verified that filtration efficiency follows an exponential law given by Equation 2.18 [Lae *et al*. 2006]

$$E = 1 - \exp(-\lambda_0 H) \tag{2.18}$$

where λ_0 is the filtration coefficient which depends on the properties of the filter and the inclusions, and H is the filter thickness or depth.

Ceramic foam filters (CFF) are commonly used in industry for filtering a variety of molten metals, including aluminum, iron, magnesium and copper [Lae *et al*. 2006], [Wieser, 1988], [Apelian & Choi, 1988], [Uemura *et al*. 1992]. The excellent thermal shock resistance facilitates their use for metal melt filtration. Ceramic foam filters improve molten metal casting quality by removing non metallic inclusions. Typically, ceramic foam filters exhibit high porosities (70 – 90%) with non uniform cells connected to each-other by ligaments. The foam is characterized in terms of the pore diameter or pore per inch (ppi) density. Typically pore diameters range between 0.01 to 2 mm [Sharafat *et al*. 2006]. Ceramic foam filters with 10, 20 and 30 ppi are commonly used for metal filtration with a trend to use finer pores filters (50, 60, 80 ppi). Figure 2.11 shows three - and two – dimensional images of a ceramic foam filter [Gauckler *et al*. 1985].

No reports on filtration of liquid silicon with ceramic foam filters seem to have been published. However, the extensive literature on the filtration of liquid aluminum and steel has been used.

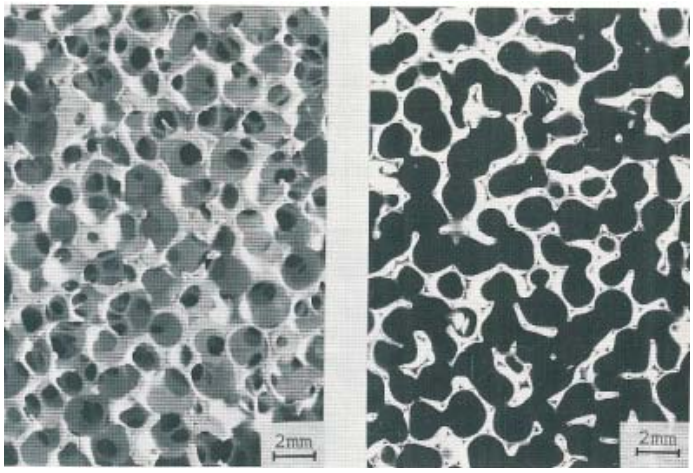

Figure 2.11: Three - and two – dimensional images of a ceramic foam filter [Gauckler *et al*. 1985].

When discussing the removal mechanism of particles we speak of cake filtration and deep-bed filtration. The filter mechanisms are illustrated in Figure 2.12. In cake filtration, the filter medium acts as a screen so that particles are retained by the filter material, resulting in the formation of filter cakes. In this case, the particles will remain on the top surface of the filter and the first deposited particles will act as a filter for the last particles approaching the filter. In contrast, in deep bed filtration, separation is effected through the particle deposition throughout the entire depth of the filter. Consequently, cake filtration is also known as surface filtration while deep bed filtration is often referred to as depth filtration [Tien & Ramarao, 2007].

The most important factor in determining cake formation is the relative filter pore size to particle size. Empirical evidence indicates the occurrence of cake formation if the particle size and the filter pore size are of the same order of magnitude. Cake formation commences immediately if the particle size is 1/3 of the size of the medium pore [Tien & Ramarao, 2007]. According to Engh [1992], even if the inclusions are much smaller than the pore size, the section of the filter closest to the inlet gradually fills up and the mechanism will more and more resemble cake mode filtration. The

behavior of the cake depends on the size and size distribution of the inclusions and the pressure gradient experienced by the inclusions in the cake. The pressure drop is very great in a cake. In chemical engineering systems where pressures of many atmospheres can be applied, cake filtration is important. In high temperature metallurgical applications usually only a pressure drop of less than 1 atmosphere is available. Then filtration must be based on removal down through the filter (deep bed filtration) [Engh, 2008].

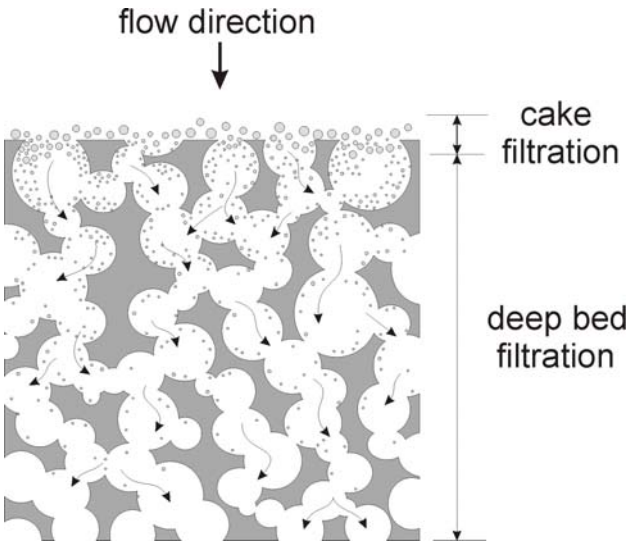

Figure 2.12: Deep bed filtration in a ceramic foam filter with the beginning of cake formation which will block filtration.

Filter capacity is defined as the quantity of deposited particles (usually expressed in grams or kilograms) which the filter is capable of accumulating before reaching a certain pressure drop (loss of metallostatic head). The filter capacity clearly depends on the type and size of the particles [Engh 1992]. During operation, a ceramic foam filter is expected to undergo three different stages [Bakke *et al*. 1994]:

- The priming period,
- The depth filtration period,
- The cake filtration period.

During the priming period, which is expected to be short in comparison with the others, the metal enters some or all of the filter pores. The fraction of the filter pores infiltrated depends on filter pore size, surface tension of the melt and pressure head. During this

period, the metal flow through the filter increases from zero up to a stationary value. During the depth filtration stage, flow remains approximately constant. Build-up of inclusions does not seem to affect the overall resistance in the filter. In the last stage, when cake filtration starts, the metal flow decreases and finally terminates. The reason is the deposition of the inclusions at the top of the filter which gives a high resistance [Bakke *et al*. 1994].

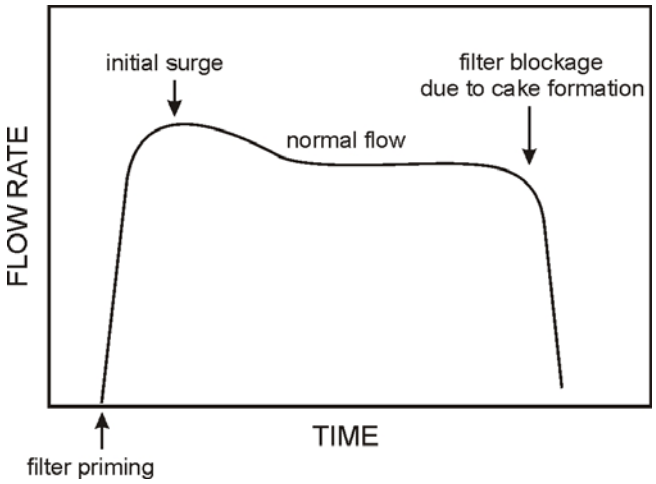

Figure 2.13: Flow rate as a function of time for filtration by ceramic foam filters [Bakke *et al*. 1994].

Various models have been developed to explain particle attachment at or on the filter media and to give a better understanding of the physical parameters that affect the removal efficiency of deep bed filtration. The main physical parameters that govern depth filtration efficiency include [Conti & Netter, 1992]:

- texture of the porous medium, pore size distribution, and filter porosity,
- filter depth,
- viscosity of molten metal,
- particle size distribution,
- particle density,
- flow rate through porous medium,
- interfacial properties between inclusions, metal, and filter.

Inclusion capture in deep bed filtration is considered to be a result of two sequential events [Raiber *et al*. 1995], [Hübschen *et al*. 2000], [Cao & Jahazi, 2005]:

- transport of the particles from the bulk melt to inner parts of the filter pores,
- attachment of the particles to the pore walls.

A number of mechanisms are considered to be responsible for the particle transport among which impingement (direct collision), interception (fluid flow transport), sedimentation (gravity), diffusion (or Brownian movement), and hydrodynamic effects are the most important [Gauckler *et al*. 1985], [Ahmad & Marshall, 2004]. Figure 2.14 shows a sketch of transport mechanism of a particle in deep bed filtration. When the difference in density between the liquid metal and the particle is high, the sedimentation forces will be the main actors to affect particle transport. If the difference decreases, sedimentation will become negligible and interception will become the dominant factor [Hübschen *et al*. 2000].

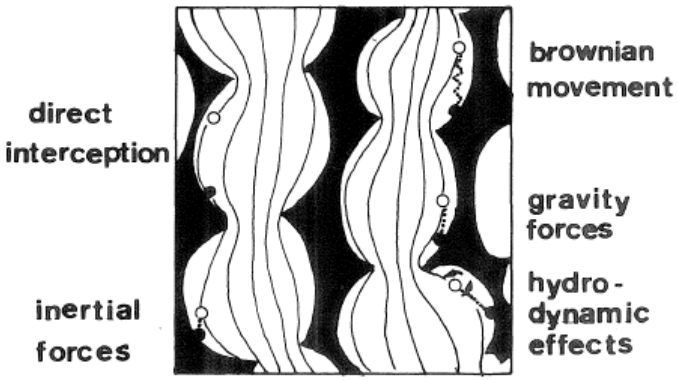

Figure 2.14: Transport mechanisms of a particle in deep bed filtration (— trajectory line) [Gauckler *et al*. 1985].

Fluid flow conditions are very important for the filtration efficiency. Particles are transported by the fluid that forms a recirculatory pattern inside the pores, towards the filter wall where they can contact with the internal surface of the filter and attach to it [Acosta & Castillejos, 2000a; 2000b]. However, large particles are less sensitive to this recirculatory pattern. Ali *et al*. [1985] suggests for steel that mechanical entrapment is responsible for filtration of inclusions larger than 30 μm, whereas surface forces are

responsible for the retention of inclusions smaller than 30 μm. The primary mode of transport of inclusions smaller than 30 μm to the filter walls is due to flow dynamics [Ali *et al*. 1985]. At the same time, the fluid flow can be responsible for dragging out the captured inclusions. Under the same fluid flow conditions, higher filtration efficiencies and a more consistent performance are obtained when using filters with a small pore size, i.e., those in which the distance from the bulk to the wall is short. Deposition of inclusions on the wall decreases exponentially with depth [Engh, 1992], [Lae *et al*. 2006], [Bradford *et al*. 2004], [Syvertsen *et al*. 1999], which is typical of depth filtration.

Particle attachment can be a result of forces developed through pressure, chemical, or van der Waals effects. The relative dominance of each mechanism is a function of particulate type and size, fluid approach velocity, as well as temperature and media characteristics. The probability that a particle will be attached on the filter walls depends on many factors [Hübschen *et al*. 2000], such as:

- *Filter*: Depth, chemical composition, microporosity, topography, and wettability.
- *Inclusions*: Composition, density, size, and morphology.
- *Melt*: Flow rate of metal through the filter, and fluid flow pattern inside the pores.

The forces at the three interfaces (interfacial tensions) between the melt and filter material, melt and inclusions, and inclusions and filter play an important role in filtration. Also a gas or vacuum phase formed between the filter material and inclusion may influence the filtration properties [Engh, 1992]. According to Raiber *et al*. [1995] when the particle is transported to the filter wall, attachment occurs as a result of the reduction of energy in the local system. Figure 2.15 shows the situation of a particle attached to the filter wall under non-wetting conditions.

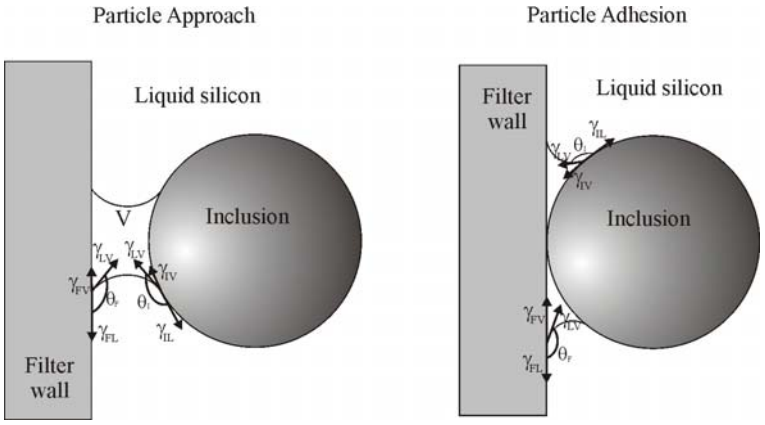

Figure 2.15: Particle approach (a) and adhesion (b) under non-wetting conditions [Raiber *et al*. 1995].

In the filtration process, wettability of the molten metal with the filter material is important. If the liquid does not wet the filter, then the inclusions are less likely to be removed by the filter. In such conditions it may be difficult for the liquid to flow through the filter pores, particularly when a filter with relatively small pore size is employed. Good wetting of the filter material by liquid silicon is a requirement for efficient filtration. The ferrostatic pressure head, Δh, required for filling a pore of the diameter D, is determined by the interfacial energy and can be calculated using equation 2.19 [Raiber *et al*. 1995]:

$$\Delta h = \frac{4 \cdot \sigma^{lg} \cdot \cos\theta}{\rho_l \cdot g \cdot D} \tag{2.19}$$

where θ is the contact angle of molten metal on the filter material, σ^{lg} is the surface tension of the liquid phase, ρ_l is the density of molten metal, and g is the gravity constant.

Inclusions can also interact with each other. The fluid flow profile plays an important role in this mechanism [Lee & Koplik, 2001]. Inside a pore there are regions with turbulent flow and regions with laminar flow. It is thought that the turbulent flow allows very small particles to agglomerate and then be attached in the regions with laminar flow. Strongly attached particles improved the filtration efficiency by trapping more incoming particles and evolving into so-called "dendrites". Particles that move along the undisturbed streamlines have higher probability to intercept. This can lead to the formation of bridges across filter pores in the uppermost part of the filter.

De-attachment of the particles from the filter walls can happen during filtration process. The filter efficiency and the product quality are greatly affected by the re-entrainment of inclusions. However, the mechanism of the particle de-attachment is complex and not fully understood yet [Kocaefe *et al*. 2004a, 2004b]. According to Kocaefe *et al*. [2004a] the filter media can not retain all the deposited inclusions and their re-entrainment happens due to the hydrodynamic effects during the continuous operation of the filter. If the viscous drag on the particle is not higher than the forces that cause attachment, the inclusion will remain inside the filter [Hübschen *et al*. 2000].

2.4 Wettability of molten silicon at high temperatures

The wettability of ceramics by liquid metals is a key factor in many fields of high temperature materials science and engineering [Yuan *et al*. 2004]. During the last 10 years, considerable effort with respect to production of low cost solar cells has been directed at developing alternative processes for refining and crystallization of silicon. In these processes crucibles, dies, and substrates of various materials may be used. It is a prerequisite that the reactions with these refractory materials be kept to a low level so that the contamination of the liquid silicon stays at a minimum [Deike & Schwerdtfeger, 1995].

Often graphite is employed as a material for the production of crucibles and dies. At the graphite/silicon interface a layer of silicon carbide forms. Particles of silicon carbide in silicon have detrimental effects on the semiconductor properties and must be avoided. Although some wetting experiments have been performed, a systematic and comprehensive investigation of the wetting behavior in the liquid-silicon/solid-carbon system is still lacking. The reason for this might be difficulties of studying the system, because wetting is accompanied by chemical reaction between silicon and carbon with the formation of solid silicon carbide at the silicon/carbon interface, leading to an irreversible change in the physico-chemical nature of interface. Generally speaking, the wetting process in reactive metal/ceramic systems is controlled by the chemical reaction which takes place at the metal/ceramic interface. Consequently, analyses of reactive wetting require a more detailed understanding of the mechanism and kinetics of the

interfacial reaction [Li & Hausner, 1996]. Silicon carbide, SiC, on the other hand is one of the silicon based ceramics, thus, the wettability of liquid-silicon/SiC-materials is reported by many authors [Whalen & Anderson, 1975], [Yupko & Gnesin, 1973], [Li & Hausner, 1991], [Zhou & Singh, 1995], [Naidich *et al*. 1998].

The wetting of a solid by a liquid drop is characterized by the contact angle, θ, defined in Figure 2.16 [Stølen & Grande, 2004]. The condition for mechanical equilibrium gives the so called Young-Dupré equation:

$$\cos\theta = \frac{\gamma^{sg} - \gamma^{sl}}{\sigma^{lg}} \tag{2.20}$$

where: γ^{sg} is the surface energy between solid and gas phases

γ^{sl} is the surface energy between solid and liquid phases

σ^{lg} is the surface tension of the liquid phase

We usually distinguish between wetting ($\theta < 90°$) and non-wetting ($\theta > 90°$) liquids. If the contact angle is zero, the liquid is considered to be perfectly wetting.

The experimental equipment used by most of the authors to measure the contact angle by the sessile drop method consists essentially of a dense alumina tube whose central part is located inside a high-temperature furnace. Windows are fitted at each end of this tube; the drop on the substrate is illuminated by a high-intensity xenon lamp and can be photographed by a camera system. The tube is connected to a gas feed system and a vacuum device. The experiments are conducted in purified argon (purity of 99.998%) at a pressure of one atmosphere [Li & Hausner, 1996], [Zhou & Singh, 1995]. The temperature is measured by a Pt/Pt+ 10% Rh thermocouple located in the immediate vicinity of the sample.

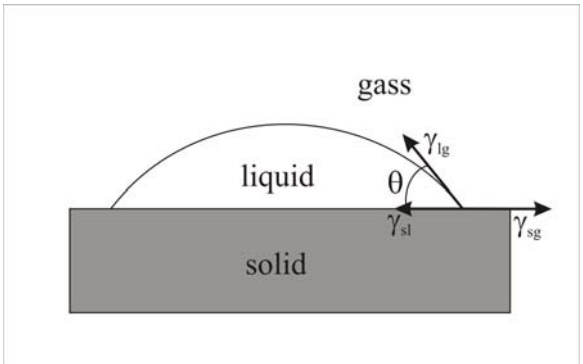

Figure 2.16: Contact angle θ of a liquid drop resting on a solid surface [Stølen & Grande, 2004].

2.4.1 Wettability of silicon with solid carbon

Wettability and infiltration of molten silicon in carbon materials is widely studied. Silicon used in these studies has high purity (99.999%). Various types of carbon materials such as glassy or vitreous carbon, pyrolytic graphite, and natural graphites are employed as substrates with known open porosity and pore size [Deike & Schwerdtfeger, 1995], [Dezellus *et al*. 2005], [Li & Hausner, 1996], [Zhou & Singh, 1995].

Melting (t = 0) starts at the contact points between the silicon and the substrate once the melting point (1414°C) of silicon is attained (Figure 2.17b). During melting the part of the silicon in the liquid state spreads on the substrate (Fig.2.17c) (Complete melting is usually achieved after 1.5 min). The contact angle θ generally takes relatively high values at the moment of complete melting of the metal, but decreases rapidly with time to stabilize at relatively low values after about 10 min [Li & Hausner, 1996].

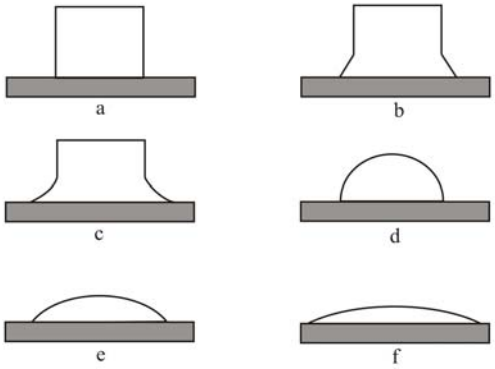

Figure 2.17: Schematic representation of melting process of silicon and its spreading on the graphite substrate. (a) before melting; (b) start of melting; (c) during melting; (d) complete melting; (e) during spreading and (f) stabilization [Li & Hausner, 1996].

Li & Hausner [1995] used commercial graphite materials with various surface roughnesses as substrates, and the contact angles were measured at 1430°C. The effect of substrate roughness on the wettability in metal/ceramic systems has been the object of several studies. Wetting and flow in well-wetted (usually reactive) systems is enhanced by roughening, while that of poorly wetted systems (non-reactive) is impeded by roughening [Naidich, 1981]. As can be seen from Figures 2.18 and 2.19, surface roughening enhances the wetting of graphite materials by molten silicon.

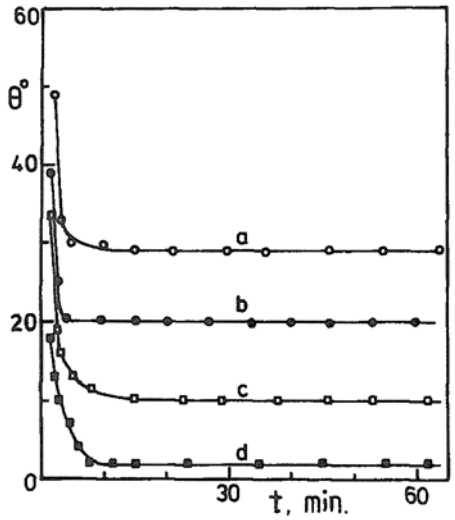

Figure 2.18: Time-dependent variation of the contact angle of silicon on graphite N with different surface roughness R_a. (a) R_a = 0.005 μm; (b) R_a = 0.30 μm; (c) R_a = 1.70 μm and (d) R_a = 3.18 μm [Li & Hausner, 1995].

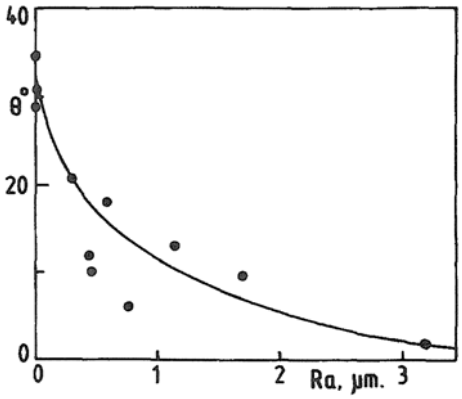

Figure 2.19: Stationary contact angle of silicon on graphite N as a function of substrate roughness R_a [Li & Hausner, 1995].

The infiltration of silicon into the graphite takes place within a depth noted by H. In addition, a lateral infiltration (see Figure 2.20) is observed, and the infiltrated distance measured from the solid-liquid-vapor three phase line is noted by D.

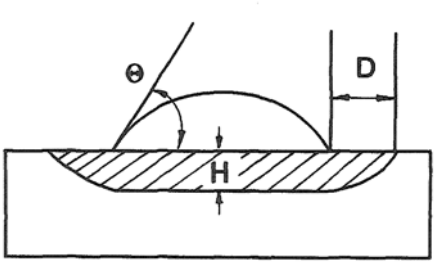

Figure 2.20: Schematic presentation of the cross-section of the silicon/graphite interface.

The measured values of H and D from a number of samples with different porosities and pore sizes are plotted in Figure 2.21 as a function of the stationary contact angles. The vertical infiltration depth H is about 0.9 ± 0.15 mm and seems to be independent on the contact angles. The vertical infiltration depth is different for different types of graphite materials (Table 2.4). These results seem to indicate that the vertical infiltration depth increases as the porosity (or pore size) of the graphite materials is increased [Li & Hausner, 1995]. The lateral infiltration distance D increases as the contact angle θ decreases. Similar results were also achieved with other graphite

materials. The lateral infiltration distance-versus-contact angle relationship follows the curve shown in Figure 2.21. Table 2.5 shows a summary of the results from various authors for graphite and glassy carbon materials.

Table 2.4: Mean values of the open porosity, pore size of various graphite materials, and the vertical infiltration depth H (lower and upper limit values) of the materials by silicon [Li & Hausner, 1995].

Graphite	Porosity [%]	Pore size [μm]	Depth H [mm]
CB620	17.02	0.05	0.40 – 0.75
UT87	17.72	0.07	0.80 – 0.95
EK77	18.65	0.10	0.95 – 1.25
N	17.77	0.06	0.85 – 1.05

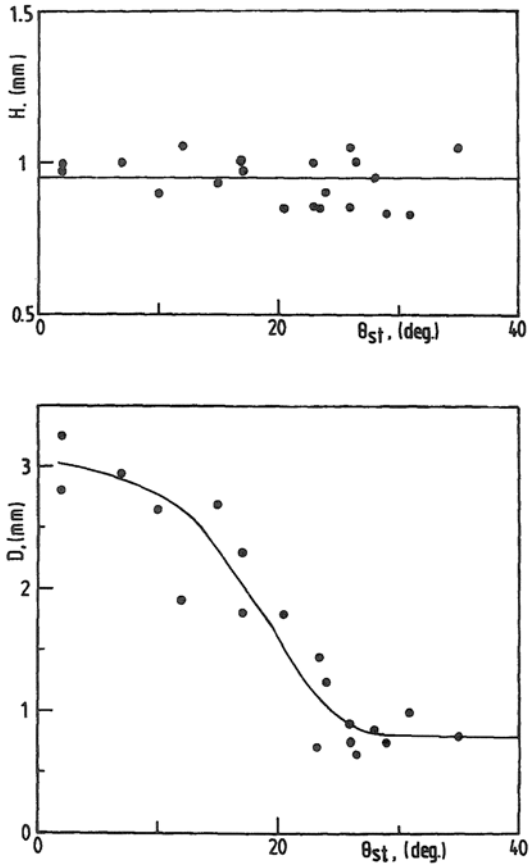

Figure 2.21: Vertical infiltration depth H and lateral infiltration distance D of silicon into the graphite N as a function of the stationary contact angles [Li & Hausner, 1995].

Table 2.5: Equilibrium contact angles of liquid silicon on carbon materials. The average roughness R_a is indicated when reported by authors.

	Li & Hausner [1995], [1996]	**Dezellus [2005]**	**Whalen & Anderson [1975]**	**Naidich [1998]**
Glassy carbon	10 - 40° (R_a < 0.005 μm)	36° (R_a = 5 nm)	40 - 50°	
Graphite	3° (R_a = 3.18 μm) 35° (R_a = 0.005 μm)	35 – 40° (R_a = 2 - 4 nm)	5 – 15° (pyrolytic graphite)	15°

2.4.2 Wettability of silicon with silicon carbide

Wetting properties of molten silicon with silicon carbide materials have been shown great interest and widely studied by many authors. Nikolopoulos *et al*. [1992] has employed the following SiC materials as substrates in their study:

(a) High-dense sintered α-SiC;

(b) α-SiC single crystals;

(c) β-SiC deposited by the CVD method on graphite substrate.

In situ formation of sessile drop technique measurements of the contact angle θ, were carried out in a purified argon atmosphere. In the system SiC-Si with various silicon carbide substrates, a good wettability is observed and the contact angle is independent of annealing time (Figure 2.22). For mono- as well as polycrystalline α-Si the θ values are quite similar, i.e. about 38° at temperatures near the melting point of silicon. This value agrees reasonably well with results reported by Wahlen & Anderson [1975] (40 ± 5° in vacuum at 1750 K), Naidich *et al*. [1998] (36° in vacuum at 1750 K) and, Yupko & Gnesin [1973] (33 - 37° in vacuum at 1720 K). The same value for the contact angle is reported by Li & Hausner [1991], [1992] too (38° at 1703 K).

Some deviation from this value, i.e. 41.5°, is observed for the β-SiC [Nikolopoulos *et al*. 1992]. This material was produced by the chemical vapor deposition (CVD) process with a roughness R_a = 0.5 μm.

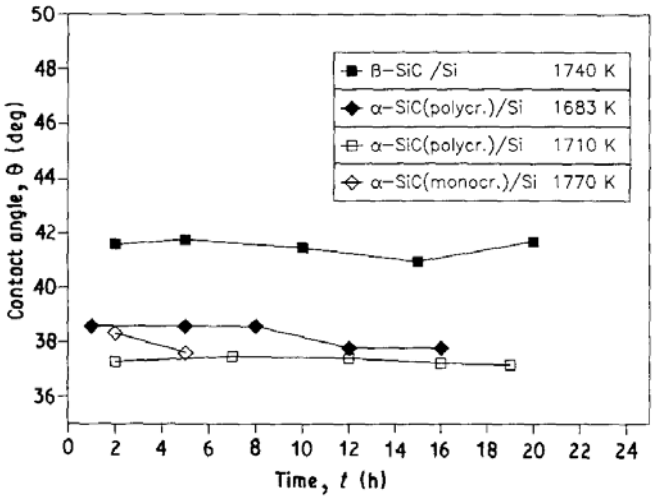

Figure 2.22: Time dependence of the contact angle for Si on various SiC substrates [Nikolopoulos *et al*. 1992].

Mukai & Yuan [2000] and Yuan *et al*. [2004] reported a low value for the contact angle of 8° at 1693 K under argon gas ($P_{O_2} \approx 10^{-21}$ MPa). The contact angles for the Si(l)/SiC(s) are shown in Table 2.6.

Table 2.6: Contact angle of liquid silicon on SiC

Material	Temp [K]	θ [°]	Reference
α-SiC	1683 - 1770	38	Nikolopoulos
	1750	40 ± 5	Wahlen and Anderson
	1750	36	Naidich
	1720	33 – 37	Yupko and Gnesin
	1703	38	Li and Hausner
β-SiC	1740	41.5	Nikolopoulos
	1693	8	Mukai and Yuan

Chapter 3

EXPERIMENTAL PART: MATERIALS, METHODS AND EQUIPMENT

In this chapter, the experimental set-up for settling, filtration and wetting experiments and the experiments carried out are presented. Methods and techniques employed to characterize the top-cut silicon scrap, Solsilc silicon, and graphites materials are given here together with the respective results. They include characterization by light and electronic microscopy, EPMA, etching procedures. A brief overview of the devices for chemical analysis including GDMS and LECO is also included.

3.1 Equipment

3.1.1 Furnaces and experiments

3.1.1.1 Settling experiments – Crystalox furnace

Two settling experiments were performed in a pilot scale Crystalox DS 250 furnace (Heliosi), shown in Figure 3.1. About 12 kg of Solsilc silicon was melted in each experiment, producing two cylindrical ingots named FS4A and FS4B with a

diameter of 250 mm and a height of about 100 mm. Silica crucibles with the inner crucible walls coated with silicon nitride were used. Since silica becomes soft at high temperatures, the crucible is supported by a graphite plate beneath and a graphite ring at the side. Heat is transferred to the silicon charge by graphite susceptors, positioned as shown in Figure 3.1, which are heated by an induction field. A thermocouple which is used for controlling the power input (susceptor temperature) is placed in the vertical susceptor. The temperature is also measured in the pedestal beneath the crucible (pedestal temperature). The susceptor is surrounded by carbon fiber insulation to reduce temperature losses to the surroundings.

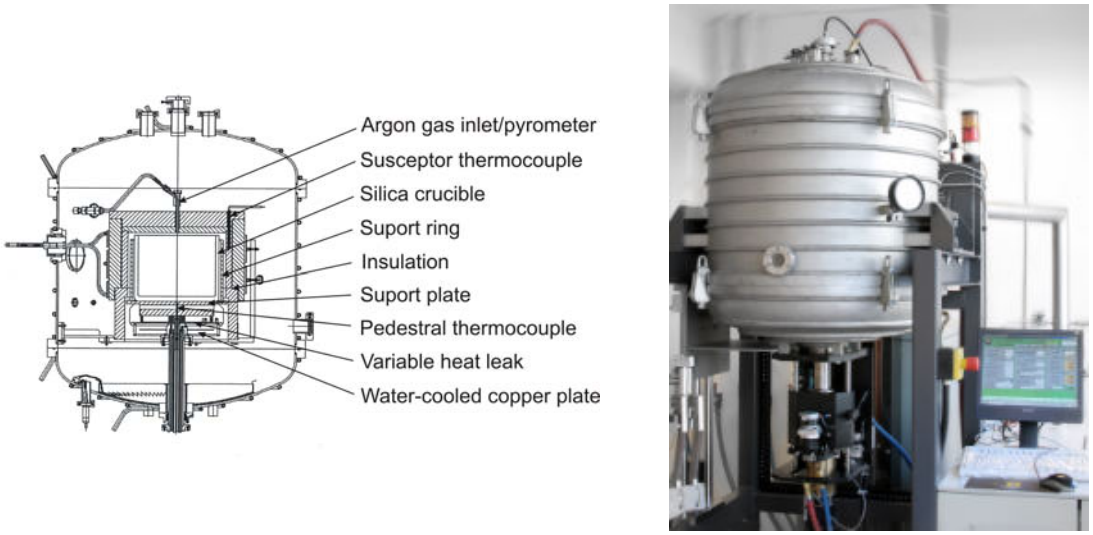

a) b)

Figure 3.1: a) A sketch of the Crystalox furnace; b) view of the furnace [Kvande, 2008].

The detailed heating program that was conducted during the settling experiments is:

1. The furnace is evacuated to a pressure of 0.08 mbar.
2. Heating to 1000ºC at 200ºC /hr. The susceptor temperature is kept constant for about one hour.
3. Argon industrial grade 4.0 (99.99% pure) is purged into the furnace at a rate of 2 l/min to reach atmospheric pressure. The argon atmosphere is retained

during the experiment. The gas in the furnace is continuously replaced by clean argon gas. The temperature is raised to 1200ºC at a rate of 300ºC/hr.

4. Temperature is raised to 1510ºC at a rate of 250ºC/hr.
5. Temperature is raised to 1535ºC at a rate of 20ºC/hr and is kept at this temperature for two hours. At the end of this period, all the silicon in the furnace has melted.
6. The settling starts. The temperature is increased to 1550ºC at a rate of about 15ºC/hr and is kept at this temperature for one hour.
7. Temperature is reduced at 15ºC/hr until reaching 1475ºC. At the end of this period the directional solidification from the bottom of the crucible starts.
8. This is the transition period during the solidification step when the temperature is reduced to 1425ºC at a rate of about 5ºC/hr.
9. Temperature is reduced at a rate of 5ºC/hr to 1380 ºC. Solidification is completed and is either detected by pyrometer readings (automatically) or by studying the power consumption.
10. Temperature is reduced to 1385ºC at a rate of 50ºC/hr.
11. Temperature is reduced to 1100ºC at a rate of 200ºC/hr and is kept at this temperature for one hour (annealing).
12. Temperature is reduced to 1080ºC at a rate of 100ºC/hr. When this temperature is reached, the power is turned off.

The temperature profile together with the melting, settling and the solidification periods are shown in Figure 3.2. Settling takes place for about 9 hours, and directional solidification of the silicon from the bottom of the crucible to the top follows. Reduction of the temperature is accomplished by opening a variable heat leak (VHL) beneath the crucible. The VHL consists of two identical insulating carbon-fiber disks with holes which are placed on top of each other. In closed positions the holes in the two discs do not coincide. By rotation of the bottom disk the openings are gradually revealed. Below the VHL is a water-cooled copper plate, and by opening the VHL the cooling from below becomes more effective.

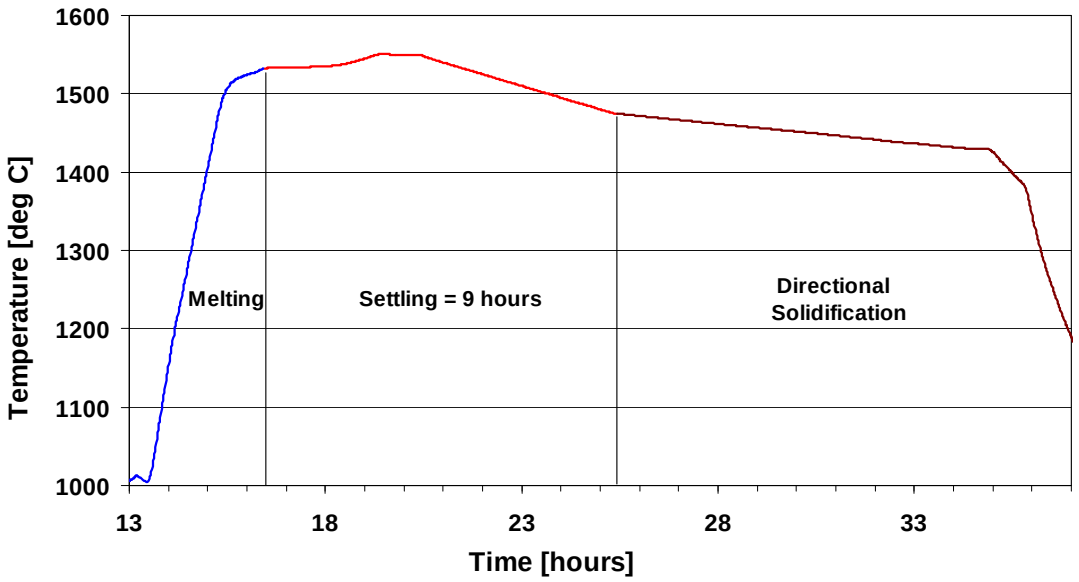

Figure 3.2: Susceptor temperature profile in the furnace during experiments.

3.1.1.2 Furnace for filtration experiments

In the filtration experiments a high vacuum furnace was employed. Figure 3.3 shows two pictures from the furnace, one from outside of the furnace and the other inside the furnace chamber. The furnace is equipped with a rotary pump and a diffusion pump which serve to give high vacuum. In our experiments, vacuum of 1×10^{-3} mbar is reached only using the rotary pump; therefore the diffusion pump is not employed. Temperature is measured by thermocouples placed inside the crucible while the heat generating current supplied in the furnace is adjusted manually at the power supply control (Figure 3.3-a). As it is seen from Figure 3.3-b), the furnace houses the heating coil where a graphite crucible wrapped with carbon felt is placed. The furnace has windows for observing the crucible during the experiments. The furnace is water cooled to prevent the induction coil and the walls of the furnace from over-heating. The crucible is designed to hold the filter with the silicon pieces placed above the filter. After filtration the molten silicon passes through a hole with diameter 8 mm at the bottom of the crucible and is collected in a cold copper bowl. The copper bowl causes silicon to solidify immediately. The design of the crucible allows removal of the filter after the experiment so that the crucible can be reused. The crucible is designed not to

crack due to movement and expansion of the silicon pieces during heating and melting. This is why the crucible gets narrower at about the middle of its depth where the diameter of the hole equals that of the filter. A sketch of the filter unit that shows the arrangement of the filter and the silicon pieces inside the crucible is shown in Figure 3.4.

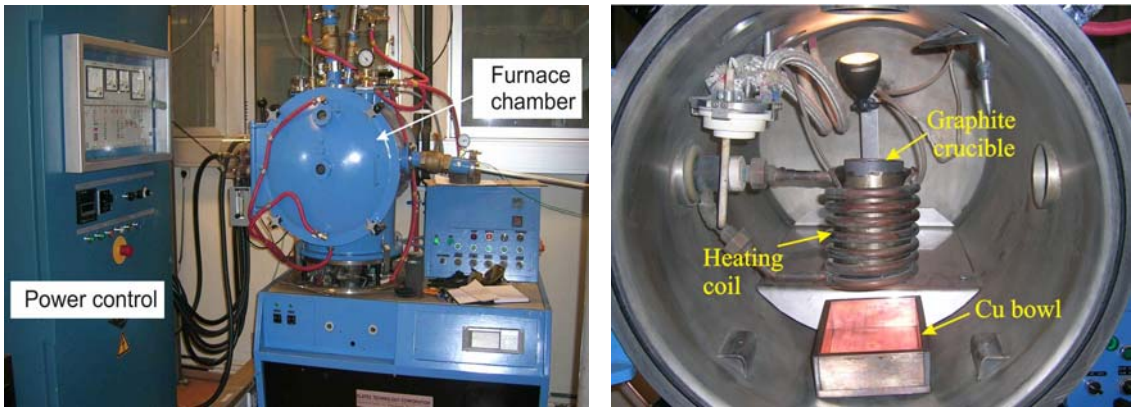

Figure 3.3: a) View of the furnace showing the furnace chamber, power and vacuum control; b) view from the inside of the furnace chamber showing the arrangement of the heating coil, crucible and copper bowl.

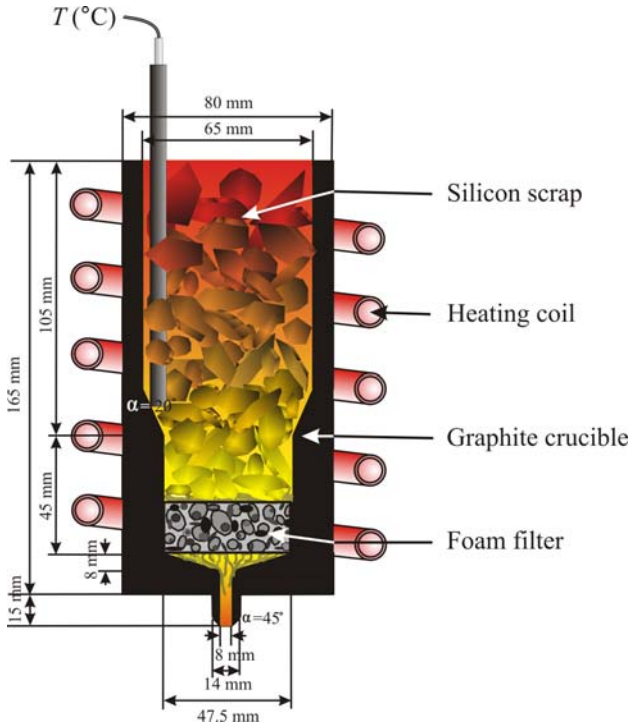

Figure 3.4: A sketch of the filtration experimental set-up showing the arrangement of the crucible, silicon and the filter.

The detailed experimental procedure followed during the filtration experiments is:

1. The crucible with the filter placed inside (see Figure 3.4) and the silicon pieces placed on top of the filter is mounted inside the heating coil of the furnace.
2. Using a rotary pump, a vacuum of 1×10^{-3} mbar is reached in the furnace chamber.
3. The furnace is filled with argon gas up to a pressure of about 650 – 700 mbar.
4. The power is turned on, and the temperature is raised to 1450 - 1500ºC.
5. The silicon melts, flows through the filter and is collected in the copper bowl. When the crucible is empty, the power is turned off.
6. After about one hour the furnace is opened, and the filtered silicon is taken from the cupper bowl.

3.1.1.3 Furnace for wettability experiments – Sessile drop technique

To study the wetting properties of the molten silicon with various refractories the sessile drop method is employed. The experimental equipment used to measure the contact angle by the sessile drop method consists essentially of a graphite tube which is located horizontally inside a high-temperature furnace. Figure 3.5 shows the open furnace with the element in the centre. A schematic diagram of the experimental set up is also shown in Figure 3.6. All of the heated furnace parts, including the element and heat shields, are constructed of graphite, allowing both extremely fast and slow heating or cooling rates. It is possible to heat the sample to 1600°C in 1 minute in either a vacuum, inert or reducing gas. The maximum temperature of the furnace is 2400°C, and it is controlled using a Keller PZ40 two color pyrometer operating from 900 to 2400°C focused on the edge of the graphite sample holder. A fire-wire digital video camera (Sony XCD-SX910CR) with a te1e-centric lens (Navitar 1-50993D) is used to record images from the sample at 960 × 1280 pixels. A Cambridge Sensotec Rapidox 2100 (with accuracy from 10^{-17} ppma to 100% O_2) was used to continually measure the partial pressure of oxygen in the gas outlet during the experiments.

The furnace was designed to study the contact angle and the interaction between a small liquid sample and a substrate with the maximum size of 10 mm in diameter and 2 to 5 mm height. The liquid drop must be small enough to sit on top of the substrate without touching the edges, with a typical sample mass of 10 - 50 mg.

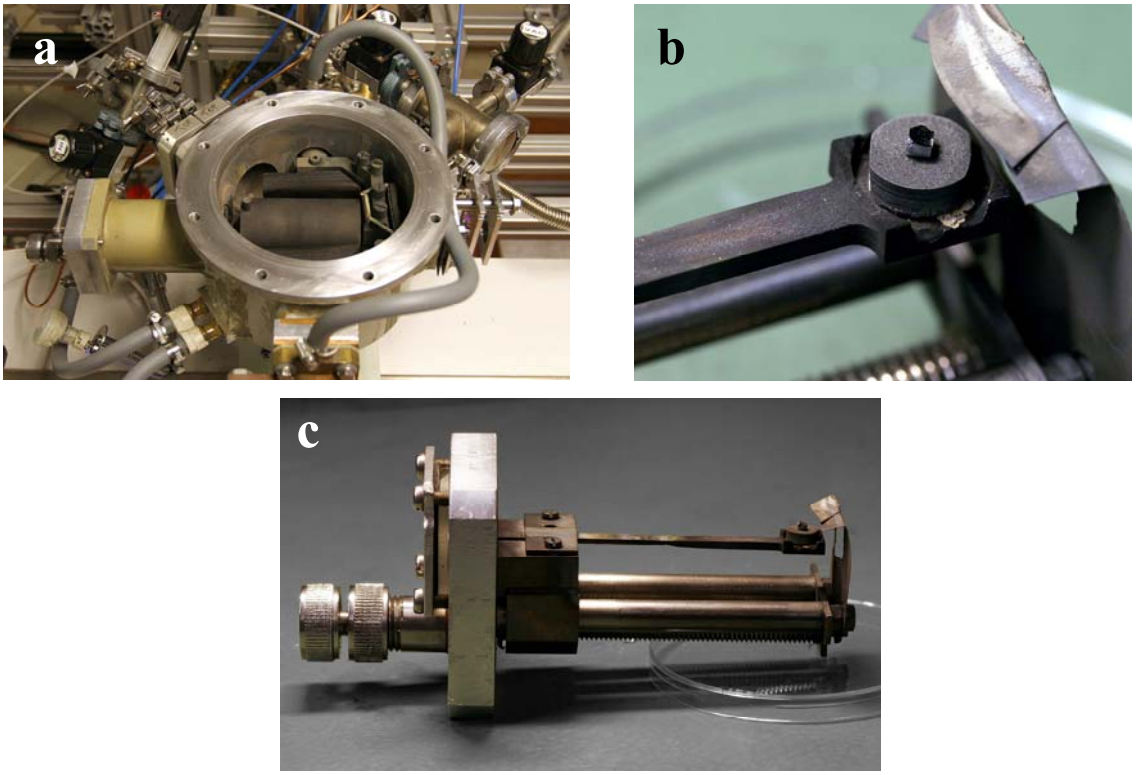

Figure 3.5: a) View of the wettability furnace used for measuring of contact angles, b) Silicon piece on a graphite substrate, c) Sample holder (photos: M. Gaal).

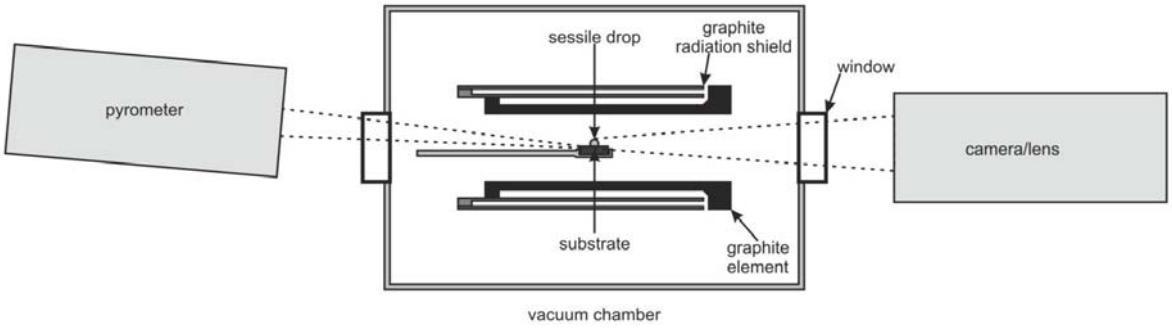

Figure 3.6: Sketch of the wettability furnace and experimental set-up.

Scientific grade argon gas (6.0), with 99.9999% Ar, was purified by an Alltec gas purifier All-Pure N2 Purifier PN 7009 combined with a Hydro Purge II type. This has the ability to remove moisture, oxygen and hydrocarbons. The content of water and oxygen in the outlet is stated to be < 1 ppb. Afterwards the argon gas runs through a furnace with Mg turnings at a temperature of 400°C which reduces further the oxygen content. The purified argon at a flow rate of 500 ml/min was used as the inlet gas to the vacuum chamber. The experiments were carried out at a pressure of 80 – 100 mbar. At the melting point of silicon the oxygen levels ranged from 5.0×10^{-22} bar to 1.0×10^{-23} bar.

The procedure used in the wetting experiments is:

1. The substrate was placed in the graphite sample holder and a silicon particle was positioned on the substrate.
2. The furnace chamber was evacuated initially down to a pressure of 2×10^{-2} mbar and then backfilled flushing purified argon till the O_2 level in the atmosphere reached a value of 10^{-18} atm.
3. The furnace was heated to 900°C in approximately 6 minutes.
4. A constant heating rate of 30°C/min is applied till the temperature of 1400°C is reached. At this temperature the O_2 level reaches 10^{-23} atm.
5. The heating rate is changed to 5°C/min till the temperature of 1500°C is reached, and there the temperature was kept constant for 20 - 30 minutes.
6. The power was turned off, and after one hour the sample was removed from furnace.

3.2 Characterization and analyzing techniques

3.2.1 Mechanical preparation of the samples

Before submitted to light and electronic microscopy, samples from Solsilc silicon before and after settling experiments and from top-cut silicon before and after filtration experiments were taken randomly, molded into resin, ground with SiC papers (mesh 80 to 4000) and polished with diamond paste of 1 μm. Afterwards, the samples were cleaned with soap, water and ethanol and were dried in hot air.

After the wetting experiments, the graphite substrates with the silicon drop on the top surface were cut in half after being molded in resin. The cutting plane passes through the middle of the substrate and the silicon piece as shown in Figure 3.7. Then the part of the sample called "observation plane" was ground and polished through the same procedure as mentioned before for silicon samples.

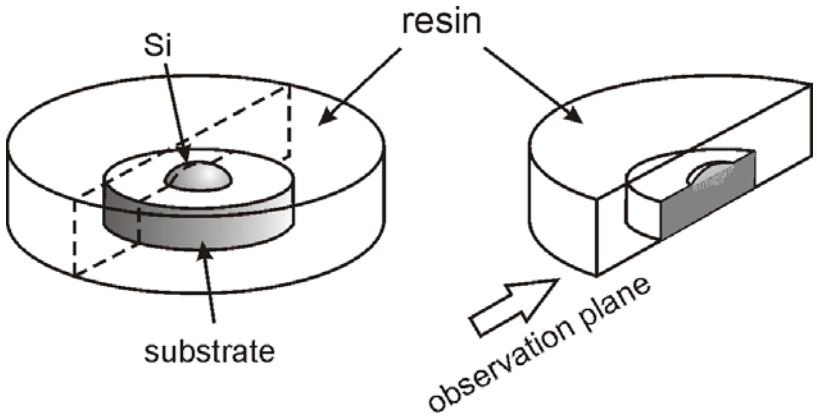

Figure 3.7: Sketch of sample preparation for wetting experiments analysis.

3.2.2 Etching and dissolution of silicon

It was necessary to study the morphology and structure of the inclusions inside the top-cut silicon scrap before and after filtration experiments and also inside the filter material. Therefore, the silicon samples were etched in an acid mixture. The standard leaching agent already established for etching and dissolving solid silicon consists of HF (40%), HNO_3 (65%) in a ratio of 1:3 parts in volume. This acid mixture dissolves silicon whereas the solid particles of SiC and Si_3N_4 are left behind [Søiland, 2004]. The dissolution of the silicon matrix proceeds by the following reactions:

$$Si + 4HNO_3 = SiO_2 + 4NO_2\,(g) + 2H_2O \quad (3.1)$$

$$SiO_2 + 6HF = H_2SiF_6\,(l) + 2H_2\,(g) \quad (3.2)$$

After being cleaned with distilled water and ethanol and dried with hot air, the samples were submitted to light and electronic microscopy. No mechanical preparation of the sample was performed.

For the wettability experiments, the silicon pieces were etched with the same acid mixture for 1 minute before the experiments. This was done in order to remove the impurities that may be present at the surface after the mechanical preparation.

3.2.3 Characterization of inclusions by light microscopes

In this study, the content of solid inclusions (SiC and Si_3N_4 particles) in silicon materials was measured. Two different techniques are employed to measure the particle size distribution of these particles. The first technique measures the particle size distribution of the extracted inclusions from the silicon matrix, whereas the second one measures the inclusions found in mechanically polished silicon samples. These techniques are described in more detail in the following paragraphs where light microscopes are employed to measure the equivalent diameter. Equivalent sphere description based on the particle projected area is employed both for SiC and Si_3N_4. Using light microscopes, the projected area of a particle is measured and is converted to the equivalent projected area of a sphere. Hence, the diameter of this sphere is the so-called equivalent diameter of the inclusion.

3.2.3.1 Inclusion count by light automated microscope (Bead Check 830)

The technique consists of dissolving a known quantity of silicon scrap in the acid mixture as described in Section 3.2.2 and collecting all the inclusions. A light automated microscope (Bead Check 830, Figure 3.8), designed to analyze size and shape of particles and granular objects, is used to count the particles. The instrument consists of a mechanical unit, video camera, optics and software. The system is fully computerized and is conveniently operated using menu-based commands. The sample is placed on a glass slide, which is scanned and imaged by the instrument video camera. This takes from minutes to several hours. The dedicated software of BeadCheck 830 analyzes the images and presents the results on a screen during operation. The results can be stored for further processing. BeadCheck 830 analyses up to 80000 particles in a sample. For each particle a picture, measurement and calculations are performed to present the particles morphological data that include equivalent particle diameter, length, width, area, roundness and convexity. Results can be presented in a histogram and as statistical data. From the projected area of the particles, employing equation (3.3), the diameter of the equivalent spherical particle is calculated.

$$d_p = 2\sqrt{\frac{S_i}{\pi}} \tag{3.3}$$

where: d_p is the diameter of the equivalent particle,

S_i is the measured projected area of the inclusion.

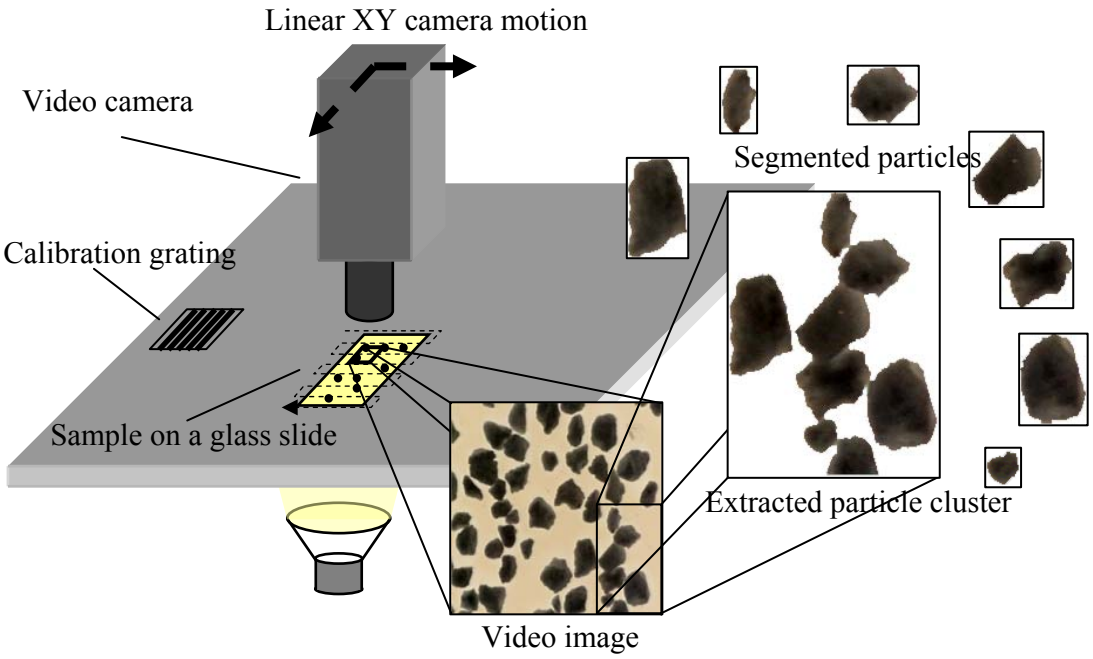

Figure 3.8: A schematic presentation of the photo microscope used for particle size analysis.

However, the procedure of collecting the solid inclusions through acid dissolution of silicon and then counting and measuring their size has the following disadvantages:

- The filters used to collect the inclusions have pore size of 2 μm. Thus, inclusions smaller than this size have probably escaped and are not collected.
- Together with the particles, also paper fibers are collected hence, influencing the inclusion size when measured by the light microscope.
- Since the particles are placed in a glass plate in an open environment other particles from dust can easily enter and be measured during the analysis thus influencing the results.

3.2.3.2 Inclusion count by standard light microscope

For the reasons mentioned above, an additional method is used to measure the particle size distribution. A standard light microscope is employed to measure the surface area of inclusions. The silicon scrap samples are randomly chosen and after being molded to resin and polished with very fine paper using 1 μm diamond spray or paste, they are submitted to light microscopy. Pictures are taken and the surface area of the inclusions is measured (see Figure 3.8).

In Figure 3.9 two pictures taken with light microscope are shown. Inclusions in these pictures have a complex shape. Thus, it is very hard to tell what the size of the particle is. However, their measured surface area is converted to the surface area of a cross section of a sphere as it is shown in Figure 3.10.

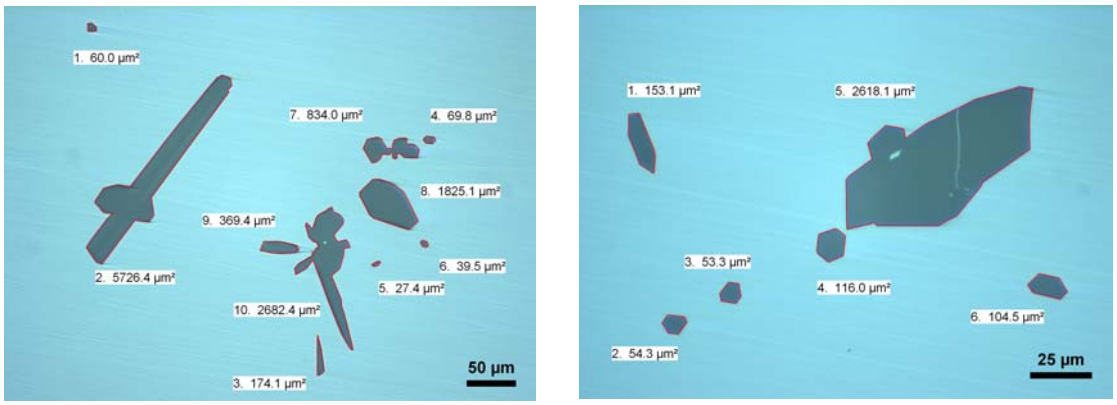

Figure 3.9: Inclusions in top-cut silicon scrap and their measured surface area.

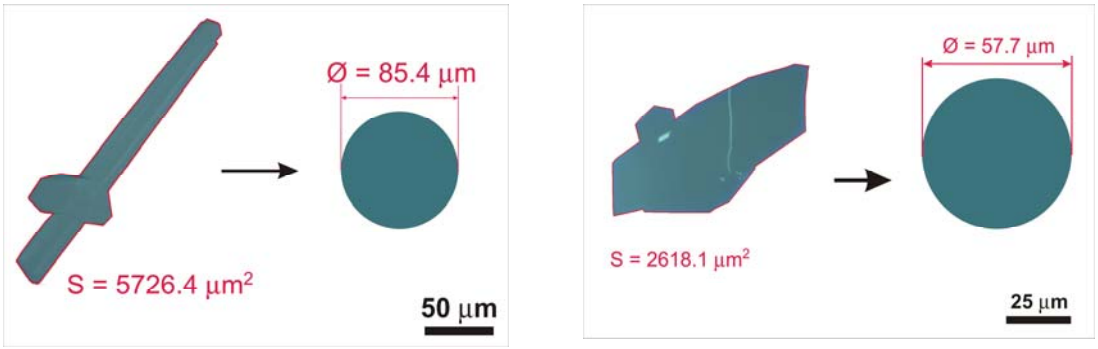

Figure 3.10: Two examples from the measurement of the particle average diameter.

Since in our analysis we have cut our samples, the measured surface area of the (spherical) inclusion corresponds to the average cross sectional area of a spherical particle sliced by a plane (see Figure 3.11). This is given by equation (3.4).

$$S_i^m = \frac{\pi}{2R}\int_{-\pi}^{\pi}(R^2 - x^2)dx = \frac{2}{3}\pi R^2 \qquad (3.4)$$

where: R is the radius of the sphere.

S_i^m is the measured surface area of the inclusion.

From the measured surface area of the inclusion, using equation (3.4), the equivalent diameter is calculated. Thus, the diameter of the equivalent spherical particle analyzed d_p is:

$$d_p = 2R = \sqrt{\frac{6S_i^m}{\pi}} \qquad (3.5)$$

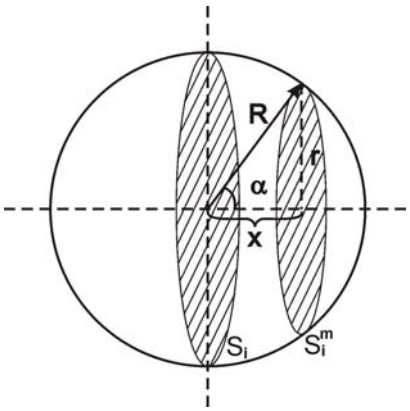

Figure 3.11: A spherical particle with radius R sliced by a plane at position x that creates a cross section area S_i^m with radius r.

The mass distribution versus mean diameter of inclusions is also calculated using equation 3.6 for the mass of the particles.

$$\text{Mass} = \frac{\pi}{6}d_p^3 \cdot \rho \qquad (3.6)$$

where: ρ is the density of the particles.

In this technique all the particles, even those smaller than 2 μm size are measured. No other particles, such as dust, are measured. However, this technique has its disadvantages:

- Only a few samples (surface areas) are investigated, thus the number of particles measured is small,
- It is time consuming.

3.2.4 Electron probe micro-analyzer (EPMA)

Mapping of silicon samples is carried out by employing EPMA. This equipment is basically a scanning electron microscope designed and optimized for X-ray analysis of elements from very small areas. EPMA is a fully qualitative and quantitative elemental analysis of micro-sized volumes at the surface of materials, with sensitivity at the level of ppm (parts per million) by mass. The JXA-8900 used for our analysis is equipped with 4 wavelength dispersive X-ray spectrometers (WDS) and an energy dispersive X-ray spectrometer (EDS). This combination can simultaneously analyze up to 12 elements and collect image signals from backscatter and secondary electron detectors [Raanes, 2005]. Mapping of silicon samples was carried out only for 4 elements, Si, C, N and O. Samples from SiC and carbon filters are analyzed also for Al content.

3.2.5 Glow discharge mass spectrometer (GDMS)

A glow-discharge mass spectrometer (GDMS) is employed to analyze the top-cut silicon scrap for the concentration level of impurities. This apparatus uses argon as the discharge gas. Argon positive ions are accelerated towards the sample surface at very high energies resulting in atomization of the upper atom layers of the sample. Atoms sputtered from the sample surface into the plasma are ionized, and ions exiting the source are analyzed by a double focusing mass spectrometer. Element concentrations are determined from the mass separated ion beam currents. This apparatus can analyze all the elements in the periodic table except H, C, N, O and S with a sensitivity of 1 ppb (part per billion).

3.2.6 LECO carbon and nitrogen analyzer

In order to measure the carbon and nitrogen content of the silicon samples a LECO carbon and nitrogen analyzer is employed. The sample is combusted in a high-

frequency induction furnace, and after that the products of combustion are passed through a catalyst where any carbon monoxide is converted to carbon dioxide. Carbon is measured as carbon dioxide in the carbon IR cell. Nitrogen on the other hand is released as N_2 from the sample and is detected using a thermal-conductivity detector. The results are adjusted for mass and calibration factors.

3.2.7 Measurement of surface roughness

Various types of graphite materials are employed as substrates with known open porosity and pore size. Their average surface roughness, R_a, is measured. Surface roughness is a measure of the finer surface irregularities in the surface texture. R_a is taken as the arithmetic average of the absolute values of the displacement of the surface valleys and peaks in microns (see Figure 3.12) and it is calculated by the following equation:

$$R_a = \frac{1}{n}\sum_{i=1}^{n}|y_i| \tag{3.7}$$

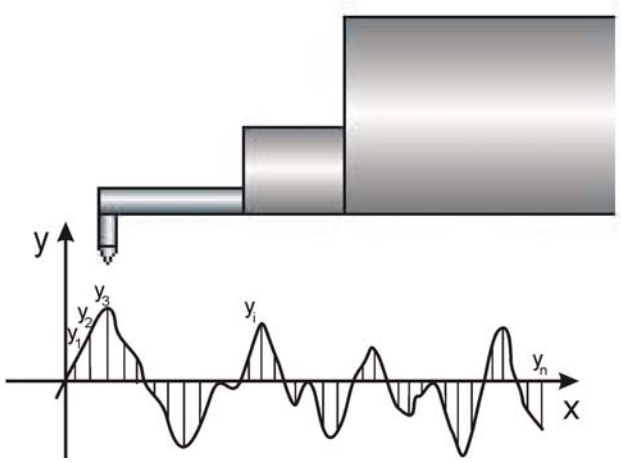

Figure 3.12: R_a is calculated as the arithmetic average of the absolute values of the peaks and valleys of the surface.

The surface roughness of cut and polished samples were measured using a standard roughness instrument (Mitutoyo SJ. 201 P/M). This instrument has a diamond needle with a very sharp tip which is in physical contact with the sample surface under a very low contact force. The roughness measurements were carried out over a length of 3

mm on the sample surface several times at different positions, and then the average roughness of each sample (R_a) was calculated.

3.3 Materials

3.3.1 Solsilc silicon – raw material for settling experiments

Solsilc is a route to SoG-Si developed by Sintef in cooperation with Fesil. Use of clean raw materials in SoG-Si production is the key idea in this process. A sketch of the Solsilc process is shown in Figure 3.13.

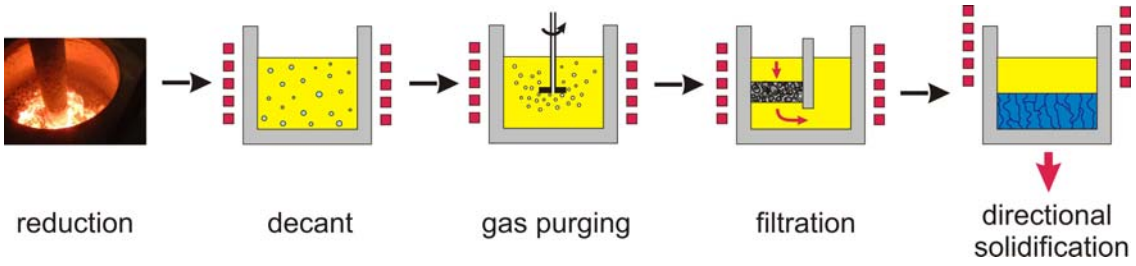

Figure 3.13: Sketch of the Solsilc process.

In the Solsilc concept, solar grade silicon is produced from clean raw materials to give high purity material directly from the reduction furnace. Fe, Ti and Al are reported to be less than 0.1 ppm by mass. However, a major problem for the final product is the high content of carbon present as SiC inclusions with size from 1 – 30 μm. The SiC inclusions may be removed by settling. To study this, settling experiments are performed with Solsilc material initially containing about 700 mass ppm of carbon.

Samples from the Solsilc silicon are analyzed with light microscopes, SEM, X-ray and EPMA. Figure 3.14 shows two pictures taken with a light microscope and SEM. These pictures show solid inclusions which have precipitated along the grain boundaries in the silicon. Their size varies from 1 – 30 μm and they are round in shape. X-ray analysis shows that inclusions are mainly SiC particles. However, low concentration levels of oxygen and nitrogen (see Table 3.1) were also found in these particles. This suggests that inclusions consist mainly of SiC, and to a lesser extent of Si_3N_4 and SiO_2 particles.

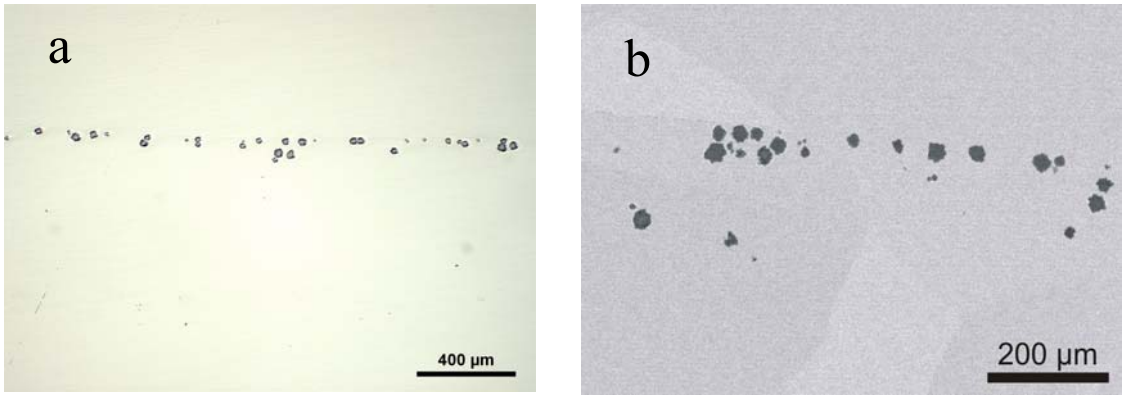

Figure 3.14: Solid inclusions in Solsilc silicon before settling experiments. a) picture taken with light microscope and b) SEM photo.

Table 3.1: Atomic concentration of elements in several solid inclusions in Solsilc silicon (EPMA analysis) before settling experiments.

Nr	Si	C	N	O
1	34.01	55.06	5.64	5.13
2	33.94	54.51	6.95	4.60
3	35.05	56.33	4.80	3.82
4	35.18	55.04	6.34	3.44
5	35.22	53.43	7.19	4.16
6	34.44	49.69	6.90	8.97
7	33.77	52.40	7.67	6.16

Mapping of SiC particles shown in Figure 3.15 was carried out by Eikevik [2008]. It displays the distribution of C, N and O over SiC particles. As it is seen from the pictures, nitrogen is found mainly around the particle whereas oxygen appears to cover the whole surface of a SiC particle. The results of the analysis indicate that SiO_2 and Si_3N_4 might serve as nucleating centers for SiC particles. These particles could have co-precipitated in the molten silicon.

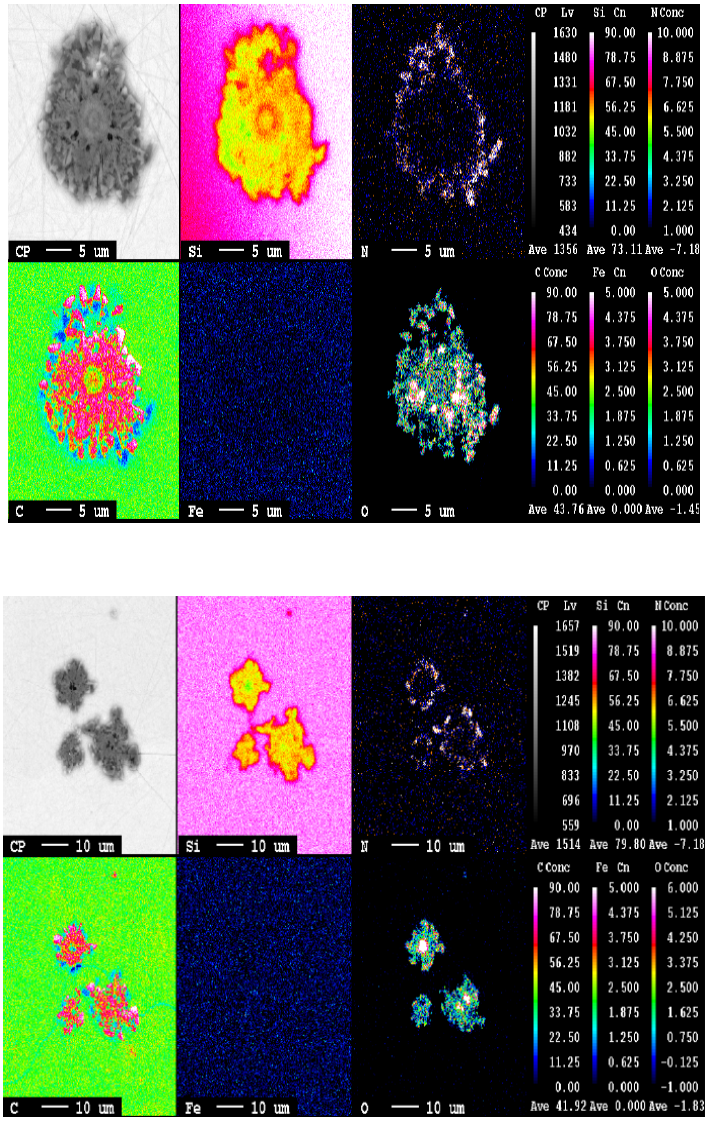

Figure 3.15: Mapping of SiC particles in Solsilc silicon by EPMA before settling [Eikevik, 2008]. The SiC particles contain also oxygen and nitrogen which might indicate co-precipitation with the SiO_2 and Si_3N_4.

Light microscopes are used to count inclusions and measure their surface area according to the procedure described in Section 3.2.3.2. From the surface area values, the equivalent diameter of the particle is calculated. The data is used to obtain the inclusion equivalent diameter distribution by number and by mass. These are shown in Figures 3.16 and 3.17.

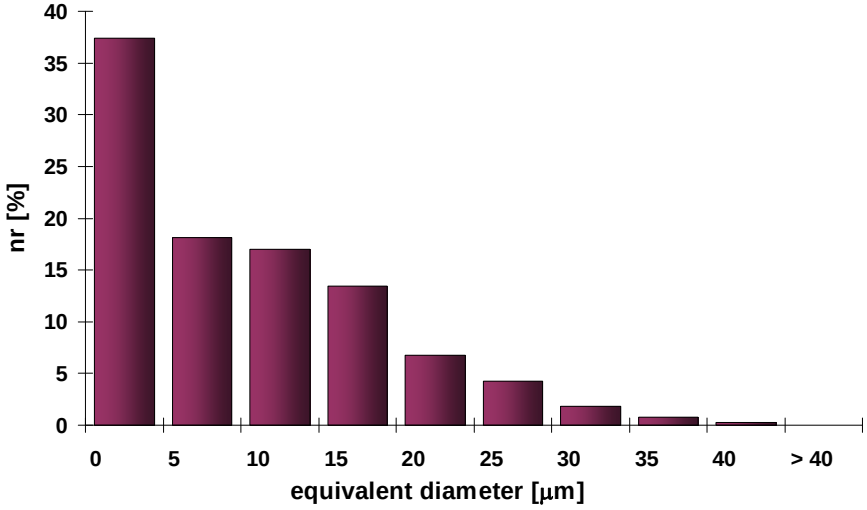

Figure 3.16: Particle mean diameter distribution by number% before settling experiments.

As one can see from Figure 3.16, the equivalent diameter of the inclusions ranges from 0 – 35 μm. The majority of the particles have a diameter of 0 – 2.5 μm. No inclusion larger than 35 μm was found. However, when the mass of the particles is considered, inclusions that lie within 20 – 25 μm give the highest contribution (see Figure 3.17).

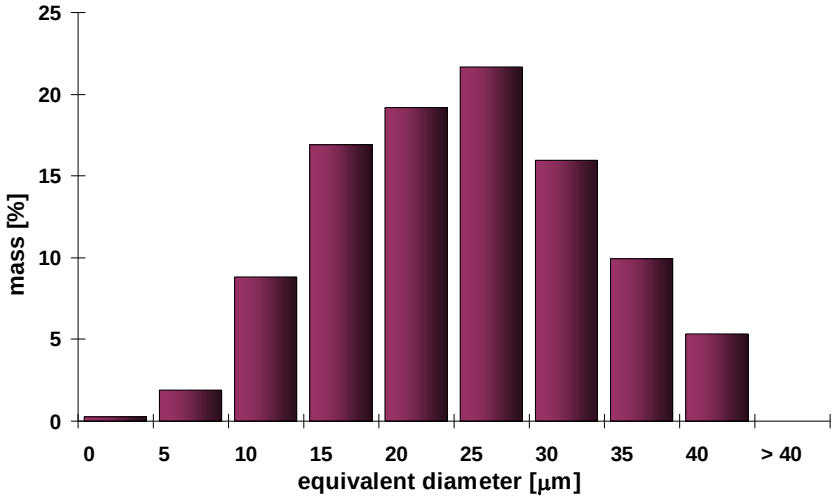

Figure 3.17: Mass% distribution of inclusions versus equivalent diameter before settling experiments.

3.3.2 Top-cut silicon scrap – raw material for filtration experiments

Multicrystalline silicon is cast in a silicon nitride (Si_3N_4)-coated quartz crucible and is then directionally solidified. Crystallization is realized by slowly moving downward the liquid silicon-containing crucible out of the inductively heated hot zone of the process chamber, as shown in Figure 1.3. This is the so-called conventional Bridgman technique that still is mainly used for the fabrication of multicrystalline ingots [Koch *et al*. 2003]. The Si_3N_4 coating, which serves as an anti-sticking layer preventing the adhesion of the silicon ingot to the quartz crucible walls, becomes a source for silicon nitride inclusions in the bulk metal. Silicon carbide particles are also present in the melt due to the previous reaction of silicon with the lining refractory and graphite heating elements over the gas phase. During directionally solidification the liquid solidifies slowly from the bottom of the crucible to the top, accumulating impurities in the liquid silicon. As a result the top of the ingot is highly contaminated with impurities such as SiC, Si_3N_4, iron, aluminum, etc. For this reason the top of the ingot is cut and sold as low value scrap.

The top-cut silicon scrap was provided by Scan Wafer ASA, a Norwegian company that produces multi-crystalline silicon wafers for PV industry. The material came in square pieces with dimensions of 150 mm × 150 mm with thickness that ranges from 10 to 20 mm. The silicon scrap pieces were broken into smaller pieces with surface areas of 1 - 8 cm^2. A view of the silicon scrap as used in filtration experiments is shown in Figure 3.18.

Figure 3.18: Top cut silicon scrap as used in filtration experiments. The square piece of silicon scrap was broken into smaller pieces before it was filtered.

3.3.2.1 Characterization of silicon scrap with light and electronic microscopy

A large part of the solid inclusions lie on the very top surface of the silicon scrap. They usually are large and easy to observe even with the free eye. Figure 3.19 shows photos taken with a SEM without any pre-treatment.

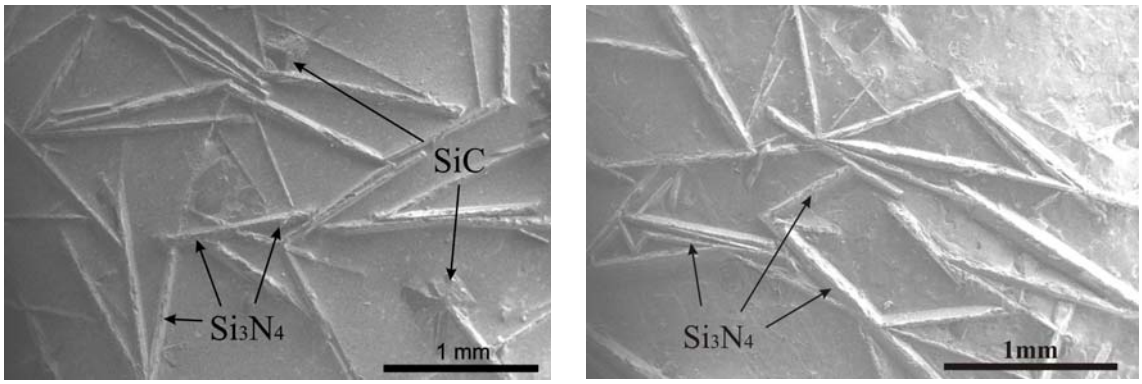

Figure 3.19: Picture of the top surface of the silicon scrap taken by SEM.

Figure 3.20 shows pictures taken by means of a photo microscope, and Figure 3.20 shows pictures taken with a SEM. These pictures present samples from the top layer of the scrap which has the highest concentration of SiC and Si_3N_4 inclusions. As it is seen from these figures, the nitrides grow into large networks. Their size can range from several micrometers to several hundreds micrometers. They can even become of

millimeter size but most of them are less than 200 µm. As mentioned in Chapter 2, the nitrides may act as nucleating centers for carbide precipitation. Examples of this are shown in Figure 3.21 and 3.22.

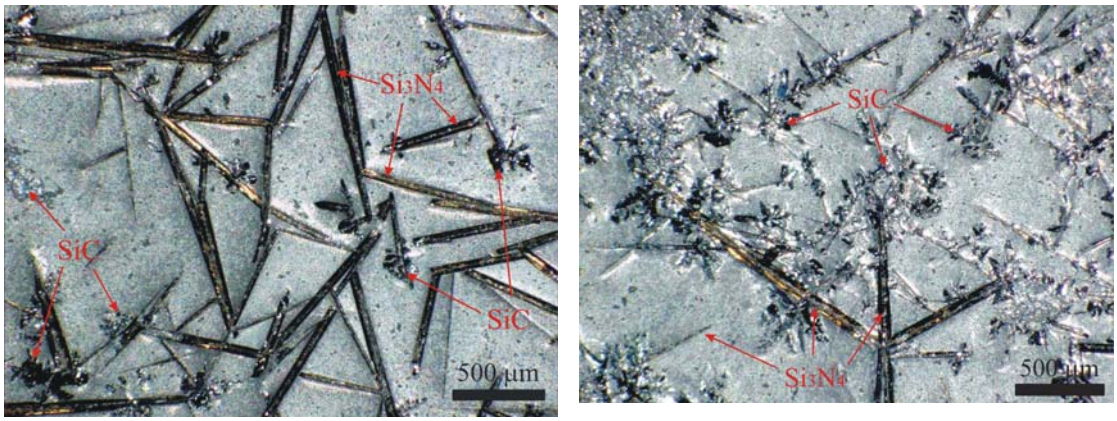

Figure 3.20: Picture taken with a photo microscope from the top surface of the silicon scrap.

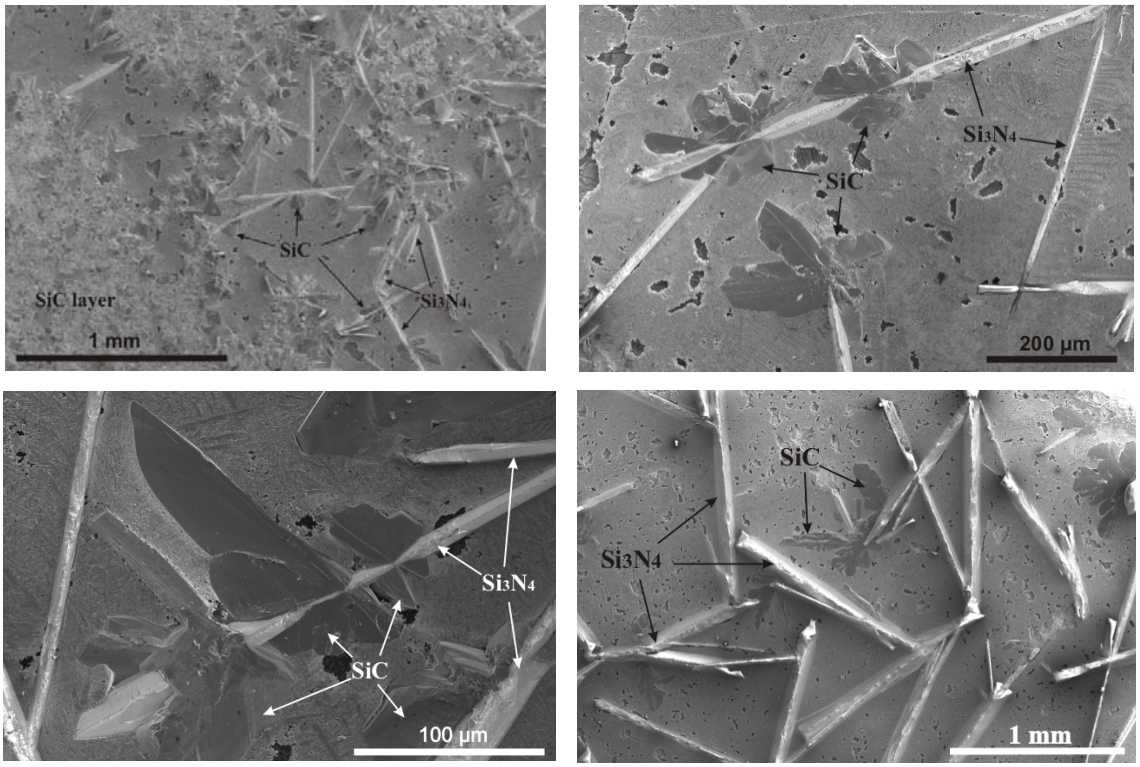

Figure 3.21: Pictures taken with a SEM from the top surface of the silicon scrap.

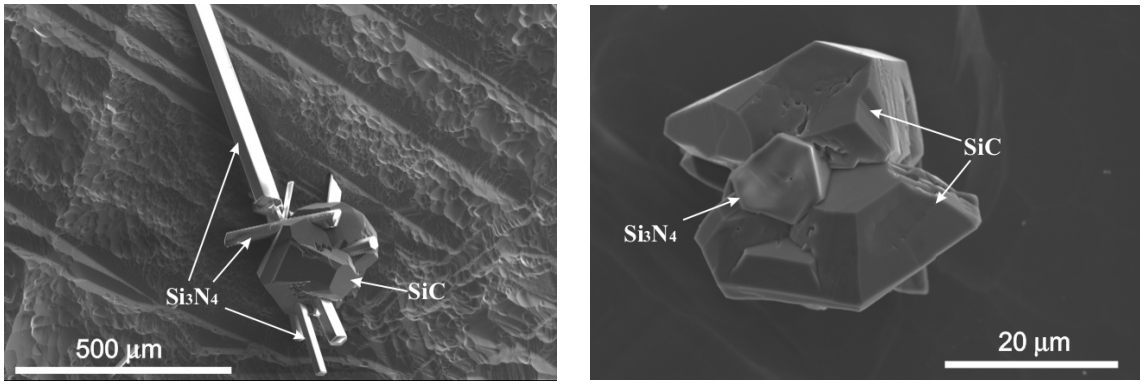

Figure 3.22: Pictures taken with a SEM from the bulk silicon scrap.

In order to observe the structure of the particles inside the silicon scrap, the samples were etched with the acid mixture as previously described for 1 hour and then, after being cleaned and dried, were investigated by SEM. Figure 3.22 and 3.23 shows some of the pictures taken.

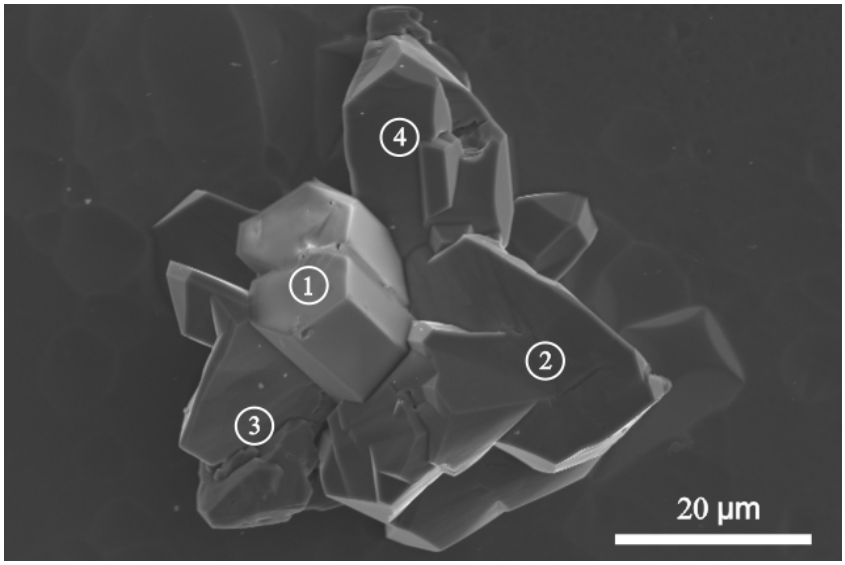

Figure 3.23: Pictures taken with a SEM showing inclusion cluster inside the silicon scrap.

Table 3.2: X-ray analysis (normalized data) of the inclusion cluster shown in Figure 3.23.

Point (1)			**Point (2)**		
Element	**Weight [%]**	**Atomic [%]**	**Element**	**Weight [%]**	**Atomic [%]**
N	50.47	67.14	**C**	38.67	59.59
Si	49.53	32.86	**Si**	61.33	40.41
Total	100.00		**Total**	100.00	
Point (3)			**Point (4)**		
Element	**Weight [%]**	**Atomic [%]**	**Element**	**Weight [%]**	**Atomic [%]**
C	28.17	47.83	**C**	37.61	58.50
Si	71.83	52.17	**Si**	62.39	41.50
Total	100.00		**Total**	100.00	

X-ray analysis was employed to analyze the particles in the clusters, thus, distinguishing the SiC from the Si_3N_4 particles. As an example, an inclusion cluster is shown in Figure 3.23 where the X-ray analysis is employed at the points denoted with numbers. The data taken is presented in Table 3.2. Before submitted to SEM the samples were carbon coated. For this reason the X-ray analysis of some particles gives a higher concentration of carbon than corresponds to the concentration of carbon in a SiC particle. On the other hand, the signal that comes from the silicon matrix interferes with that from the particles thus giving a higher concentration of silicon.

Finally a full dissolution process was carried out where all the silicon material was dissolved by the acid mixture as described in Section 3.2.2. The particles were collected on a special paper filter which resists aggressive media. Afterwards, ethanol was used to wash off the solid particles collected in a glass beaker. When the ethanol evaporated, the particles were analyzed using light and electronic microscopes to study the structure. Figure 3.24 shows SEM photos of the inclusions.

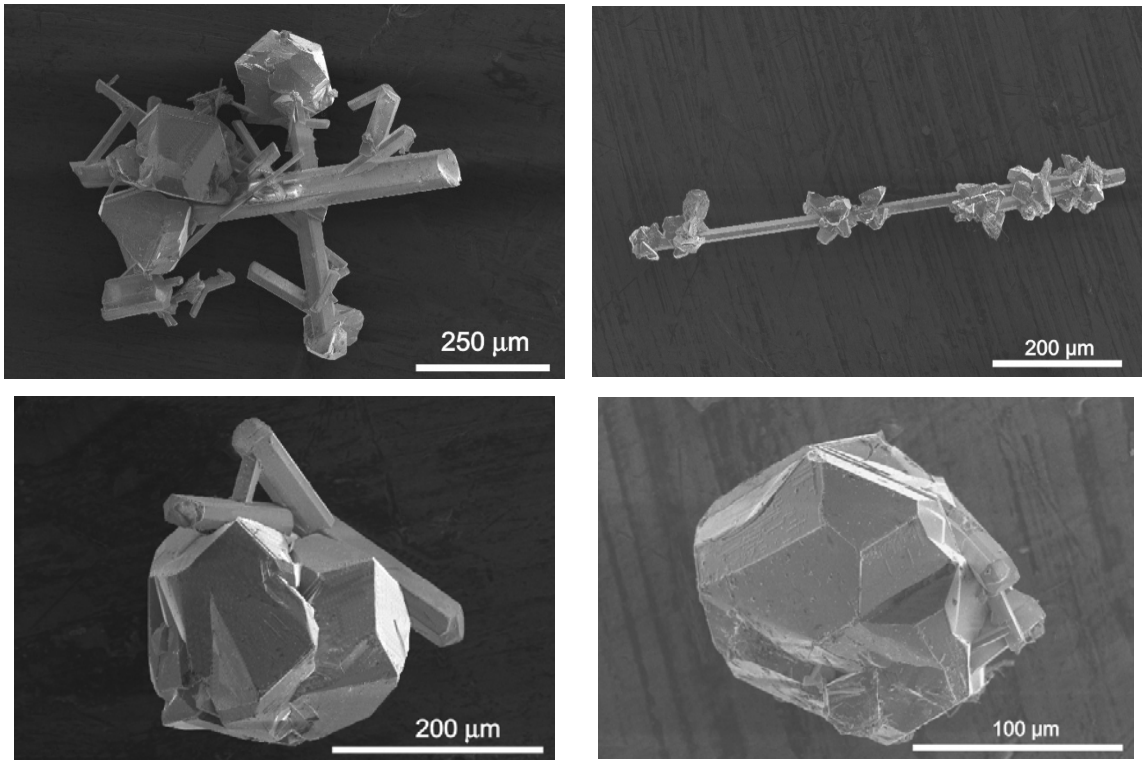

Figure 3.24: SEM pictures from inclusions after total dissolution of the silicon.

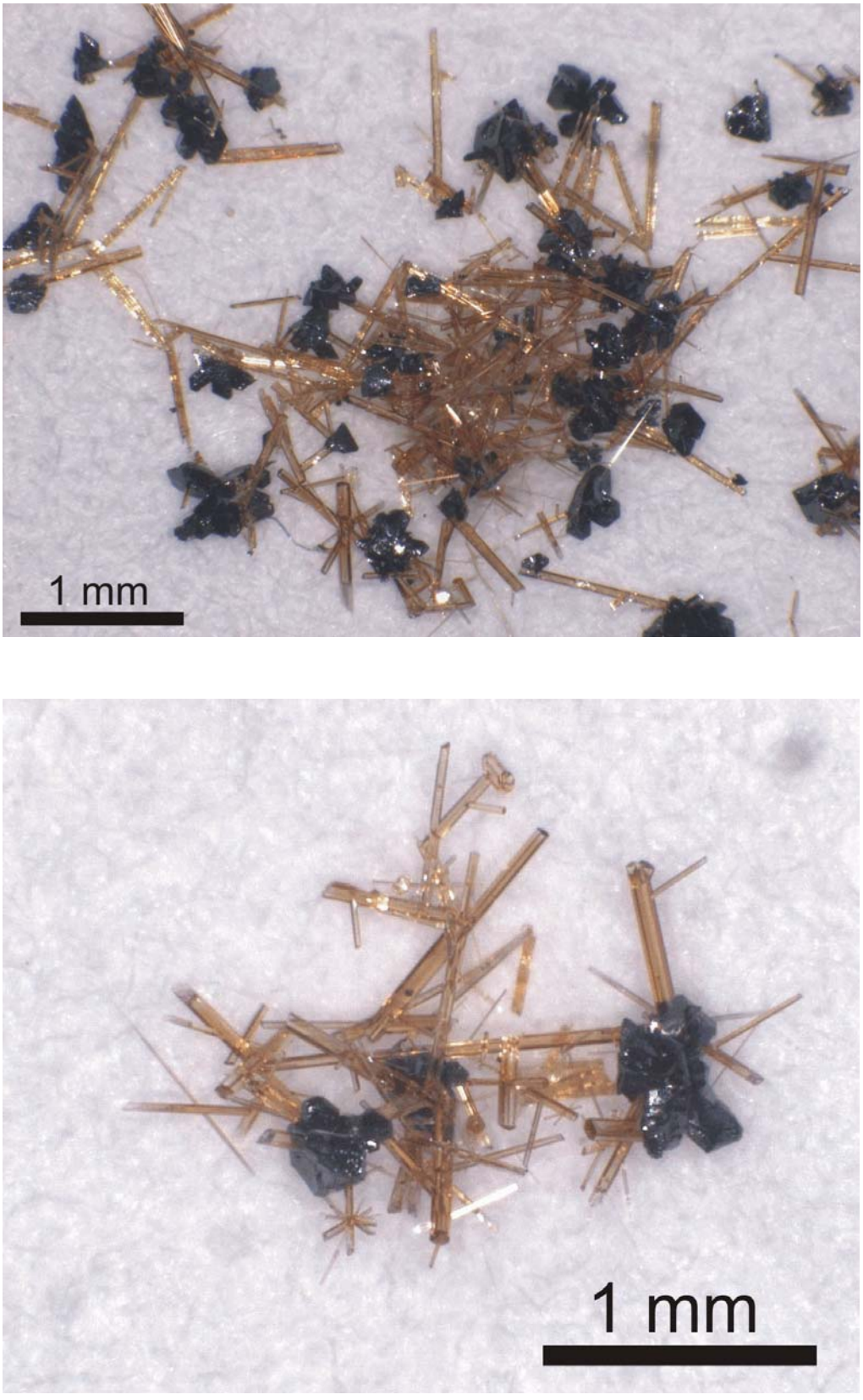

Figure 3.25: Two pictures taken with a photo microscope of the inclusions left after total dissolution of silicon scrap.

Some of the largest clusters found were analyzed by a photo microscope. Two pictures are shown in Figure 3.25. From the pictures in Figure 3.24 and 3.25 one can see that Si_3N_4 particles are rods with a hexagon base. One may note the golden color of Si_3N_4 particles. It is reported [Herrmann & Goeb, 2001] that this color comes from impurities such as Ti. SiC has a dark grey to black color. XRD analysis reported from Søiland [2004] has shown that they are β-SiC particles.

Other samples from the silicon scrap were randomly chosen, cut and molded into resin. Afterwards, they were ground with SiC paper and polished with diamond paste down to 1 µm. Light microscope and electron probe micro analyzer (EPMA) were employed to study these samples (Figure 3.26 and 3.27).

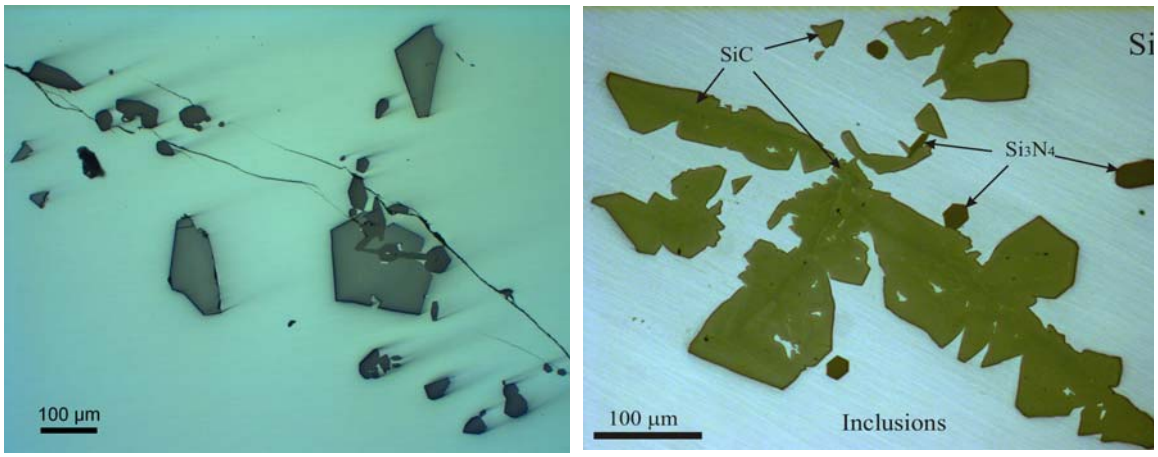

Figure 3.26: Pictures showing inclusions in the silicon scrap.

As already seen, the inclusion clusters in the silicon scrap consist of many particles, both carbides and nitrides. They have a complex shape, and it is hard to distinguish the carbides from nitrides as they tend to sinter together. Even the shape is not of much help since many small particles make up the large ones. Thus, EPMA is used for mapping of the inclusion clusters. Some of the results are shown in Figure 3.27. In this figure, mapping of the observed area shows the distribution in mass% of C, N and Si. From the results one can easily recognize the carbides and nitrides and tell the difference between them. On the right hand side of the picture in Figure 3.27, the

concentrations of the respective elements are given in mass %. The results are more of a descriptive than quantitative nature.

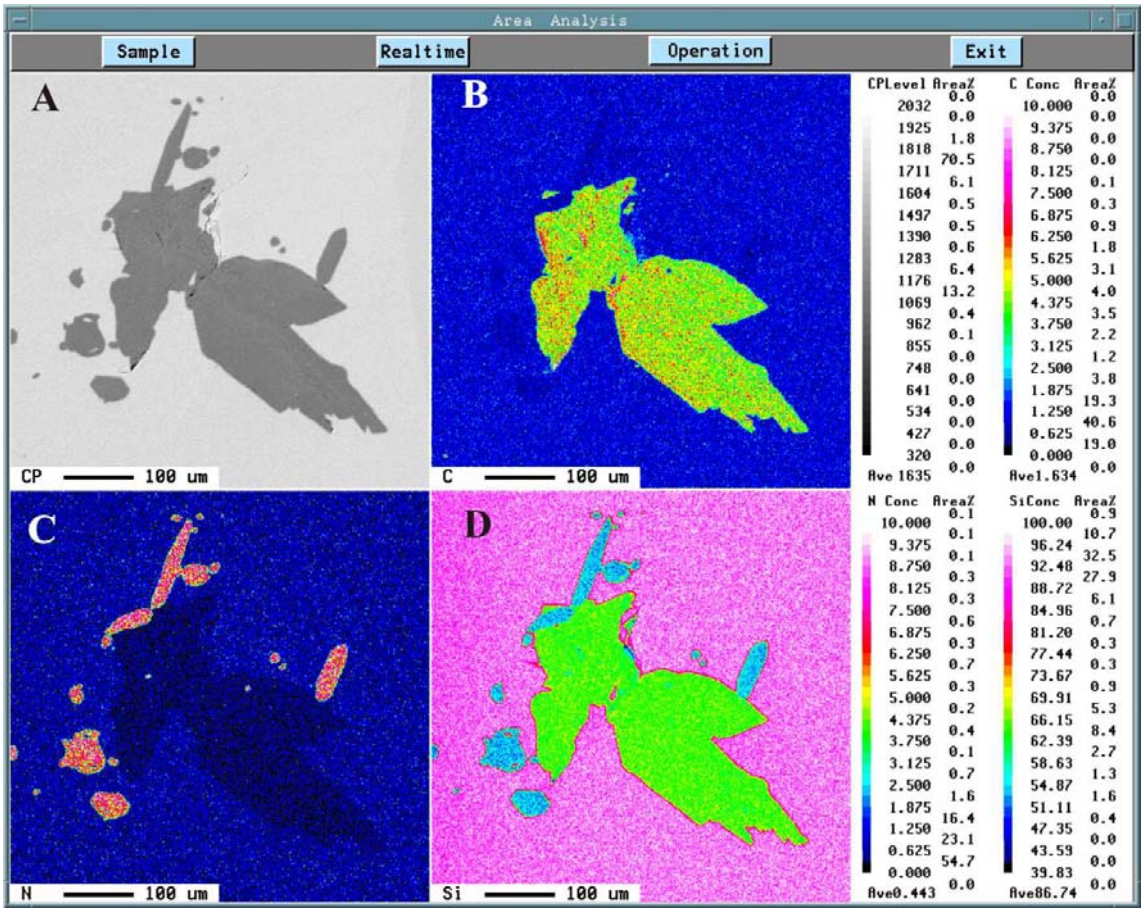

Figure 3.27: Mapping of clusters of inclusions inside the material. A) view of the inclusions cluster, B) distribution of carbon in the surface (SiC particles), C) distribution of nitrogen in the surface (Si_3N_4 particles), D) distribution of silicon. Distributions are given in mass percent (EPMA).

3.3.2.2 Particle size distribution by number and mass

Several samples of top-cut silicon scrap were dissolved in the acid mixture as shown in Section 3.2.2, and all the inclusions collected after dissolution were analyzed with the photo microscope Bead Check 830. The inclusion size distribution given as number of particles in percentage *versus* equivalent diameter is shown in Figure 3.28. From this distribution we can see that the maximum size of the particles lies in the

range size of 5 – 10 µm. Table 3.3 gives analysis data such as minimum and maximum size, means size etc.

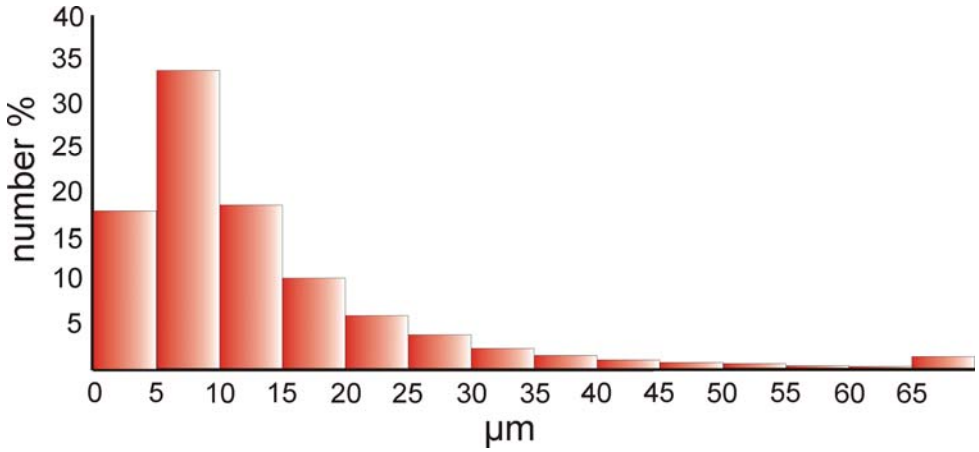

Figure 3.28: Inclusion equivalent diameter distribution by number for the first dissolved sample in Table 3.3.

Table 3.3. Results from the particle size analysis carried out for 6 dissolved samples by automated photo microscope Bead Check 830.

Total No.	Min size [µm]	Max size [µm]	Mean [µm]	Median [µm]	Nr. [%] (5 - 10µm)
10000	2.5	188.8	14.1	9.6	33.5
10000	2.6	240.9	13.6	8.9	36.5
36723	2.1	226.8	13.5	10.7	28
2470	3.0	184.3	16.5	12.1	31.5
2608	3.1	115.3	15.3	11.1	34
2315	3.5	117.7	16.3	12.0	33.5
Mean	2.8	179.0	14.9	10.8	32.8
STDV	0.5	53.0	1.3	1.3	2.9

A particle size analysis is also conducted by a standard light microscope. Hundreds of pictures were taken and the surface area of a total of 1331 inclusions and inclusion clusters were measured. From this data, the mean diameter of the particles is calculated as explained in the Section 3.2.3.2. The results are presented in Figure 3.29

where the inclusion size distribution in number% versus equivalent diameter is shown. As it is seen from this figure, this fits well with results from the first technique. About 72 % of the particles fall in the size range of 0 – 25 μm indicating that the majority are small inclusions. The calculated average size of the particles is about 25 μm and only 5 % are large inclusions with size > 75 μm.

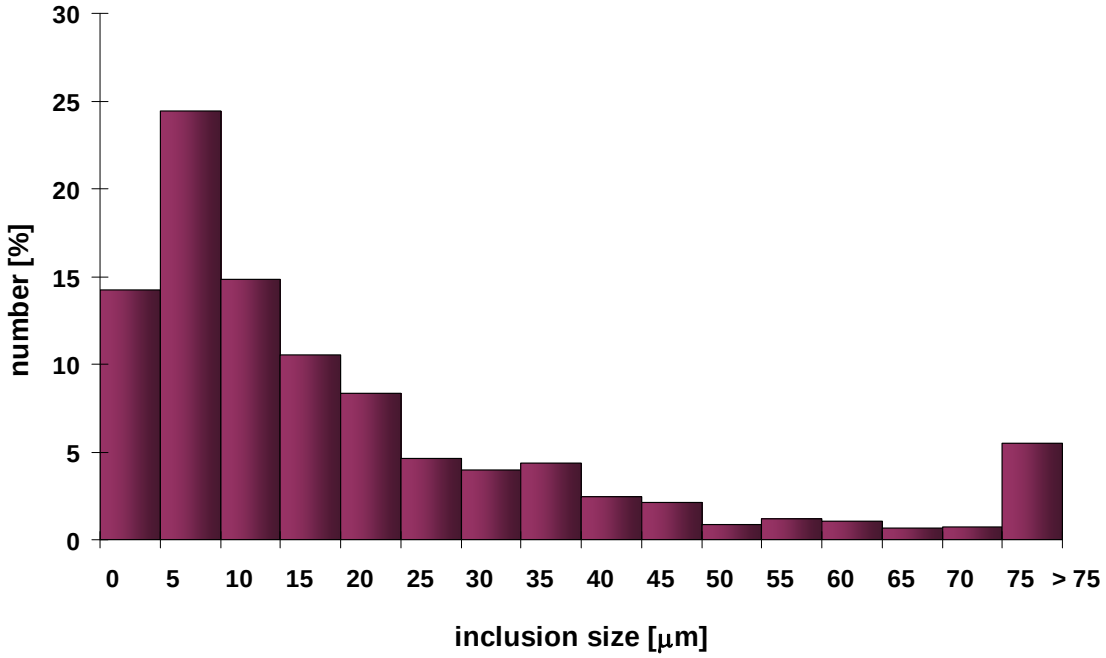

Figure 3.29: Inclusion size number distribution analyzed by light microscope.

Figure 3.30 presents the mass % of the inclusions versus their equivalent diameter. Notice that the y-axis is in logarithmic scale. The density of the SiC particles (ρ_{SiC}) is 3.16 g/cm^3 and the density of Si_3N_4 ($\rho_{Si_3N_4}$) is 3.17 g/cm^3. Assuming that half of our particles are carbides and the other half are nitrides, the density of the inclusions is taken 3.165 g/cm^3. Using the simple formulas in equations (3.5) and (3.6), we can calculate the inclusion mass. Table 3.4 shows the statistical data for this analysis.

Table 3.4. Analysis data of the inclusion size distribution in silicon scrap samples analyzed by light microscope.

Total No.	Min size [μm]	Max size [μm]	Mean [μm]	Median [μm]	STD
1331	0.8	295.3	25.4	13.0	36.0

From Figure 3.30, we can see that, even though the majority of the particles are small, the contribution of the large inclusions to the mass balance is much greater. More than 90 % of the total mass has a size > 75 μm. This clearly indicates the importance of large inclusions in the mass distribution.

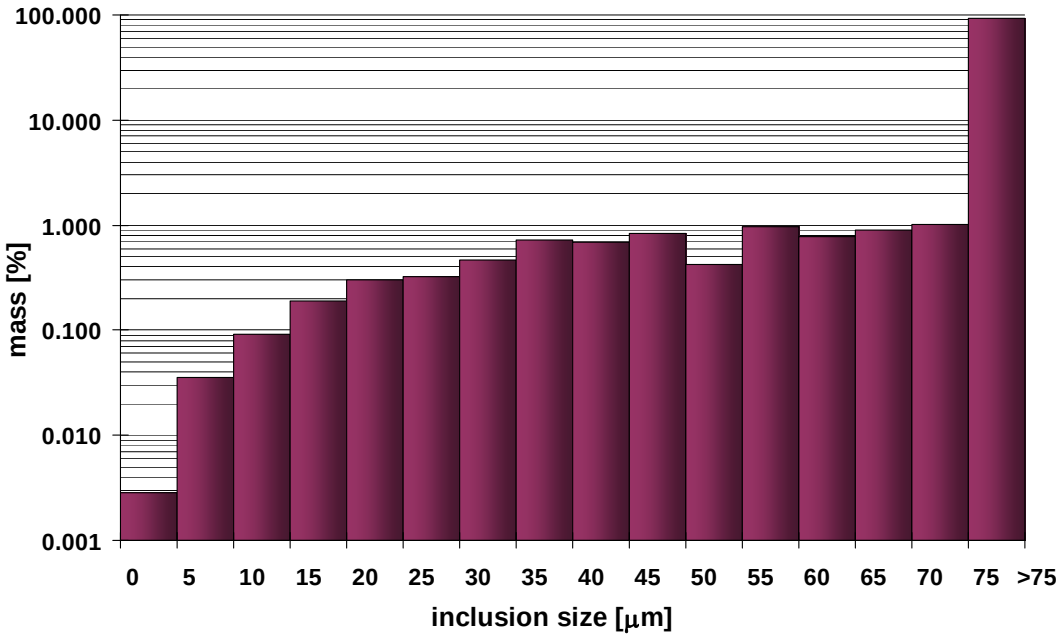

Figure 3.30: Mass % distribution of inclusions present in the silicon scrap by light microscope.

The results from the two different techniques employed to analyze the particle distributions generally agree. The curves of the particle size distributions given in Figure 3.28 and 3.29 have the same shape. They both show that the maximum of the number of particles lies in a size 5 to 10 μm. However, the first analysis (Table 3.3) shows that about 33% of the particles lie in this range while the other technique shows 25%. This variation may be explained by the difference in the sampling and analyzing techniques employed in each case.

3.3.2.3 Chemical analysis of the silicon scrap

Samples from the top-cut silicon scrap were analyzed by GDMS for the level of impurities present in the scrap. The results of the chemical analysis are shown in Table 3.5.

Table 3.5: Concentration of the main impurities present in top-cut silicon scrap analyzed by GDMS.

Element	P	Ca	Ti	Fe	Zr	Mg	Al
Concentration [mass ppm]	0.09	0.84	0.02	0.28	-	0.01	1.24

The results from the LECO analyzer for carbon and nitrogen concentrations in top-cut silicon scrap are shown in Table 3.6. Three different runs were carried out and the average values are calculated.

Table 3.6: Concentration of carbon and nitrogen present in top-cut silicon scrap analyzed by LECO.

C-content / [mass ppm]	Mean C-content (STDV) / [mass ppm]	N-content / [mass ppm]	Mean N-content STDV / [mass ppm]
138 / 96 / 70	101.3 (34.3)	43 / 37 / 59	46.3 (11.4)

3.3.3 SiC and carbon filters

Filtration experiments were carried out using ceramic foam filters. They were provided by Eger-Sørensen AS, a Norwegian company and Foseco AB, a British company. These filters are used in filtration of molten aluminum and molten iron and are commercially available in the market. They consist of silicon carbide (SiC), carbon and binders. The brand, material, pore size and maximum service temperature are shown in Table 3.7.

Table 3.7: The brand, material, pore size and maximum service temperature of the filters.

Brand	Material	Pores per inch [ppi]	Capacity [kg/cm^2]	Max. temp. [◦C]	Producer
STELEX Pro	Graphite (65%)	10	1.95 - 2.90	1680	Foseco AB
SEDEX	SiC (65%)	10, 20, 30	4.0	1500	Foseco AB
Nil	SiC (85%)	10, 20, 30	-	1500	Egør-Sørensen AS

Figure 3.31 shows photos of SiC and carbon filters. SiC filters with 10, 20 and 30 pores per linear inch (ppi), and carbon filters with 10 ppi were used in our experiments.

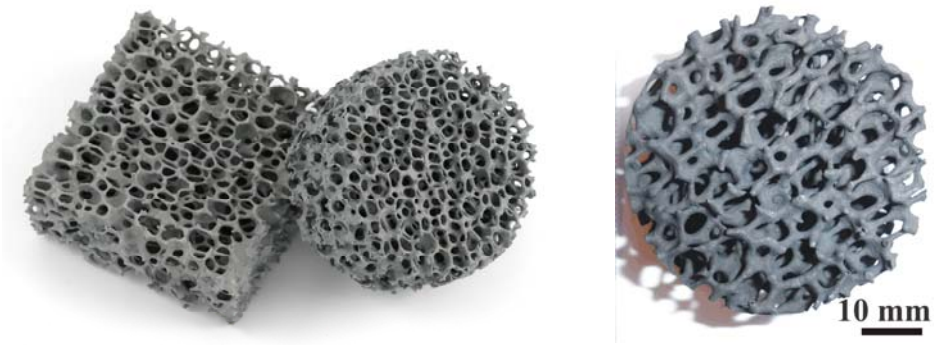

SiC filters (10 and 20 ppi) Carbon filter (10 ppi)

Figure 3.31: The SiC and carbon filters used in filtration of silicon scrap.

The ceramic foam filters are made by impregnating organic foam, usually polyurethane foam, with an aqueous slurry containing the main material (silicon carbide for SiC filter, and graphite for carbon filters) and the corresponding binder. Then, removing the excess slurry (for example by squeezing the impregnated organic foam), drying and firing the impregnated organic foam, and cutting or machining the resulting piece to pieces of the required shape and size takes place afterwards.

The silicon carbide filters consists of 20 - 85% silicon carbide, 20 - 50% alumina, 1.5 - 5.0% silica derived from colloidal silica sol and 1 - 3% alumino-silicate fibers by mass.

The carbon filters have 20 – 80% graphite, 1 – 10% wollastonite, 1 – 20% silica, and 1 – 10% an alkali phosphate glass by mass.

The exact composition of the filters used in our experiments was not provided from the producers. However, the SiC filters from Foseco AB contain 65% by mass SiC while the filters provided from Eger-Sørensen AS have 85% by mass SiC. Light microscopic pictures shown in Figure 3.32 display the inner structure of SiC filters. The SiC particles that compose the filters appear in white color. From these pictures it is seen that the filters from Foseco AB have a low quantity of SiC and consist mainly of

binder even though the claim is 65% in mass of SiC. For this reason, in our experiments filters with 65% SiC were used only in introductory experiments. All the results concerning filtration reported in this thesis are for only 85% SiC filters and carbon filters.

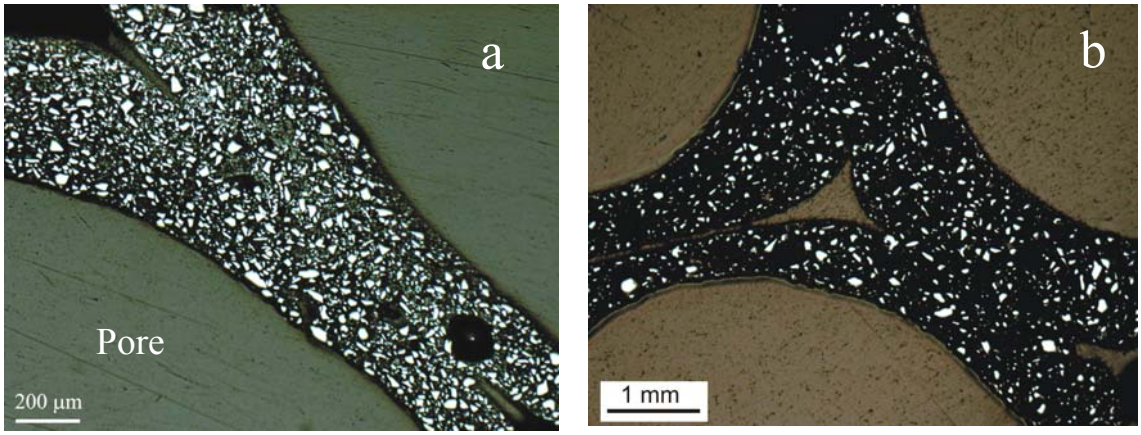

Figure 3.32: a) Ceramic foam filter with 85% SiC (Eger-Sørensen AS), b) Ceramic foam filter with 65% SiC (Foseco AB). SiC particles appear white in the pictures.

A picture taken with light microscope of the carbon filter is shown in Figure 3.33. The filters samples that were submitted to light microscopy were first molded into resin and than polished with fine SiC paper.

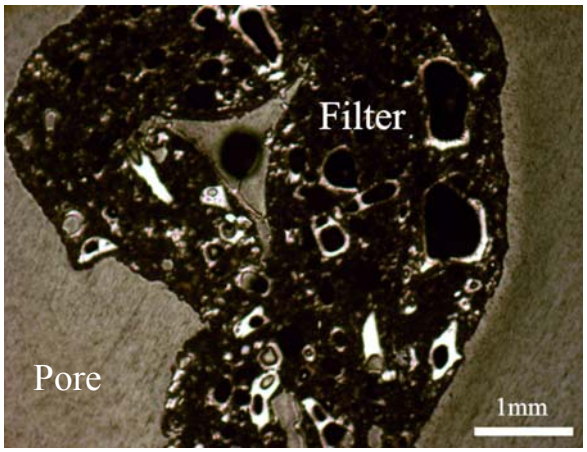

Figure 3.33: A picture of carbon filter wall taken by a light microscope showing the inner structure of the filter.

Mapping of a SiC filter (85% - SiC) and a carbon filter is carried out by EPMA for C, Si, Al, and O. Figures 3.34 and 3.35 show the results from the analysis.

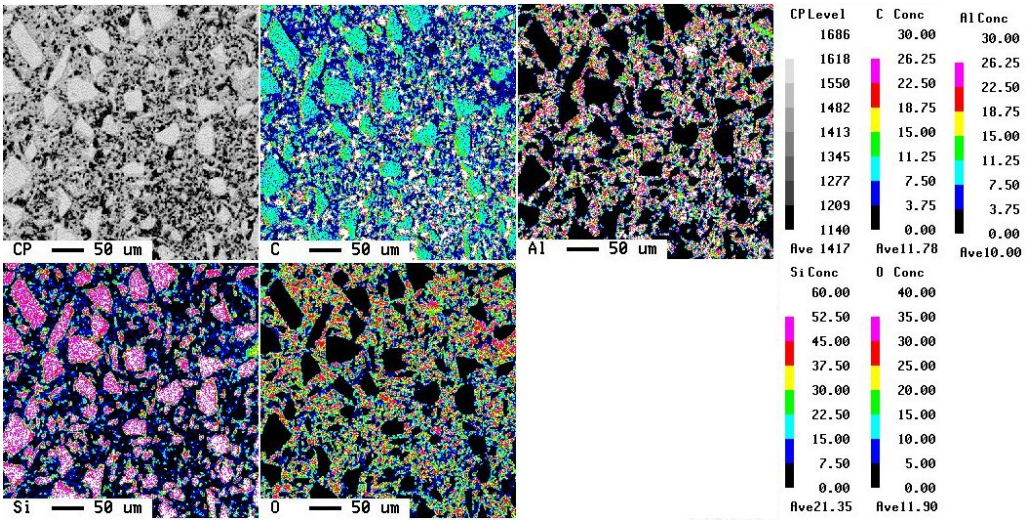

Figure 3.34: Mapping of a SiC (85%) filter wall by EPMA.

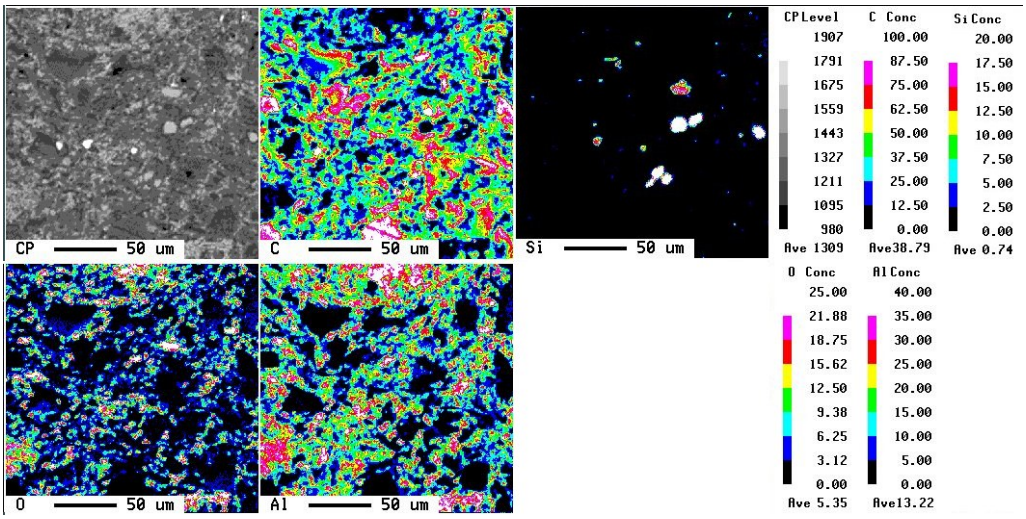

Figure 3.35: Mapping of a carbon filter wall by EPMA.

As Figure 3.34 shows, the SiC particles that compose the filter are surrounded by the binder material which consists, as mentioned before, mainly of alumina. The only purpose of the binder is to serve as glue for the SiC particles. Sintering of SiC particles does not take place. The situation is almost the same with the carbon filters but in this case the graphite material is mixed better with the binder so that it almost seems to be one material. X-ray diffraction analysis carried out for both SiC and carbon filters

confirms the presence of alumina (Al_2O_3) and silica (SiO_2) in SiC filters and of alumina in carbon filters.

3.3.4 Refractory materials – raw materials used in wetting experiments

3.3.4.1 Filter material

A carbon and a silicon carbide (85% SiC) filter were taken and ground to fine powder using a ball-mill and sieved afterwards with a 41 μm mesh. The powder collected was pressed in shape of a disc with diameter 10 mm and depth 3 mm. These discs were used as substrates in the wetting experiments with pure silicon.

3.3.4.2 Graphite substrates

Various purified graphite materials were used as substrates in the study of the wettability of molten silicon with refractories. They were provided by Svenska Tanso AB, the Swedish branch of Toyo Tanso Company that produces graphites for metallurgical applications. For the sessile drop experiment a substrate with a flat surface is needed to be in contact with molten silicon. The graphite materials received were in the form of blocks. The graphite materials were cut into slices with 3 mm thickness using a diamond saw with 2 mm thickness at a speed of 10 mm/sec. Then, graphite discs with a diameter of 10 mm were cut by a core drill from the slices. Afterwards, different surface roughnesses for the substrates were made by polishing the surface with silicon carbide emery papers 1200, 2400 and 4000. Table 3.8 shows the properties of the graphite substrates used in our study.

Table 3.8: The measured properties of the graphite substrates.

Substrate	Average pore diameter [μm]	Porosity [%]	Bulk denstity [g cm^{-3}]
IG11*	2.5	18.3	1.742
ISEM3*	2.72	13.4	1.858
ISO88*	0.66	12.1	1.885
SIC6	3.2	12.7	1.849
IG610	2.6	12.8	1.814

*Safarian-Dastjerdi [2007].

3.3.5 Pure silicon for wetting experiments

SoG poly-crystalline silicon with impurity level of ~ 1ppm was used as the sample in the sessile drop experiments. It was provided by REC-Silicon, which is one of the main producers of SoG-Si. The silicon samples were prepared as small cubic pieces with dimensions of 3 × 3 × 3 mm. Before experiments, they were etched for 1 min. in acid mixture as described in Section 3.2.2 to remove impurities from the sample surface.

3.4 Experiments

3.4.1 Overview of filtration experiments

An overview on the filtration experiments and other details is given in Table 3.9 and 3.10. The SiC filters used are of 85% SiC material. In experiment number 17 (Table 3.10) the silicon material employed for filtration is pure poly-crystalline silicon produced by the Siemens process and provided by REC. Table 3.9 also gives an overview of the previous experiments with 30 ppi SiC filters conducted by Chithambaranadhan [2005] during his Master thesis, and Table 3.10 gives an overview of the new experiments carried here.

Table 3.9: Data on filtration experiments carried out by Chitambaranadhan [2005].

Exp. No.	Filter	Pore size	Filter depth [mm]	Input Si [g]	Output Si [g]
NF1	SiC – Eger Sørensen	30 ppi	26	180.6	166.6
NF2	- " -	- " -	- " -	157.5	128.0
NF3	- " -	- " -	- " -	182.5	158.2
NF4	- " -	- " -	- " -	189.8	158.4
NF5	- " -	- " -	- " -	179.4	166.0
NF6	- " -	- " -	- " -	183.6	166.0
NF7	- " -	- " -	- " -	175.4	149.0
NF8	- " -	- " -	- " -	161.5	152.0
NF9	- " -	- " -	- " -	173.6	159.8

Table 3.10: Data on new filtration experiments.

Exp. No.	Filter	Pore size	Filter depth [mm]	Input Si [g]	Output Si [g]
1	C - Foseco	10 ppi	38	311	193
2	- " -	- " -	- " -	301	46.6
3	- " -	- " -	- " -	271	151.5
4	- " -	- " -	- " -	248.7	158
5	SiC – Eger Sørensen	- " -	26	291	104.6
6	- " -	- " -	- " -	258	231.2
7	- " -	- " -	- " -	252.1	122.5
8	- " -	- " -	- " -	294	248
9	- " -	20 ppi	- " -	300.8	252
10	- " -	- " -	- " -	300.7	227.8
11	- " -	- " -	- " -	268	170
12	- " -	- " -	- " -	280	231
13	- " -	30 ppi	- " -	258	234
14	- " -	- " -	- " -	285	244
15	- " -	- " -	- " -	285.5	250.8
16	- " -	- " -	- " -	260	232
17	- " -	- " -	- " -	324.3	250

3.4.2 Overview of wetting experiments

Several substrates with different surface roughness were prepared from the refractory materials. Table 3.11 summarizes the wetting experiments. Apart from the experimental details it also gives the main results, which are the final contact angles and the maximum infiltration depth of molten silicon in the substrates. Two experiments were carried out with substrates from the filter materials, one with the carbon filter and the other one with the SiC filter (85% SiC). Also 28 experiments with five different graphite materials were performed. The silicon samples were pure poly-crystalline silicon prepared by the Siemens process. Argon gas was flushed during the experiments at a flow rate of about 500 ml/min, while the pressure in the furnace ranged from 80 – 100 mbar. The temperature was kept constant at 1450°C and the oxygen level was 5×10^{-16} - 5×10^{-18} ppm.

Table 3.11: Overview of the wetting experiments of molten silicon with various refractories (see Table 3.8). The results on final contact angles and maximum infiltration depth are also shown.

Exp. No.	Substrate	Sample	Roughness R_a [mm]	Final contact angle [°]	Max infiltration depth [μm]
1	C filter (powder)	Si pure	-	0	-
2	SiC filter (powder)	- « -	-	18.7	-
A1	IG11	- « -	1.27	0	814
A2	- « -	- « -	1.27	-	701
A8	- « -	- « -	0.79	0	872
A24	- « -	- « -	0.14	25.1	614
A40	- « -	- « -	0.09	28	698
D1	ISEM3	- « -	1.32	0	1272
D2	- « -	- « -	1.32	0	1355
D8	- « -	- « -	0.56	0	1524
D24	- « -	- « -	0.11	23.8	872
D40	- « -	- « -	0.09	27.2	906
F1	ISO88	- « -	0.93	7.0	323
F4	- « -	- « -	0.12	28.9	135
F5	- « -	- « -	0.06	28.0	150
F8	- « -	- « -	0.92	8.4	313
F10	- « -	- « -	0.71	12.0	614
F12	- « -	- « -	0.45	17.2	596
F40	- « -	- « -	0.06	31.1	159
S1	SIC6	- « -	0.13	21.4	1060
S8	- « -	- « -	1.00	0	2857
S10	- « -	- « -	0.81	0	3120
S12-1	- « -	- « -	0.69	0	1568
S12-2	- « -	- « -	0.65	0	>1600
S24	- « -	- « -	0.18	14.4	1149
S40	- « -	- « -	0.10	27.1	1161
Z1	IG610	- « -	1.54	2.1	1360
Z8	- « -	- « -	0.46	5.0	1178
Z12	- « -	- « -	0.25	7.7	1591
Z40	- « -	- « -	0.10	27.4	785

Chapter 4

EXPERIMENTAL RESULTS

Experimental results are given in this chapter. Settling of SiC particles in molten silicon is presented first followed by filtration of inclusions from the silicon scrap and then, wetting of molten silicon on the graphite substrates.

Light microscopy is employed to analyze the inclusions in silicon samples before and after settling and filtration. The data achieved is used to quantify the removal efficiency after each method. SEM and other analyzing techniques such as EPMA, Leco etc. are also employed to analyze the silicon samples.

At the wetting experiments, focus is placed on the final contact angles and the infiltration depth of the molten silicon in the graphite materials.

4.1 Settling of SiC particles in molten silicon

Settling experiments were performed in the Heliosi furnace. The material, Solsilc silicon was supplied by SINTEF Materials and Chemistry. The experimental procedure is described in Section 3.1.1.2. Ingots after solidification were named FS-4A and FS-4B. They were round with a height of about 100 mm and diameter of 250 mm.

4.1.1 Sampling and analyzing techniques

After solidification, the silicon cast ingots were cut in half. Samples were taken close to the center of the ingot from the top to the bottom as shown in Figure 4.1. To analyze quantitatively the inclusion content from the bottom to the top, the ingot was divided into 7 regions as indicated in Figure 4.1. A thin slice with a thickness of 2 mm was cut at the bottom of the ingot.

4.1.2 Inclusions in the bottom of the ingot

Samples from the Solsilc silicon before and after settling experiments were analyzed with light microscope, SEM, and EPMA. As mentioned before, a thin slice with thickness of 2 mm was cut in the bottom of the ingots. Figure 4.2 shows two pictures taken with a light microscope of the inclusions found in this layer. In this sample, the concentration of inclusions is very high and they appear in large clusters as Figure 4.2 shows.

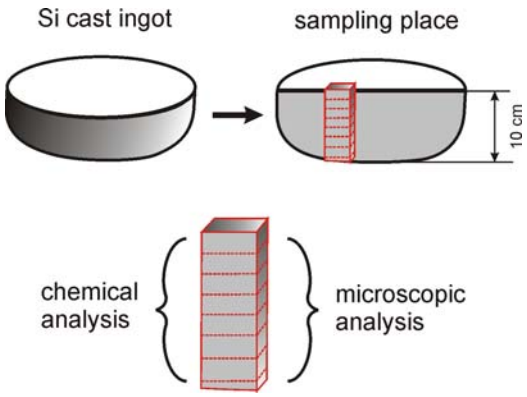

Figure 4.1: Sampling of the cast silicon ingot.

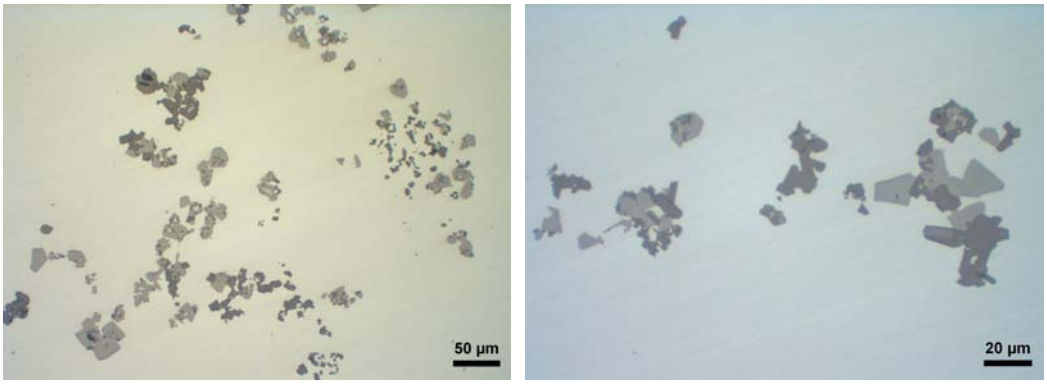

Figure 4.2: Inclusions in the bottom of the ingot.

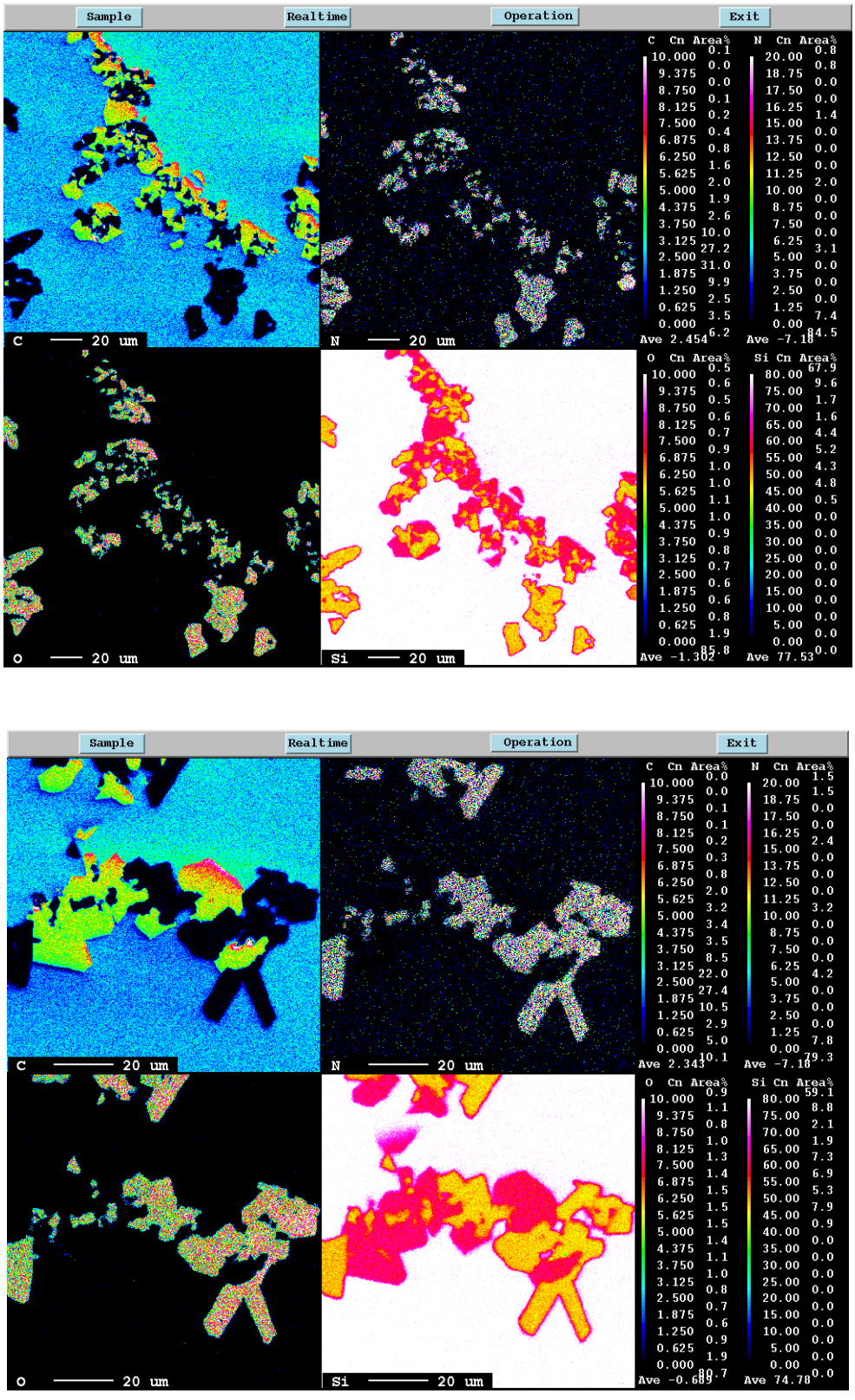

Figure 4.3: EMPA analysis of two different inclusions clusters inside the 2 mm layer at the bottom of the ingot showing the presence of SiC and SiO_xN_y particles.

As mentioned in Section 3.1.1.1, the bottom of the ingot is in direct contact with the silicon nitride coating which prevents sticking of the silicon to the quartz crucible. This layer may be a source for inclusions in the bottom of the ingot. Therefore, mapping of several areas of the 2 mm-thick layer by EMPA was performed in order to determine the chemical composition of the inclusions. Figure 4.3 shows the content of C, N, O and Si in the inclusion clusters. As it can be seen from Figure 4.3, EMPA analysis confirms the presence of SiC particles and silicon oxy-nitrides (SiO_xN_y). SiC particles make about half of the inclusions clusters. While the source of SiO_xN_y particles is the anti-sticking silicon nitride layer, the SiC particles are inclusions that have settled during the experiment.

1 cm^2 of the 2 mm layer at the bottom of ingot FS-4B is analyzed by light microscopy. All the particles found inside this area were counted and their surface area was measured. However, particle size analysis performed with light microscopes, as described in Section 3.2.3, does not distinguish between the SiC and Si_3N_4 particles (or SiO_xN_y). Therefore, in the calculations of the number and mass distribution, only half of the particles were considered. This approximation was based on EPMA analysis (see Figure 4.3). The data are summarized in Table 4.2.

4.1.3 Inclusions along the ingot

Analysis of the inclusion number and mass distribution along the whole height of the ingot is carried out by means of light microscopy. The sample was divided into 7 regions starting from bottom to the top of the ingot as indicated in Figure 4.1. First, a surface area of 1 cm^2 is observed in each region. Then, the samples were ground to a depth of 0.5 cm in the horizontal direction, and a surface area of 1 cm^2 was analyzed again in each region. This procedure was repeated twice thus, allowing us to obtain information from three different areas in each region. Inclusions found inside these areas are analyzed according to the procedure described in section 3.2.3.2. The averaged data for two cast ingots, named FS-4A and FS-4B, are shown in Figure 4.4 and 4.5. Table 4.1 and 4.2 give the data before and after settling, respectively for the two casts. In Table 4.2, data for the bottom 2 mm-thick layer are also given.

From Figures 4.4 and 4.5 it is seen that the concentration of inclusions in Solsilc silicon before settling is very high compared to after the settling experiments. The mass of inclusions in the 2 mm-thick layer in the bottom of the ingot is more than 10 times higher than in the rest of the ingot (see Figure 4.5).

The mass of inclusions is calculated from equation (4.1).

$$m_p = \frac{\pi}{6} \cdot d_p^3 \cdot \rho_{SiC} \tag{4.1}$$

where m_p is the mass of the particle, ρ_{SiC} is the density of the SiC particles (3.16 g/cm^3).

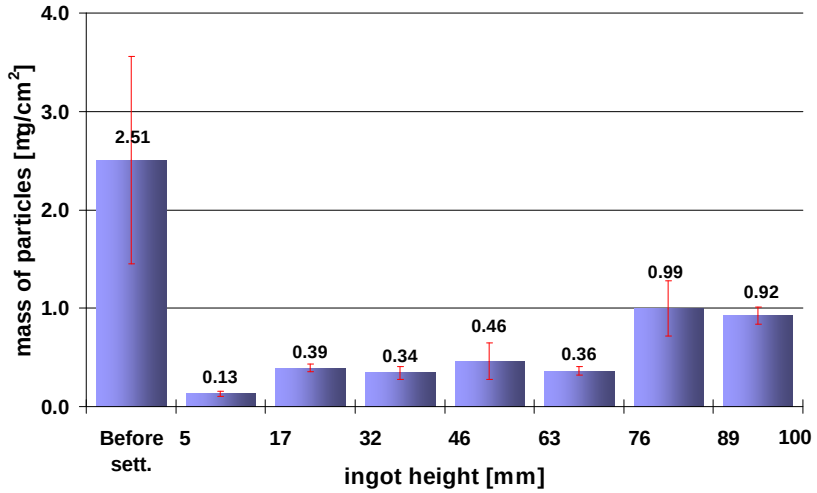

Figure 4.4: Inclusion mass along the ingot FS-4A (see Table 4.1).

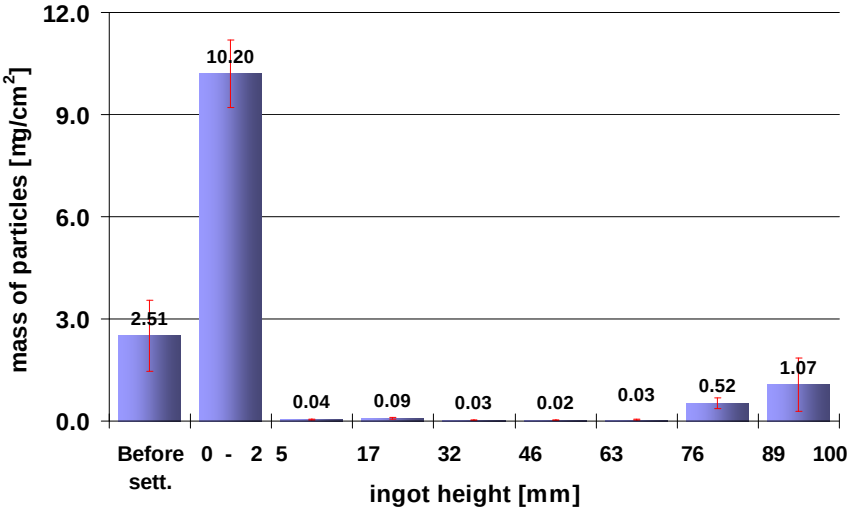

Figure 4.5: Inclusion mass along the ingot FS-4B (see Table 4.2).

Table 4.1: Analysis of ingot FS-4A.

1 cm^2 [mm]	**Number of inclusions/cm^2**	**Surface area, S_i [mm^2/cm^2]**	**Mass [μg/cm^2]**	**Removal efficiency, η_{sett}**
Before sett.	375	35149.9	2.51	-
89 - 100	51	8488.9	0.92	75.8%
76 - 89	87	10758.3	0.99	69.4%
63 – 76	60	5227.4	0.36	85.1%
46 - 63	90	6937.8	0.46	80.3%
32 - 46	370	7451.5	0.34	78.8%
17 - 32	886	8440.2	0.39	76.0%
5 - 17	26	2390.4	0.13	93.2%

Table 4.2: Analysis of ingot FS-4B

1 cm^2 [mm]	**Number of inclusions/cm^2**	**Surface area, S_i [mm^2/cm^2]**	**Mass [μg/cm^2]**	**Removal efficiency, η_{sett}**
Before sett.	376	35149.9	2.51	-
89 - 100	46	7248.3	1.07	79.4%
76 - 89	111	7033.8	0.52	80.0%
63 – 76	10	733.7	0.03	97.9%
46 - 63	8	494.9	0.02	98.6%
32 – 46	6	555.9	0.03	98.4%
17 – 32	12	1302.9	0.09	96.3%
5 – 17	6	721.2	0.04	97.9%
2 mm	798	3224225	10.20	-

In the middle of the ingot the content of inclusions is very much lower than in the top. In Table 4.1 and 4.2 removal efficiency is calculated from the measured surface area of the particles per cm^2 before and after settling using equation (4.2).

$$\eta_{sett.} = \frac{S_{i\ \text{before sett.}}^{m} - S_{i\ \text{after sett.}}^{m}}{S_{i\ \text{before sett.}}^{m}} \times 100\% \qquad (4.2)$$

Excluding the bottom 2 mm, on average, the removal efficiency is about 80 % in the ingot FS-4A and about 93 % in ingot FS-4B.

Total carbon content of the samples along the ingot height is analyzed with a LECO analyzer. The results are shown in Figure 4.6 and 4.7 for the cast FS-4A and FS-4B respectively. The carbon concentration is given in mass ppm.

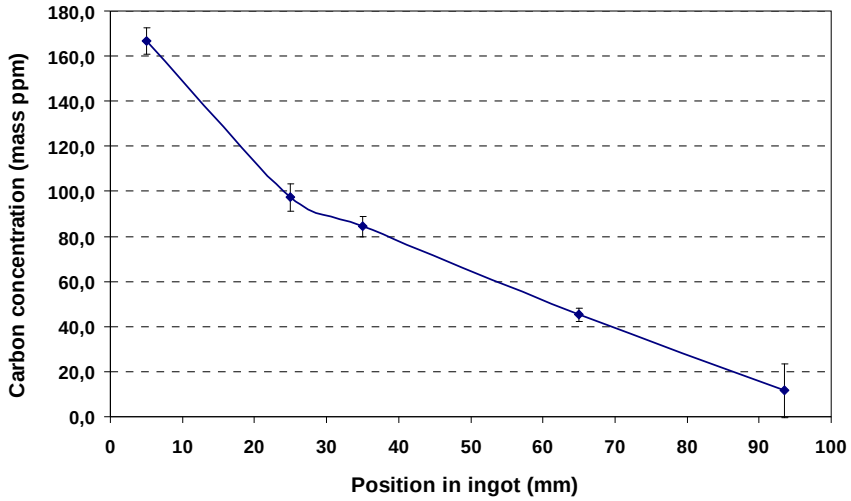

Figure 4.6: Carbon content in mass ppm along the FS-4A cast silicon ingot.

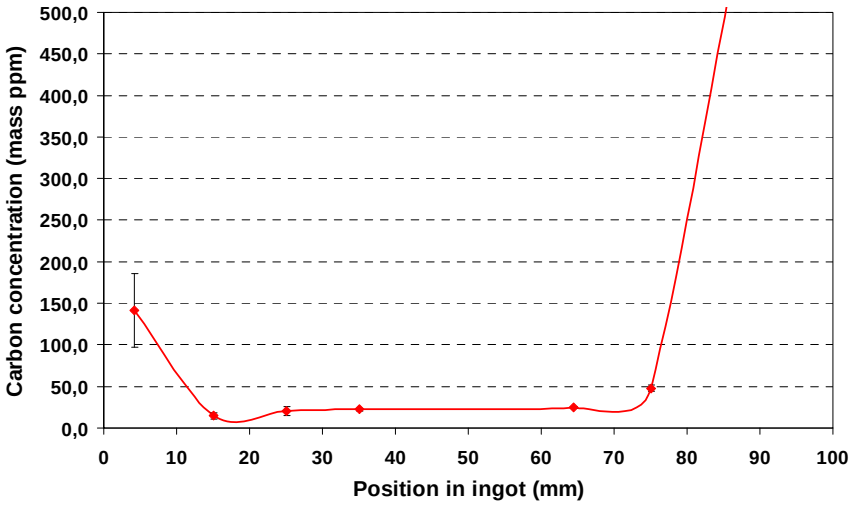

Figure 4.7: Carbon content in mass ppm along the FS-4B cast silicon ingot.

The results for cast FS-4A show that concentration of total carbon drops with the height of the ingot. In cast FS-4B the concentration of total carbon in the middle of the

ingot is lower than in the bottom and in the top. It is about 25 ppm by mass at locations 15 - 70 mm from the bottom of the ingot. Knowing that the material contained initially about 700 mass ppm carbon, it shows a removal efficiency of 96.4% on average.

4.2 filtration of top-cut silicon scrap with ceramic foam filters

4.2.1 Inclusions in silicon after filtration

In the previous chapter, the content of solid inclusions in the top-cut silicon scrap are determined both qualitatively and quantitatively by employing light and electronic microscopy. The same techniques are employed here to give the content of inclusions in the silicon after filtration. Samples from filtered silicon after each experiment were taken randomly for light and electronic microscopy analysis.

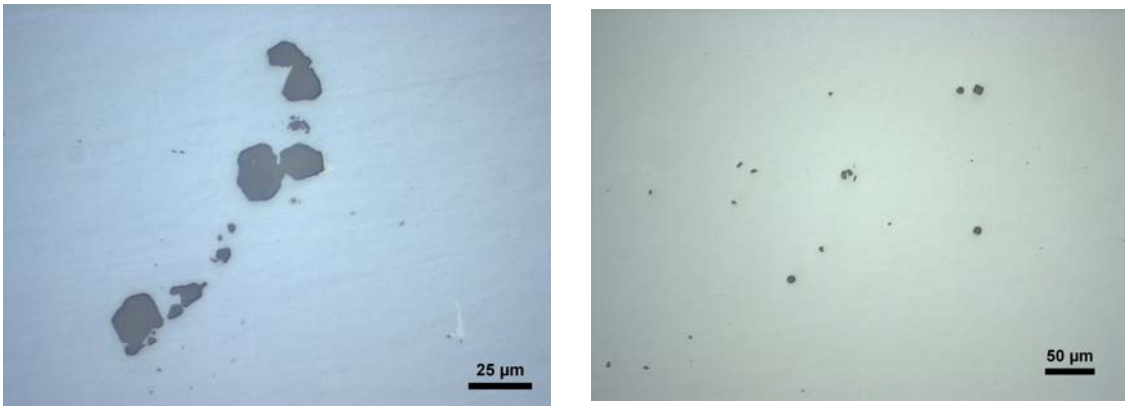

Figure 4.8: Large inclusions in filtered silicon with 10 ppi C filter (left side) from Exp.2 and with 30 ppi SiC filter (right side) from Exp.13.

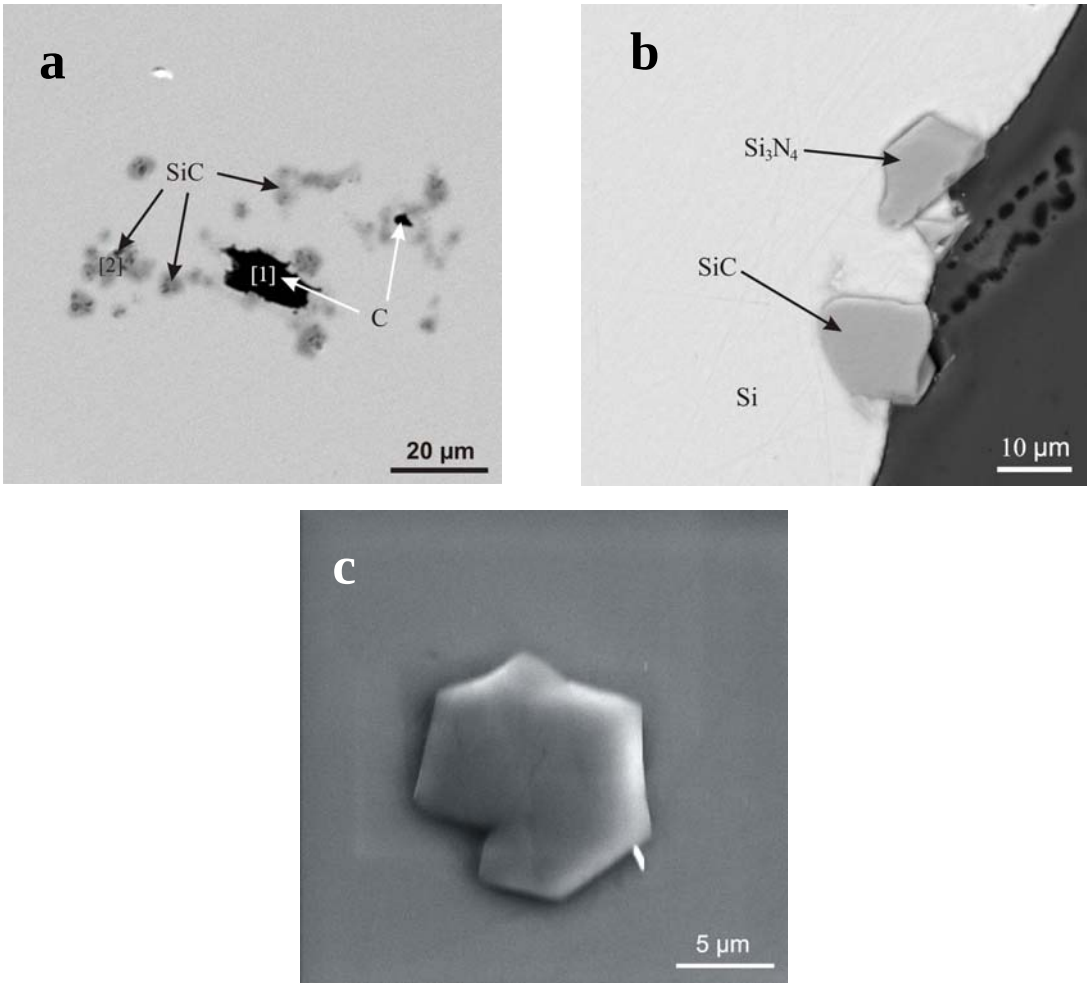

Figure 4.9: EPMA pictures from filtered silicon with a) 10 ppi carbon filter (Exp.3), b) 20 ppi SiC filter (Exp.12) and, c) 30 ppi SiC filter (Exp.13) where carbon, SiC and Si_3N_4 particles are found.

Figure 4.8 shows two pictures taken with light microscope of some of the largest inclusions found in filtered silicon with a carbon filter 10 ppi from Exp.2 and with a SiC filter 30 ppi from Exp.13 and Figure 4.9 shows EPMA pictures of some inclusions in filtered silicon (Exp.3, 12 and 13). Particles found in filtered silicon with 10 and 20 ppi were SiC and Si_3N_4 inclusions, while in silicon filtered with 30 ppi SiC filters only SiC was found. Pure carbon inclusions were found in filtered silicon (Figure 4.9-a), indicating that molten silicon might have carried off graphite particles from the crucible during filtration.

4.2.1.1 Inclusion count after dissolution of silicon matrix

Several samples from silicon before and after filtration with 10, 20 and 30 ppi SiC filters were dissolved in the acid mixture of HF and HNO_3 as described in section 3.2.2. Inclusions extracted were carefully collected and counted by light automated microscope (see section 3.2.3.1). The results from dissolution of silicon scrap before filtration are shown in Table 4.3 and those for dissolution of silicon after filtration are shown in Table 4.4. Since in 174 g of silicon scrap before filtration there are 23734 particles, this gives about 13855 particles per 100 g silicon scrap.

Table 4.3: Count of inclusions in silicon before filtration.

Mass dissolved [g]	Number of inclusions
14.2	5041
12.7	5842
12.8	1992
13.6	1000
7.5	No inclusions
11.2	7
9.4	517
7.5	No inclusions
10.0	No inclusions
9.4	No inclusions
9.2	5
6.9	5
10.2	1
7.8	No inclusions
10.8	No inclusions
9.1	3417
9.0	5907
Total 171.3	23734

In Table 4.4 the number of particles is for dissolution of 100 g of silicon scrap in each filtration experiment with various SiC filters. Dissolution of silicon after filtration with 30ppi SiC filters was carried out by Chithambaranadhan [2005] in preliminary experiments. Dissolution of 300 g silicon after filtration with 30 ppi SiC filters from experiments 14, 15 and 16 of this study was also carried out. However, no inclusions were found after these experiments. Table 4.5 summarizes the results from Table 4.6. Standard deviation data are placed in brackets.

Table 4.4: Count of inclusions in 100 g silicon after filtration. The experiment from which the silicon is taken is shown in brackets.

10 ppi SiC	20 ppi SiC	30 ppi SiC*
2470 (Exp.5)	1089 (Exp.9)	48 (NF1)
2608 (Exp.6)	1857 (Exp.9)	21 (NF2)
2315 (Exp.6)	738 (Exp.10)	6 (NF3)
4118 (Exp.7)	470 (Exp.11)	72 (NF4)
1803 (Exp.8)	1649 (Exp.12)	14 (NF5)

*Dissolution of Si after filtration with 30 ppi SiC filters were carried out by Chithambaranadhan [2005]. The data are corrected for dissolution of 100 g. The experiment code is shown in brackets.

Table 4.5: Results from dissolution of silicon scrap before and after filtration.

	Si before fil.	10 ppi filter	20 ppi filter	30 ppi filter
No. of particles (STDV) /100 g	13855	2663 (869)	1159 (585)	32 (27)
Filtration efficiency η_{filter}^{count} [%]	-	80.8	91.6	99.8

Filtration efficiency based on inclusion count, η_{filter}^{count}, is calculated from equation (4.3).

$$\eta_{filter}^{count} = \frac{N_{\text{before fil.}} - N_{\text{after fil.}}}{N_{\text{before fil.}}} \times 100\% \qquad (4.3)$$

As one can expect, filters with smaller pores have higher removal efficiencies. 30 ppi SiC filters remove more than 99% of inclusions from silicon. The graph in Figure 4.10 gives the number of particles given in Table 4.5.

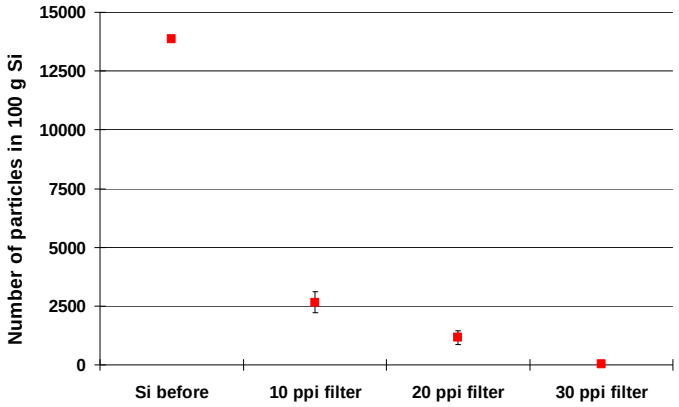

Figure 4.10: Total number of particles in 100 g silicon before and after filtration given in Table 4.5.

4.2.1.2 Inclusion count by light microscopy

A surface area of 1 cm^2 from silicon samples after filtration with 10, 20 and 30 ppi SiC filters from Exp.6, 9 and 14 is analyzed by light microscopy according to the method described in section 3.2.3.2. All inclusions found in this area are measured and their equivalent diameter is calculated. Particle size distribution of inclusions in silicon after filtration is shown in Figures 4.11 – 4.13, for 10, 20 ands 30 ppi SiC filters respectively.

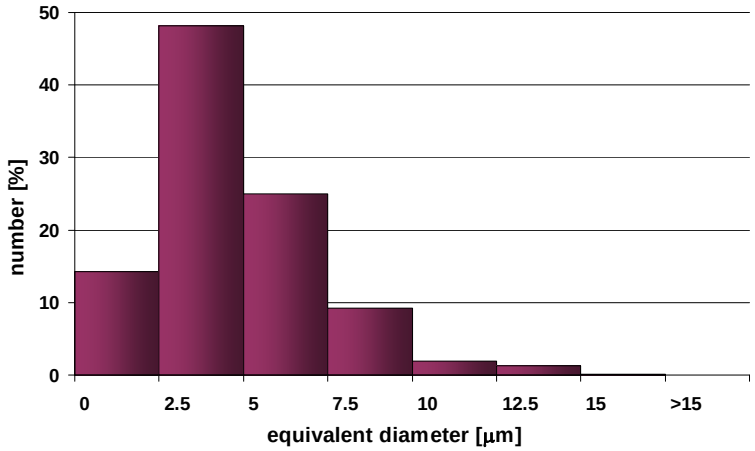

Figure 4.11: Size distribution by number% of inclusions after filtration of silicon scrap with 10 ppi SiC filter (Exp.6).

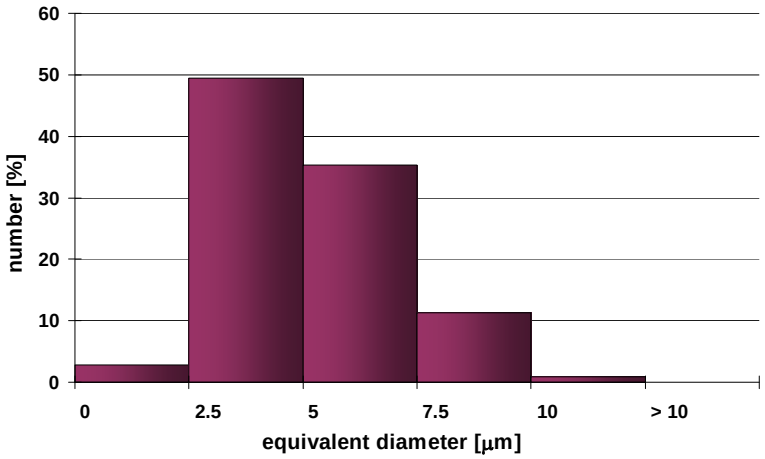

Figure 4.12: Size distribution by number% of inclusions after filtration of silicon scrap with 20 ppi SiC filters (Exp.9).

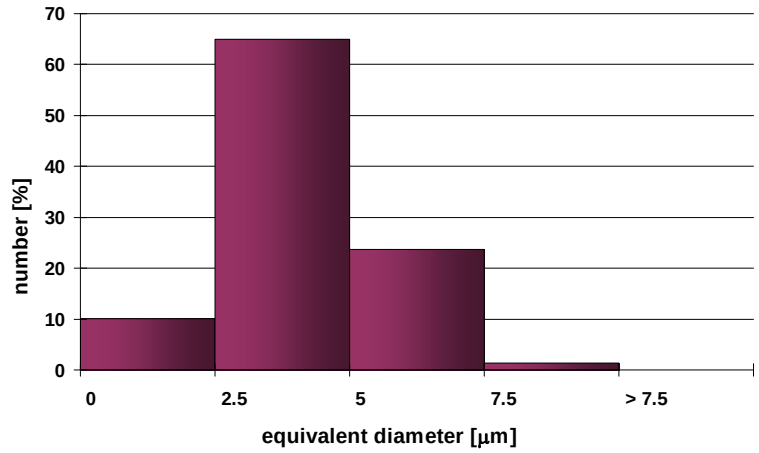

Figure 4.13: Size distribution by number% of inclusions after filtration of silicon scrap with 30 ppi SiC filters (Exp.14).

Figures 4.11 – 4.13 show how the size distribution of inclusions in filtered silicon changes on changing the pore size of the filter. Almost all particles larger than 7.5 μm are removed from silicon scrap when using a 30 ppi filter. It is important to note that after filtration with a 30 ppi filter, all particles in silicon are SiC round in shape, and no inclusion cluster is found.

However, there is a discrepancy between the size distributions of inclusions after filtration with 10, 20 and 30 ppi filters. For example, about 14% of the particles

measured after filtration with 10 ppi filter have a size from 0 – 2.5 μm, and only 3% and 10% of the particles after filtration with 20 and 30 ppi filters fall within this size. This could be explained with the presence of secondary inclusions in the silicon samples and it is discussed in the next chapter.

The mass of inclusions m_p is calculated from their equivalent diameter from equation (4.1) for SiC particles with density ρ_{SiC} = 3.16 g/cm^3. The data obtained from the analysis is summarized in Table 4.6.

Table 4.6: Results from light microscopy analysis of silicon scrap before and after filtration.

	Si scrap before	**10 ppi (Exp.6)**	**20 ppi (Exp.9)**	**30 ppi (Exp.14)**
Number of inclusions/cm^2	144	637	212	228
S_i^m **[μm^2/cm^2]**	226951	9422	3301	2228
Mass [μg/cm^2]	157.6	0.22	0.067	0.038
d_p **range [μm]**	0 – 360	0 – 15	0 – 10	0 – 7.5
Average d_p [μm]	29	4.7	5.1	4.1
Filt. eff. $\eta_{filter}^{surface}$ [%]	-	95.8	98.6	99.0

Filtration efficiency based on surface area of inclusions observed before and after filtration, $\eta_{filter}^{surface}$, is calculated from equation (4.4).

$$\eta_{filter}^{surface} = \frac{S_{i\ \text{before fil.}}^{m} - S_{i\ \text{after fil.}}^{m}}{S_{i\ \text{before fil.}}^{m}} \times 100\% \qquad (4.4)$$

The graph in Figure 4.14 shows the total surface area and total mass of inclusions in silicon before and after filtration. The axis for mass values, placed on the right of the graph with blue color, is in logarithmic scale. Filtration efficiency for all filters gives high values. 1 cm^2 surface area of Si samples was observed. In microscopic image analysis where the surface area and the mass of particles are measured and calculated, missing one 10 μm particle corresponds to missing one thousand particles of 1μm.

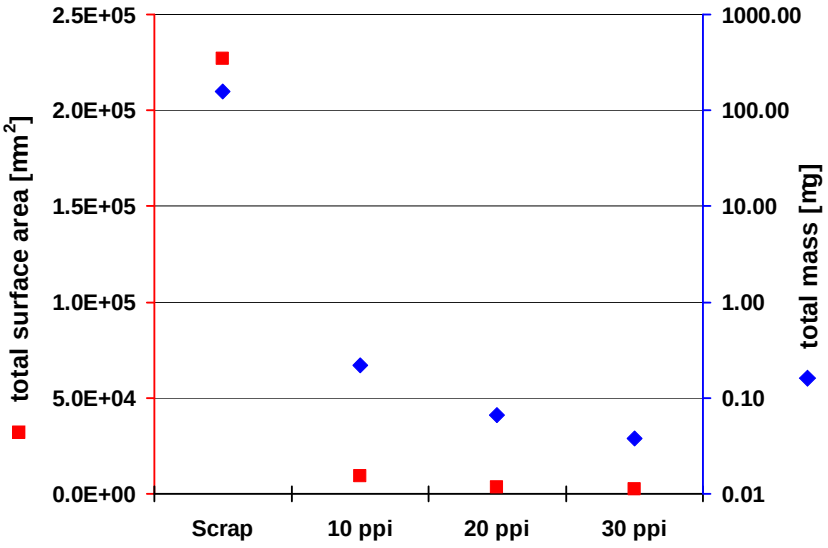

Figure 4.14: Total surface area and total mass of inclusions in 1 cm^2 area of silicon sample before and after filtration.

4.2.2 Inclusions captured by the filter

4.2.2.1 Inclusions captured at the top of the filters

After completing the filtration experiments, both the carbon and SiC filters were studied using light and electronic microscopy. Samples were prepared from filters with different pore sizes. After experiments were completed, special care was taken to remove the filters from the crucible without crating any damage and samples were analyzed without any mechanical preparation.

Figure 4.15 shows pictures taken with SEM of the top surface of the carbon filters. Many inclusions forming large clusters are captured at the top pores which are filled with silicon.

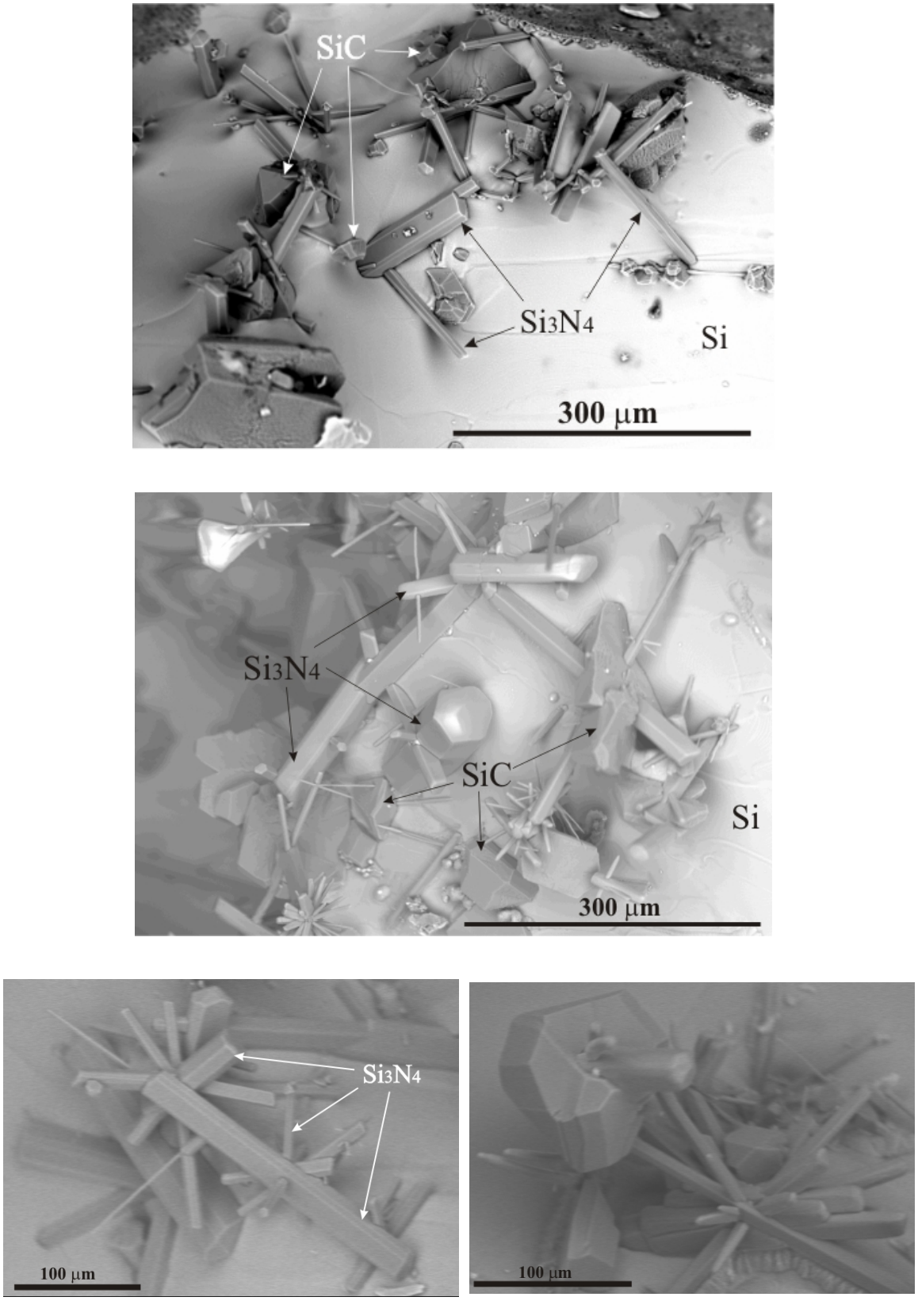

Figure 4.15: Inclusions captured at the top surface of 10 ppi carbon filters from Exp.3.

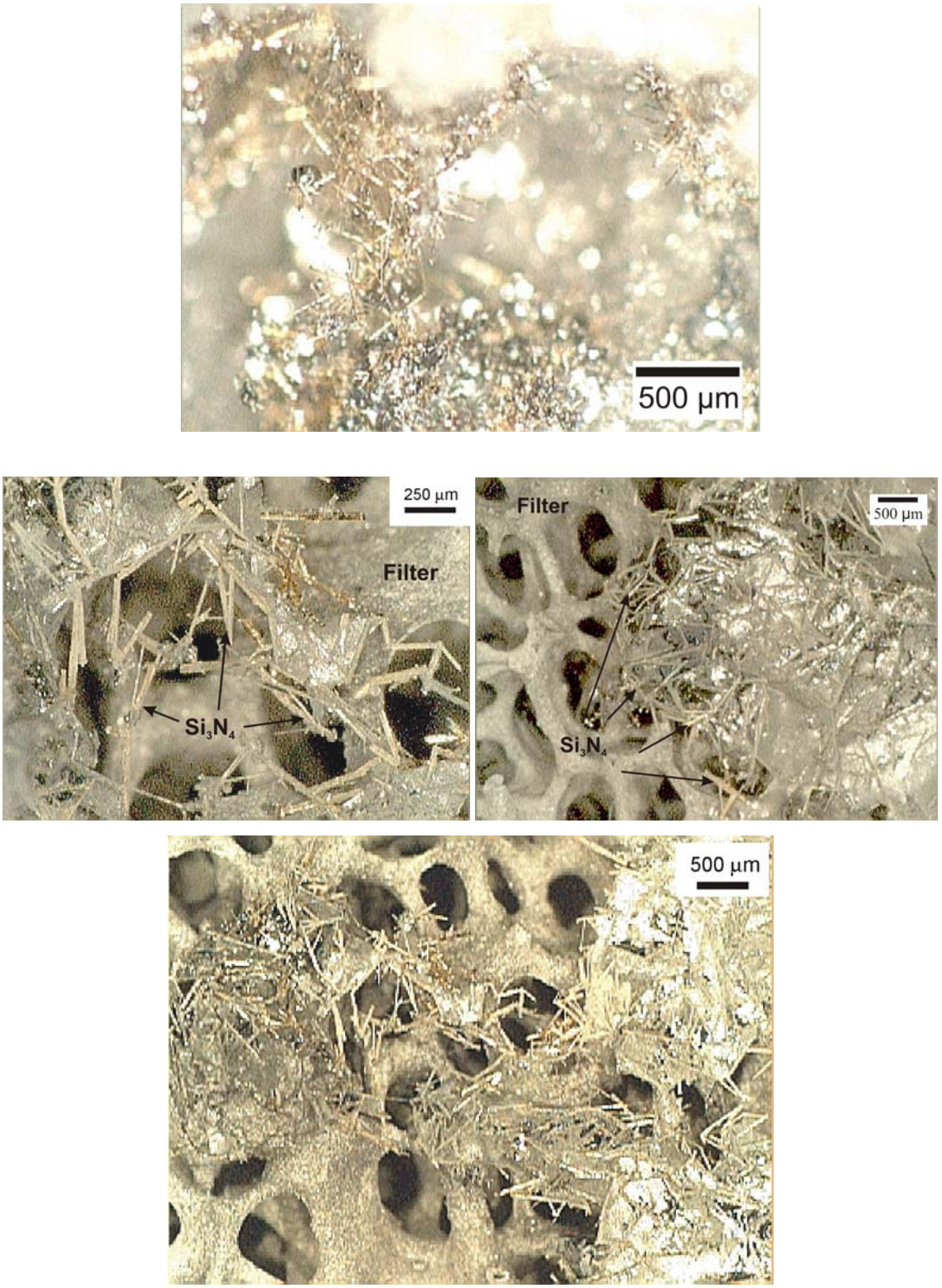

Figure 4.16: Inclusions captured at the top surface of a 10 ppi carbon filter from Exp.3 (picture at the top) and 30 ppi SiC filters from NF3 and NF4 (middle and bottom pictures).

After filtration, inclusions were mainly concentrated in certain parts of the top surface forming cakes as Figures 4.15 and 4.16 show. The particles that compose these cakes have a size that varies from several micrometers to several hundreds micrometers. The majority of them are large and their shape suggests that they are mostly Si_3N_4 particles. An accurate analysis of inclusion size distribution is not possible as these particles lie one above another. The cake created serves as a filter for other particles that come later during the filtration process. Small particles can be captured in these cakes even in the 10 ppi filters.

4.2.2.2 Inclusions captured inside filters

Filters with silicon remaining inside after filtration were cut horizontally and vertically and then were studied using light and electronic microscopy. The samples were ground and polished according to procedure described in section 3.2.1. Views of the upper pores of a 20 ppi SiC filter (Exp.9) are shown in Figure 4.17. The filter was cut horizontally and mounted in resin. The presence of carbide and nitride particles may be the reason why some silicon was trapped in the top layer of the filter. The filter pores were filled with silicon. These pictures show that many inclusions were captured, mainly SiC but also Si_3N_4. In the pictures in Figure 4.17, the Si_3N_4 particles appear darker than the SiC particles.

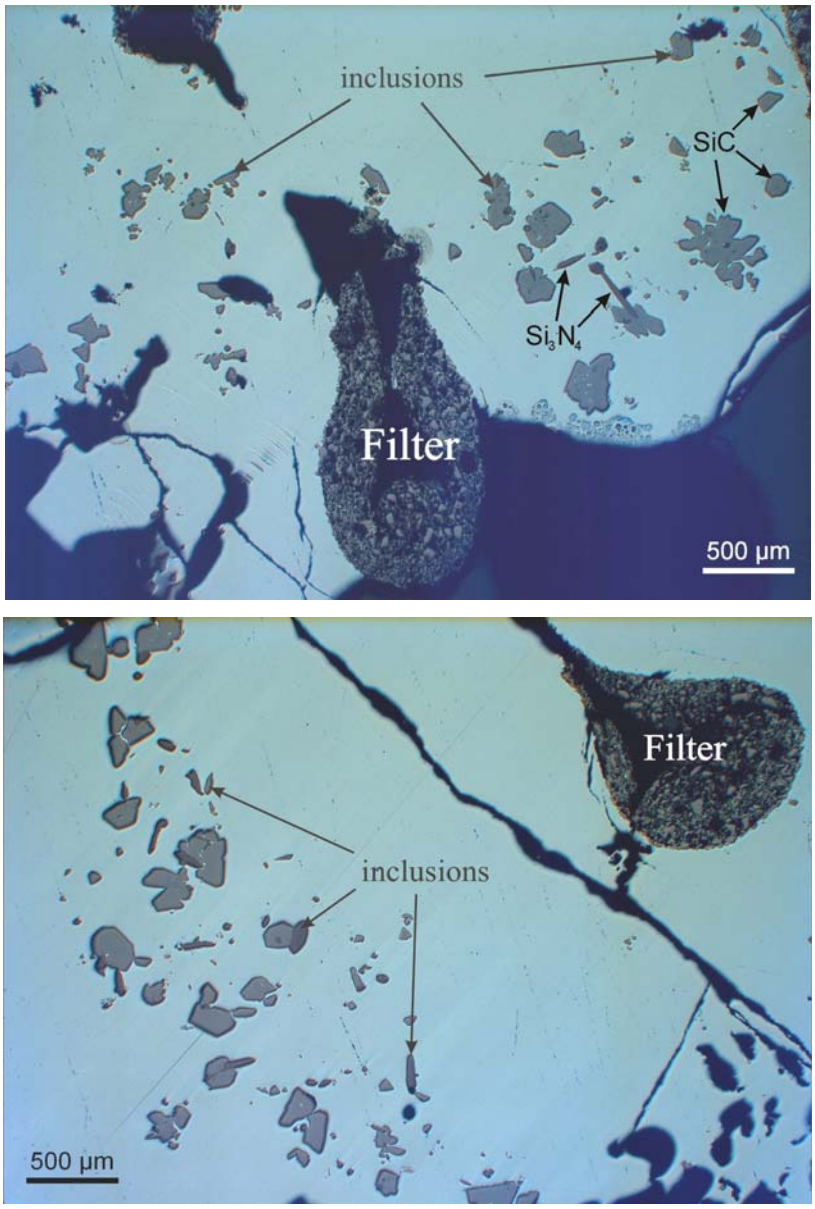

Figure 4.17: Inclusions captured at the top surface of a 20 ppi SiC filter (Exp.9).

Pictures of pores along the depth of a 10 ppi carbon filter (Exp.4) and of a 10 ppi SiC filter (Exp.6) are presented in Figure 4.18. Many SiC particles were found in the upper pores of the filter (Figure 4.18c and d). Many inclusion clusters were found close to the filter walls, and several clusters formed bridges that connect the pores of the filter. Only small Si_3N_4 inclusions were found collected in the top, as in Figure 4.17. The larger Si_3N_4 inclusions were too large to enter the pores and thus remained at the top surface of the filter. In the lower part of the filter, only a few SiC particles were found (Figure 4.18e and f).

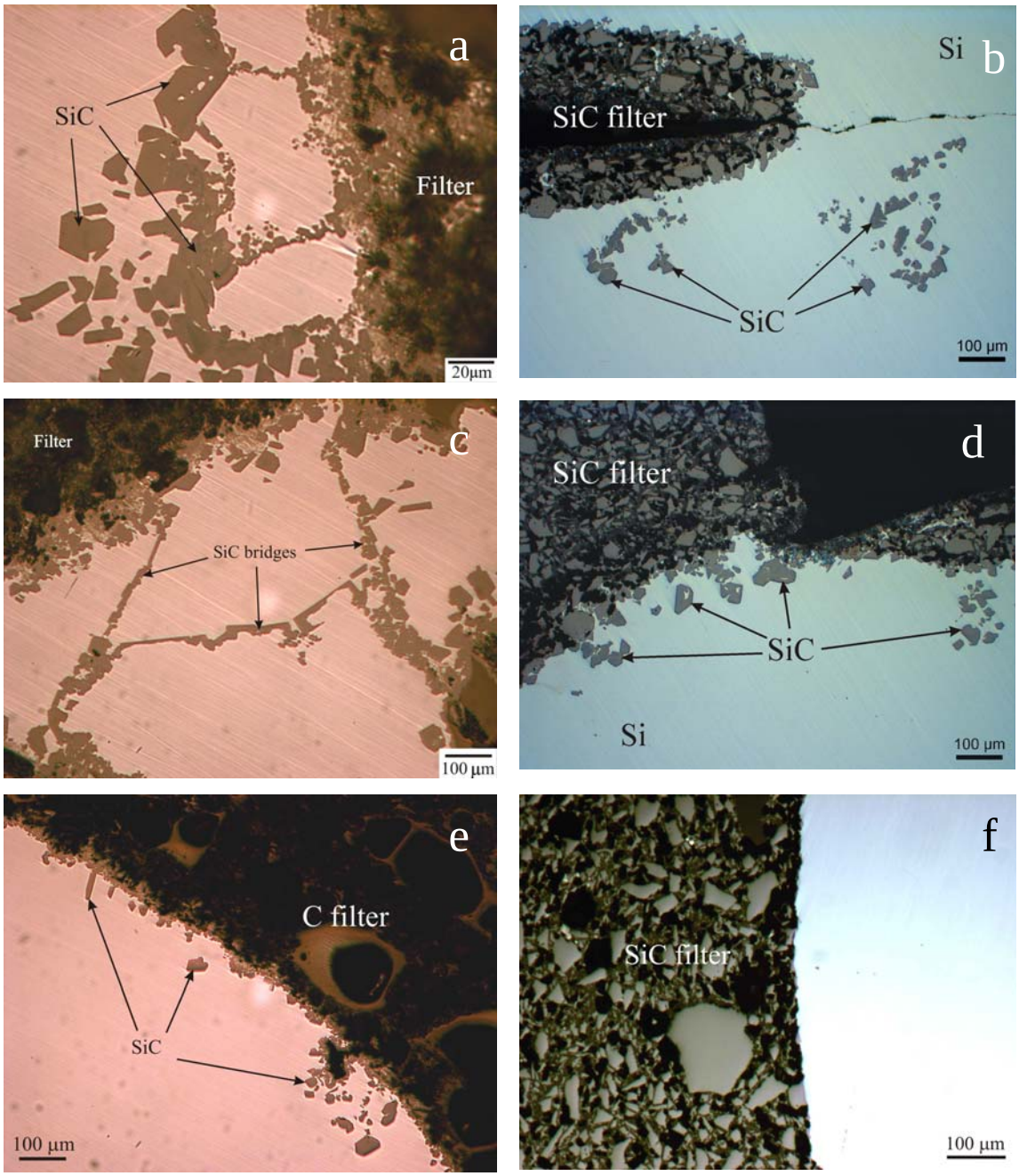

Figure 4.18: Inclusion attachment to a 10 ppi C filter (Exp.4) and to a 10 ppi SiC filter materials (Exp.6). (a) SiC bridges in the upper part of a C filter, (b) SiC particles in the upper part of the filter, (c) SiC bridges in the middle pores of a C filter, (d) SiC particles in the middle of a SiC filter, (e) few SiC particles at C filter bottom wall, (d) empty pore at bottom of the SiC filter.

SiC inclusions and <300µm Si_3N_4 inclusions were mainly removed in the upper section of the filter. More inclusions were found in the lower part of the 10ppi filters than in the 30ppi filters. The SiC inclusions found inside the filter pores may have come from inclusions in the input silicon or from the filter material itself. If these SiC inclusions come from the filter materials, Al and O from Al_2O_3 filter binder should also have been found. Pure SiC particles are most likely the SiC inclusions in the initial silicon. To clarify this issue, EPMA is used to map the region inside the filter where inclusions were captured, as shown in Figure 4.19.

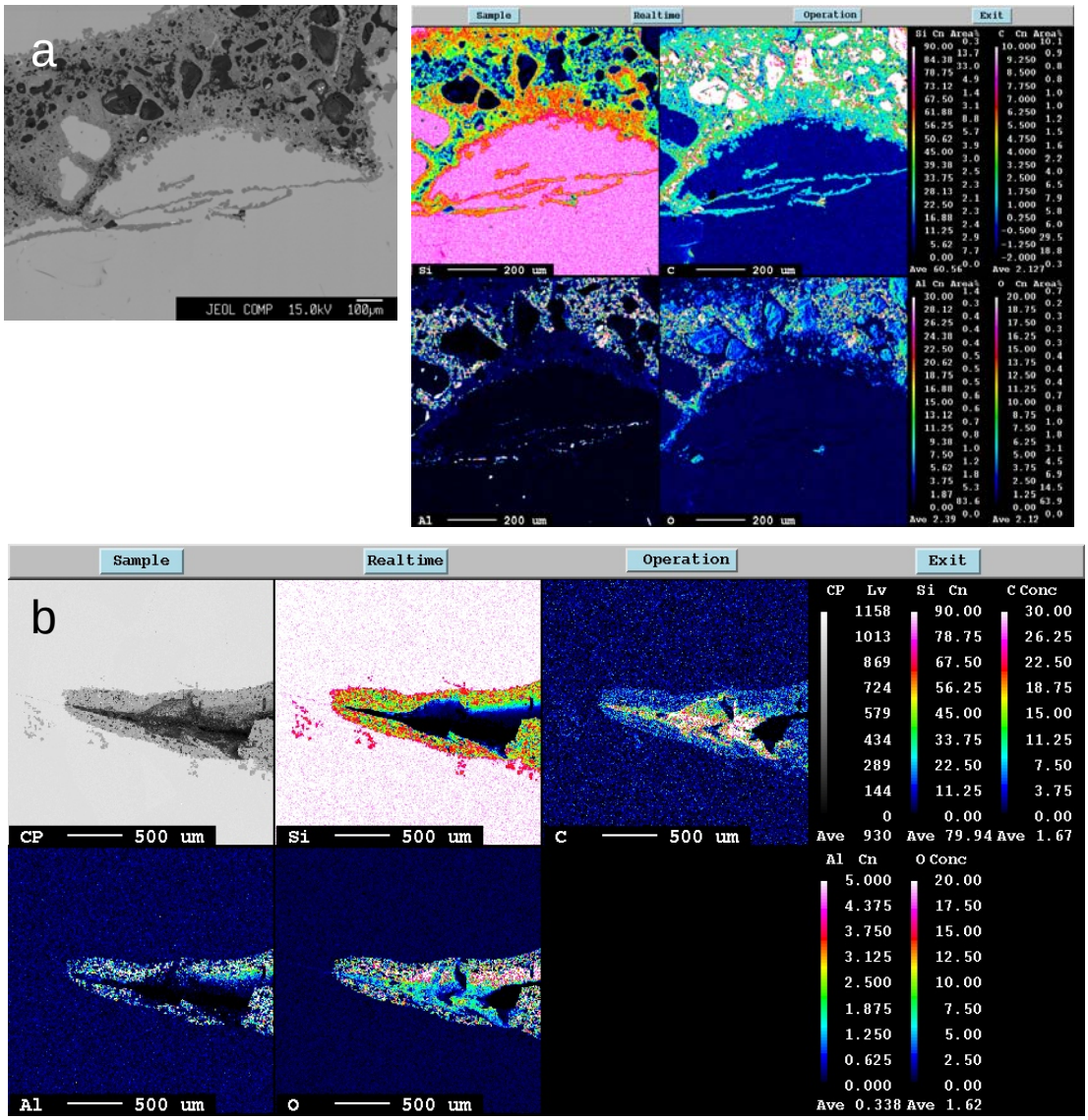

Figure 4.19: EPMA mapping of used filters. (a) 10 ppi C filter (Exp.1), (b) 10 ppi SiC filter (Exp.6).

The legend on the right side gives the mass percentage of the elements. For the SiC filter, it is clear that SiC particles (clusters and bridges) close to the filter materials are inclusions in the input silicon as no Al is present close to the particles. For the C filter, the bridges around the filter matrix contains Al and O, which means these bridges were not 100% original SiC inclusions and dissolution of the carbon filter in the silicon melt takes place.

To determine the inclusion distribution and their location inside the filter, a 10 ppi SiC filter (Exp.8) was cut vertically and a sample of the whole depth of the filter was observed using light microscopy. Figure 4.20 shows the distribution and location of the inclusions inside the filter. The main regions with inclusions are numbered. The SiC particles are entrapped not only at the upper pores but also in the pores at the bottom of the filter. This can be explained by the large pore size in comparison with the inclusion size. Figure 4.20 also shows higher magnified pictures of the main locations where inclusion clusters and bridges are found The upper pores are more filled with particles than the lower ones.

To observe the morphology and structure of the inclusion clusters and bridges, the sample was etched with the HF - HNO_3 acid mixture as described in Chapter 3. The etching solution dissolved the silicon that filled the pores. Figure 4.21 shows the pictures taken with an SEM. While the silicon was dissolved by the etching solution, the inclusions were left behind. Although special care was taken to keep the inclusions in their position, some of them were removed during etching. However, their “prints” were left in the sample, as shown in Figure 4.21. The inclusions are mainly SiC and a few Si_3N_4 particles assembled in clusters. As shown previously, the inclusions also form bridges.

Figure 4.22 shows a vertical cut of a 30 ppi filter (Exp.15). Notice that inclusions are also found in the bottom pores of the filter. However, their number is smaller than the number of inclusions captured in the upper pores.

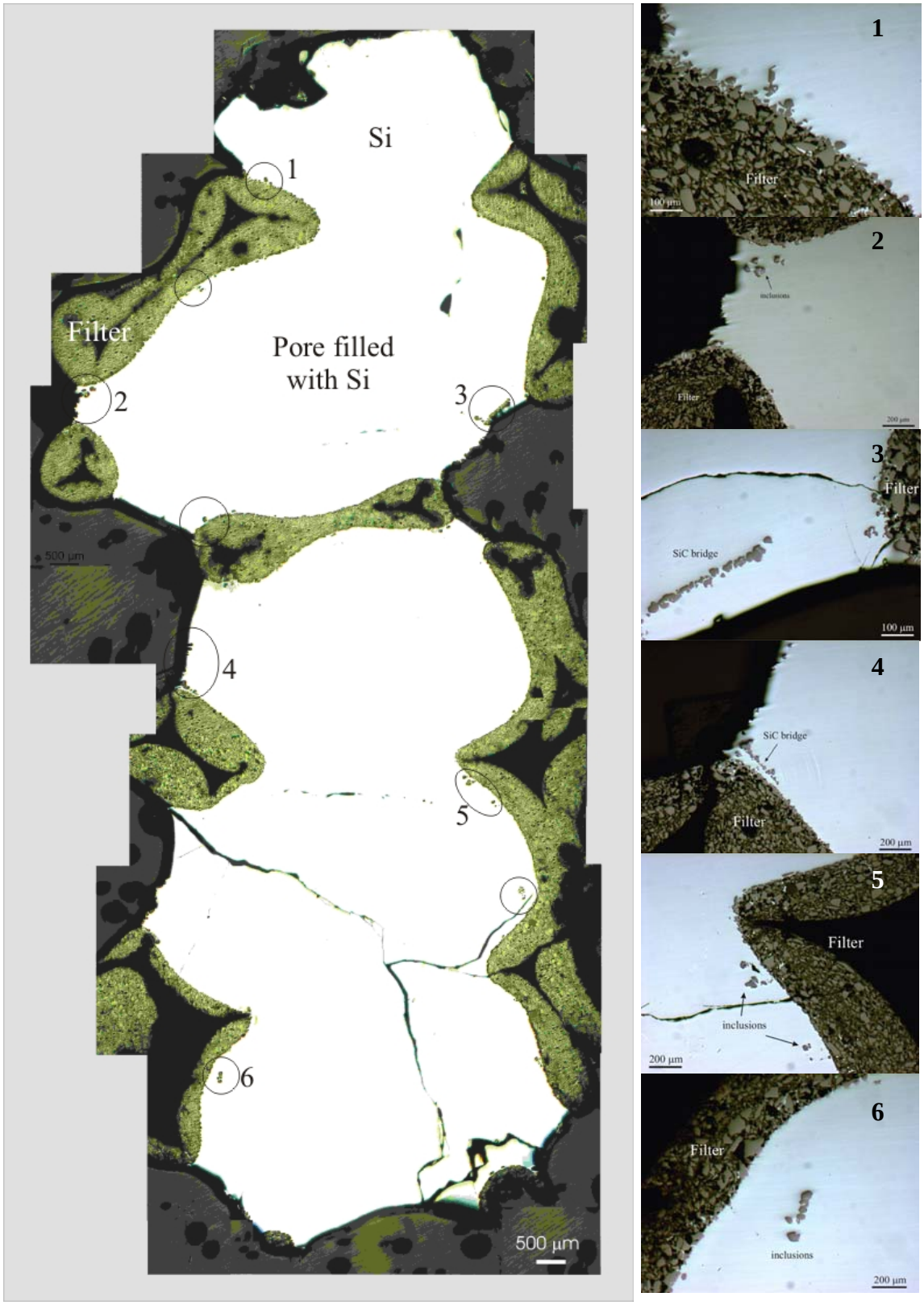

Figure 4.20: Vertical-cut section of a 10 ppi SiC filter (Exp.8). Right figures show magnified views of positions 1 - 6 in the left figure.

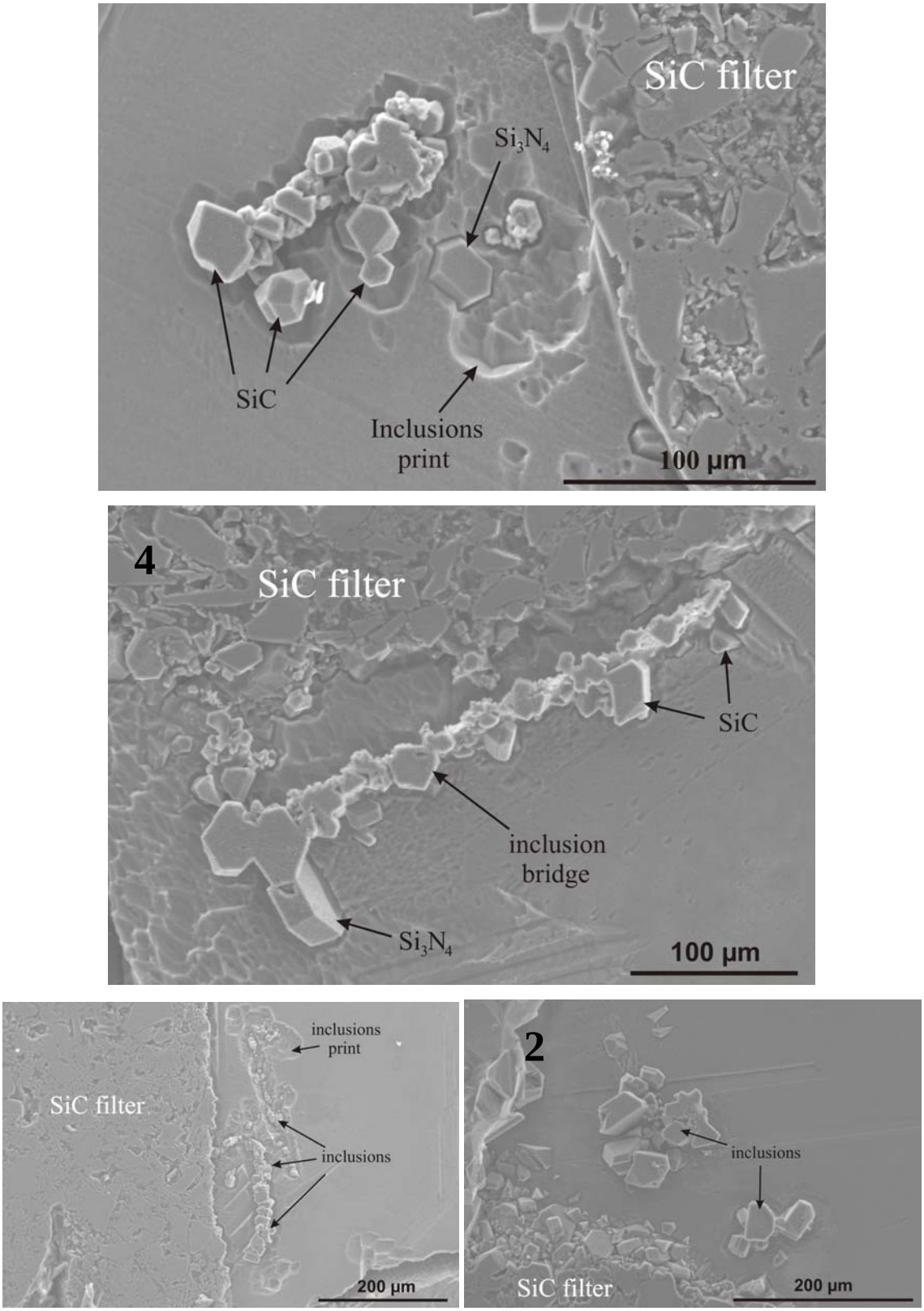

Figure 4.21: Inclusions captured inside the pores of the 10 ppi SiC filter from Exp.8 (SEM observation of partial etching samples).

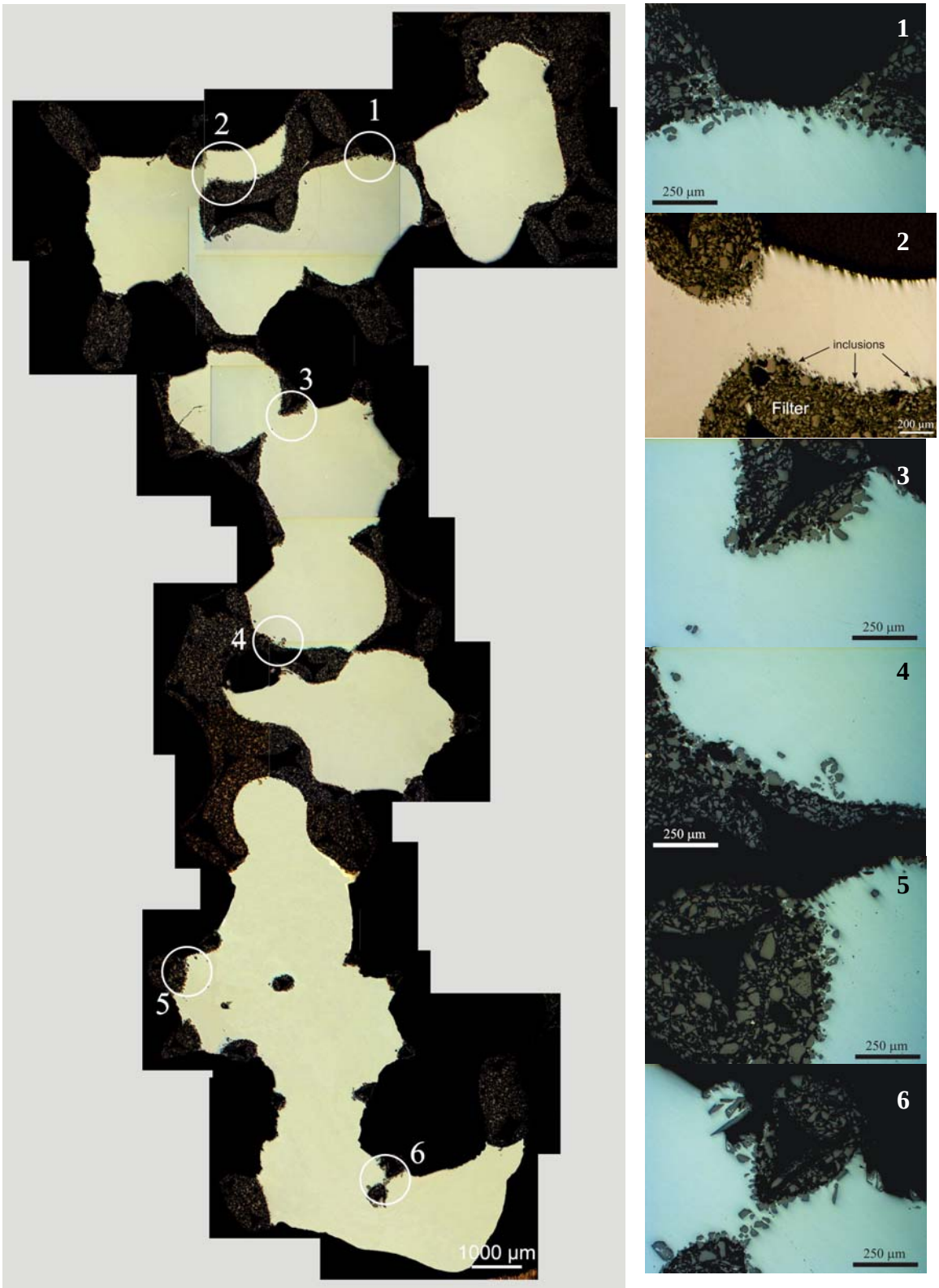

Figure 4.22: Vertical-cut section of a 30 ppi SiC filter (Exp.15). Right figures are magnified views of positions 1 - 6 in the left figure.

4.3 Wettability of molten silicon with refractories

4.3.1 Wetting of molten silicon with filter materials

Wetting of molten silicon was investigated on the carbon and SiC filter (85% SiC) substrates. As shown in Section 3.3.4.1, the filter substrates were prepared by grinding, sieving the powder and pressing it afterwards into tablets (disc shape) of 10 mm diameter and 2 – 3 mm height. The samples prepared in this way could not be analyzed for surface roughness as the technique would destroy the surface. Pictures from different stages of molten silicon above the filter substrates are shown in Figure 4.22 and 4.23. Time and temperature at these stages are also shown in the figure. Time t = 0 when the melting starts.

The contact angles of the molten silicon on the carbon filter substrate drop rapidly from about 95° to 0°. It takes only less than 4 minutes for the molten silicon to fully penetrate into the carbon filter substrate.

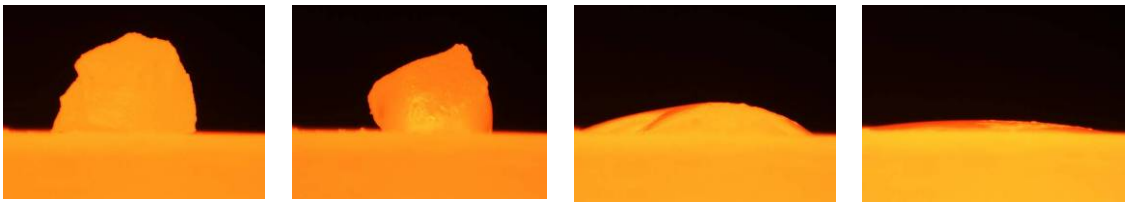

(a) T = 1400°C t = 0s. (b) T = 1420°C t = 82s (c) T = 1430°C t = 117s (d) T = 1450°C t = 197s

Figure 4.22: Stages of the silicon melting on a substrate from the carbon filter material.

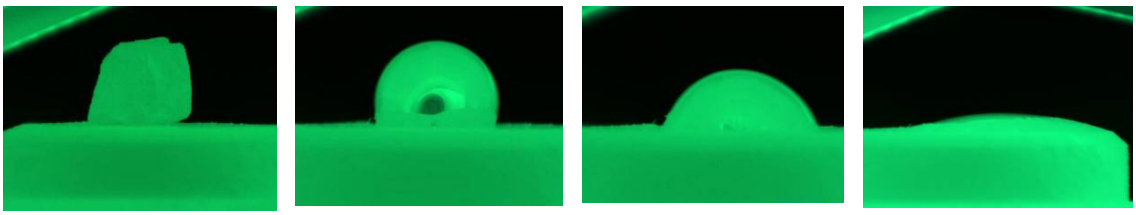

(a) T = 1400°C t = 0s. (b) T = 1420°C t = 75s (c) T = 1430°C t = 120s (d) T = 1450°C t = 440s

Figure 4.23: Stages of the silicon melting on a substrate formed from the SiC filter material.

The final contact angles of molten silicon on SiC filter substrate are about 18.7° and the time required to reach the stable value is about 10 minutes. Due to the fact that the substrate is made of pressed powder, the final contact angle results smaller than it would in a solid and pure SiC substrate. The molten silicon infiltrated the substrate but, the infiltration depth could not be measured.

4.3.2 Wetting of molten silicon with graphite materials

Substrates with different surface roughness were prepared from the graphite materials. The results are presented in Figures 4.24 – 33. Two figures are presented for each graphite material showing the variation of contact angle with time and the variation of the final contact angles with surface roughness, R_a. From these figures one can see that it takes 3 to 10 minutes for the molten silicon to reach the final contact angle, depending on the surface roughness value. When the surface is smooth (R_a < 0.1 μm) the final contact angle for all the graphites is about 30°. As the surface becomes rougher, the final contact angle decreases and it can reach even zero. In that case the silicon is absorbed completely by the graphite material. The average surface roughness for which the final contact angle becomes zero, is different for different graphite materials.

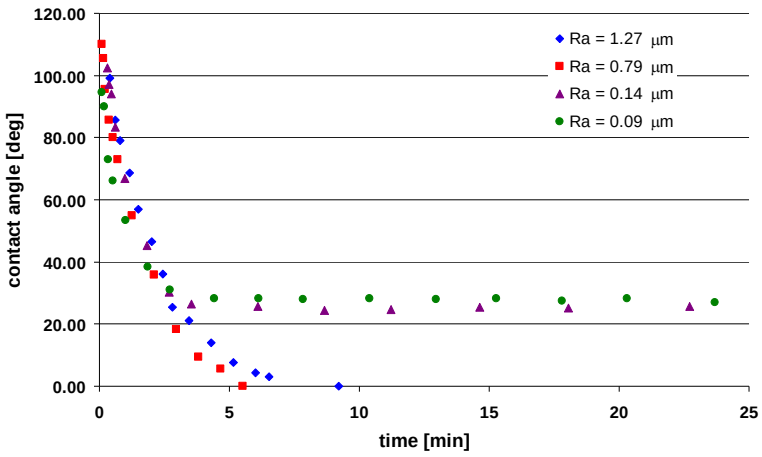

Figure 4.24: Contact angles of molten silicon versus time in IG11-graphite substrates with different surface roughness.

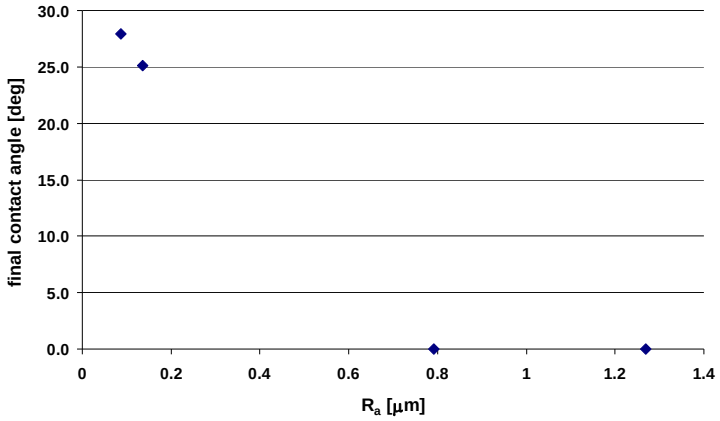

Figure 4.25: Final contact angles versus surface roughness, R_a, in IG11-graphite.

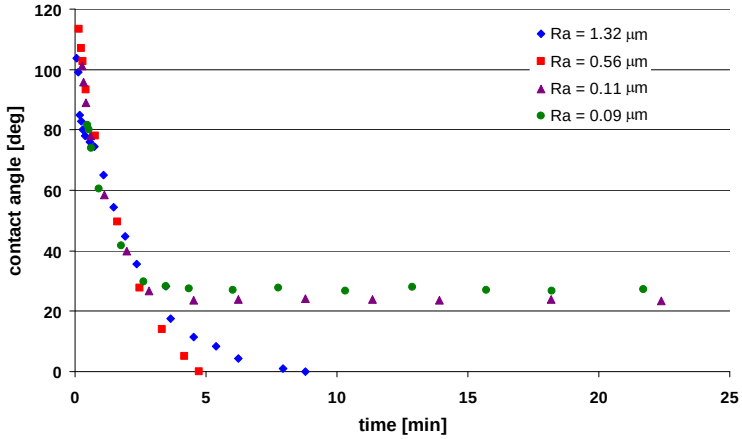

Figure 4.26: Contact angles of molten silicon versus time in ISEM3-graphite substrates with different surface roughness.

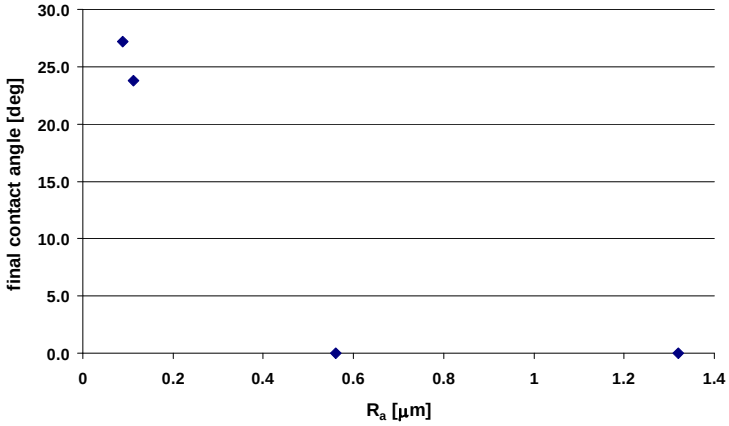

Figure 4.27: Final contact angle versus surface roughness, R_a, in ISEM3-graphite.

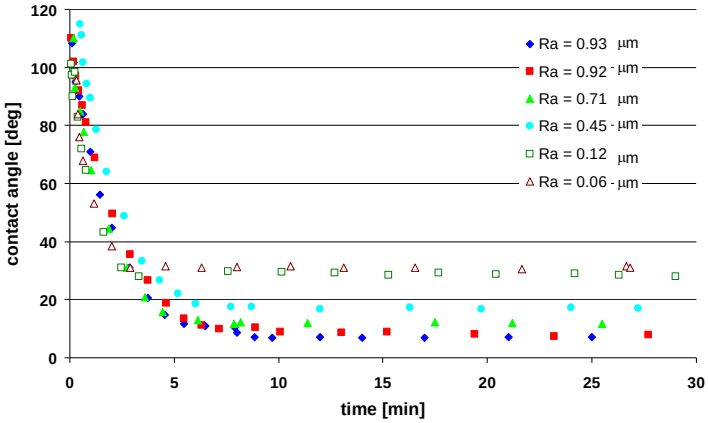

Figure 4.28: Contact angles of molten silicon versus time in ISO88-graphite substrates with different surface roughness.

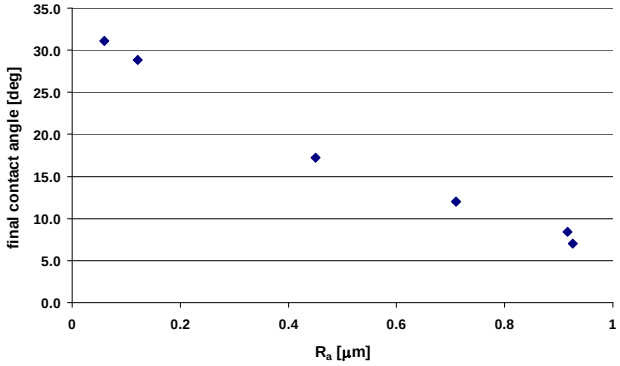

Figure 4.29: Final contact angles versus surface roughness, R_a, in ISO88-graphite.

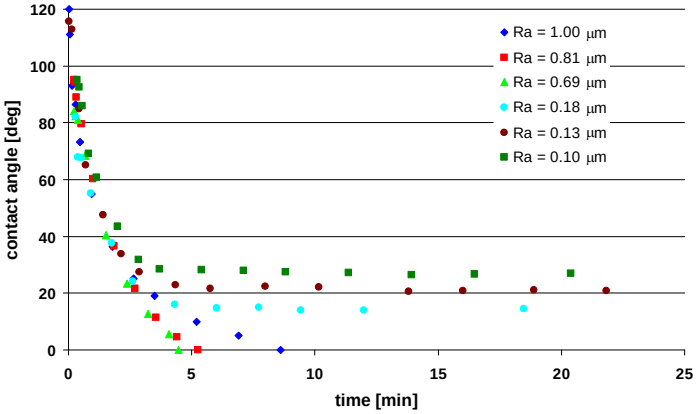

Figure 4.30: Contact angles of molten silicon versus time in SIC6-graphite substrates with different surface roughness.

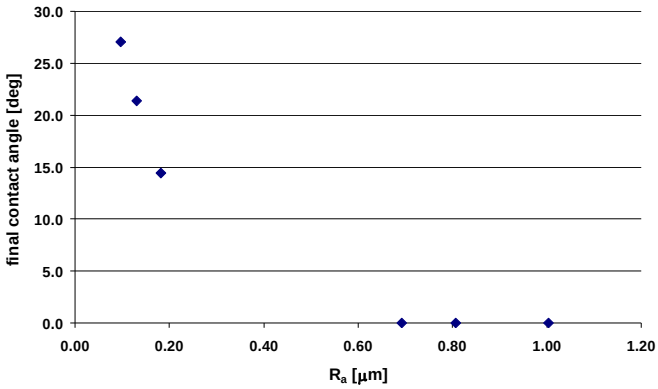

Figure 4.31: Final contact angles versus surface roughness, R_a, in SIC6-graphite.

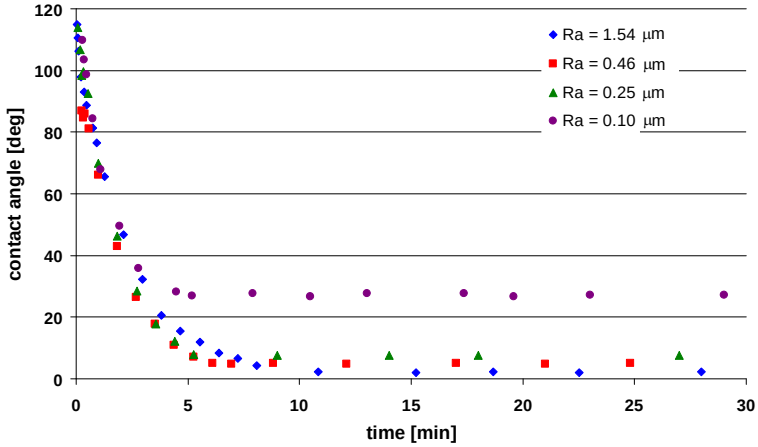

Figure 4.32: Contact angles of molten silicon versus time in IG610-graphite substrates with different surface roughness.

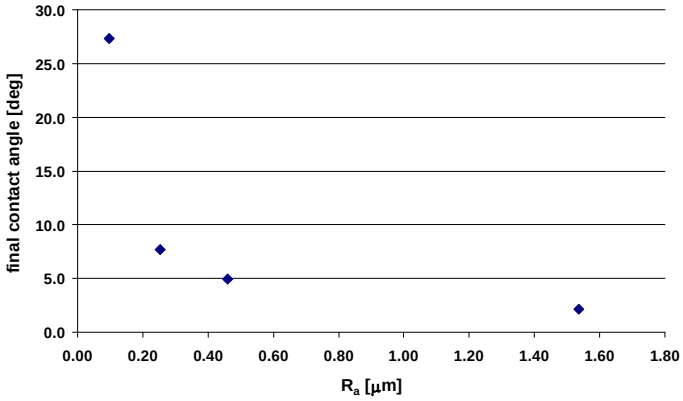

Figure 4.33: Final contact angles versus surface roughness, R_a, in IG610-graphite.

Table 4.7: Summary of contact angle values and surface roughness for the graphite materials.

IG11		ISEM3		ISO88		SIC6		IG610	
R_a [µm]	θ_F [°]	R_a [µm]	θ_F [°]	R_a [µm]	θ_F [°]	R_a [µm]	θ_F [°]	R_a [µm]	θ_F [°]
0.09	28	0.09	27	0.06	31	0.10	27	0.10	27
0.14	25	0.11	24	0.12	29	0.13	21	0.25	8
0.79	0	0.56	0	0.45	17	0.18	14	0.46	5
1.27	0	1.32	0	0.71	12	0.69	0	1.54	2
				0.92	8	0.81	0		
				0.93	7	1.00	0		

After wetting experiments the samples were molded into resin and cut in half to analyze their inner structure (see Section 3.2.1). First, maximum infiltration of molten silicon into the substrate was measured by light microscopy as shown in Figure 4.34. Figure 4.35 - 4.37 show the average infiltration depth of silicon versus average pore diameter, porosity and the bulk density of the graphite substrates. The average of the infiltration depth is calculated from all the values of each graphite material. The standard deviation data (STDV) are shown in brackets. Table 4.8 summarizes the results.

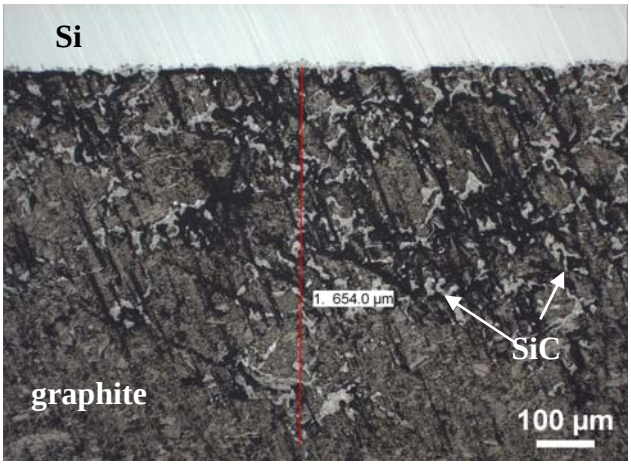

Figure 4.34: Light microscopy pictures that show the measurements of maximum infiltration depth in the graphite substrates IG11.

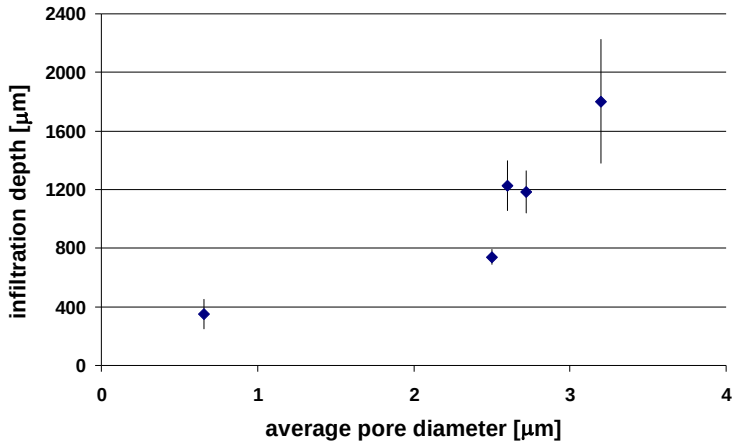

Figure 4.35: Infiltration depth of molten silicon versus the average pore diameter of the substrates.

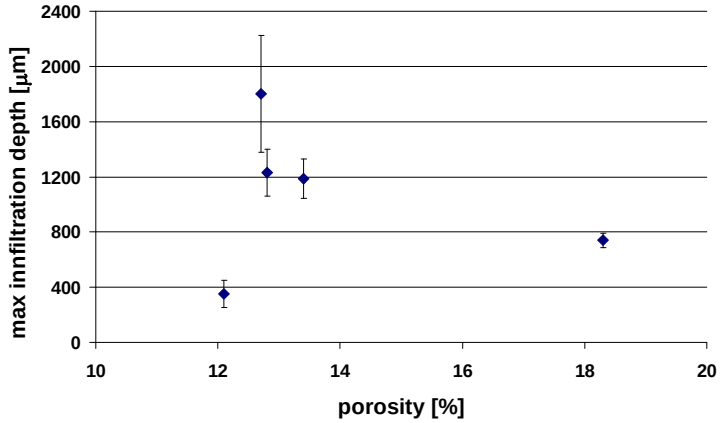

Figure 4.36: Infiltration depth of molten silicon versus the porosity of the substrates.

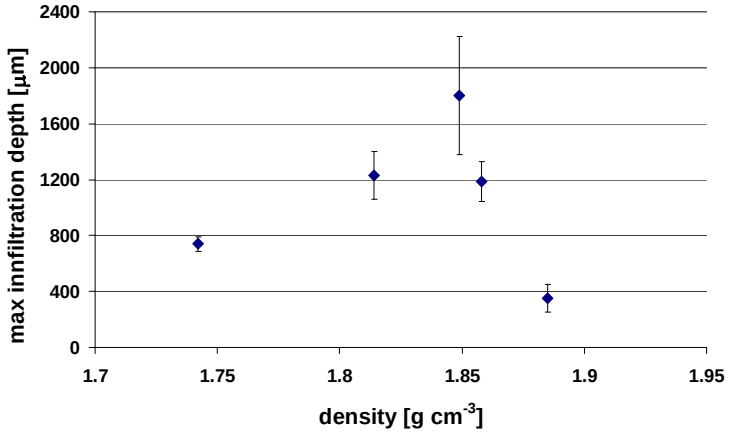

Figure 4.37: Infiltration depth of molten silicon *versus* bulk density of the substrates.

Table 4.8: Data of the infiltration depth, mean pore diameter and porosity of the graphites.

Substrate	Average pore diameter [μm]	Porosity [%]	Bulk density [g cm^{-3}]	Infiltration depth (STDV) [μm]
IG11	2.5	18.3	1.742	740 (103)
ISEM3	2.72	13.4	1.858	1186 (286)
ISO88	0.66	12.1	1.885	352 (202)
SIC6	3.2	12.7	1.849	1802 (847)
IG610	2.6	12.8	1.814	1229 (341)

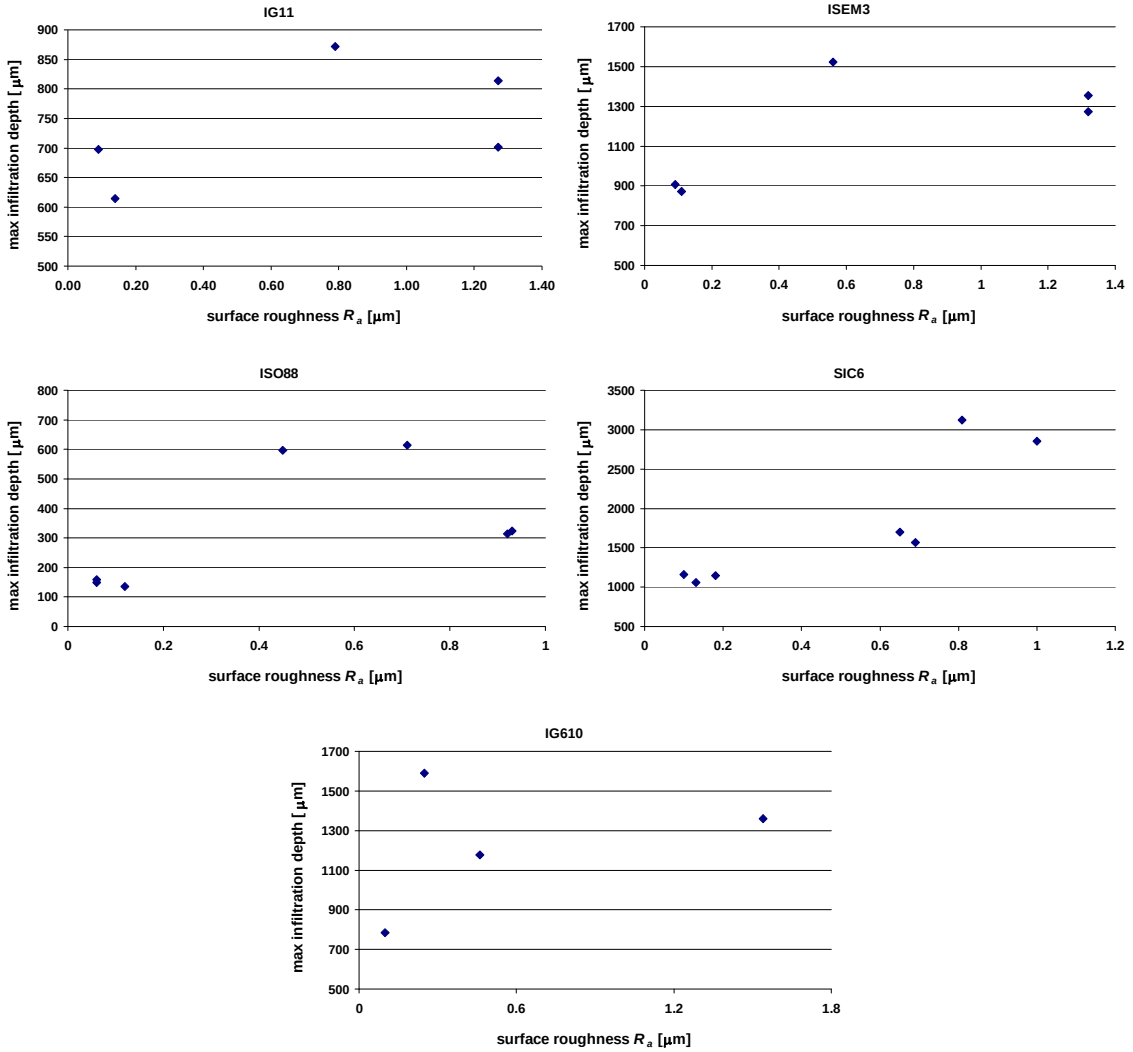

Figure 4.38: Maximum infiltration depth versus surface roughness for each graphite substrate.

From Table 4.8 one can see that the maximum infiltration depth of molten silicon changes with the surface roughness of the substrates for each graphite material. To show the variation of maximum infiltration depth versus surface roughness for all the graphite substrates these data are plotted in Figure 4.38.

Several samples after wetting experiments were submitted to EPMA analysis. Three pictures from IG11 and ISO88 taken with the same magnification are shown for comparison in Figure 4.39.

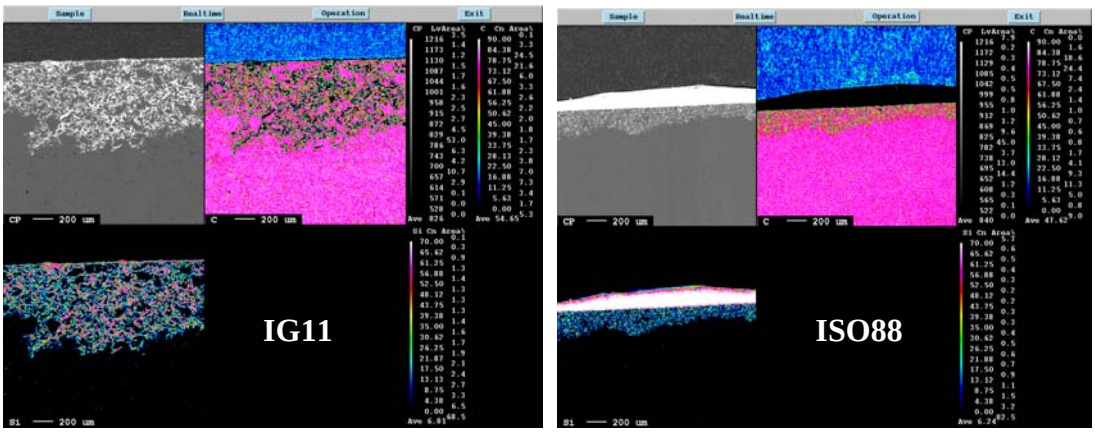

Figure 4.39: EPMA analysis of three substrates from IG11 and ISO88 showing the infiltration of molten silicon in these graphite materials.

Characterization of the substrates after wetting experiments was carried out using SEM and light microscopes. Figure 4.40 shows two SEM pictures from IG11 substrate, sample A1. The first picture shows the upper part of the substrate where the pores are filled with silicon. In the second picture of this figure, open pores in the bottom of the substrate are shown.

Figure 4.41 shows two pictures taken with light microscope. In the first picture (Figure 4.41-a) the molten silicon has fully infiltrated the graphite ISEM3. One can see the pores of the substrate filled with silicon and transformed into SiC afterwards. The final contact angle is 0°. Figure 4.41-b shows a picture of the graphite ISO88 after the experiment F5 where the silicon metal, the graphite and the reaction formed SiC layer can be seen. The microstructure of the SiC layer consists of individual SiC particles and a thin uniform SiC sub-layer underneath. The SiC particles have a diameter which can

reach tens of microns and are in direct contact with the silicon metal while the SiC sub-layer is in contact with the graphite material.

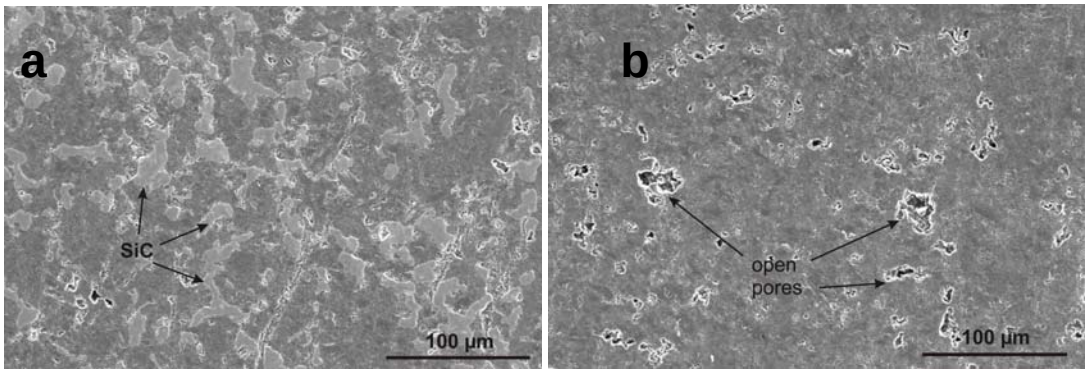

Figure 4.40: SEM pictures from IG11 substrate (sample A1) showing (a) pores filled with silicon and (b) open pores.

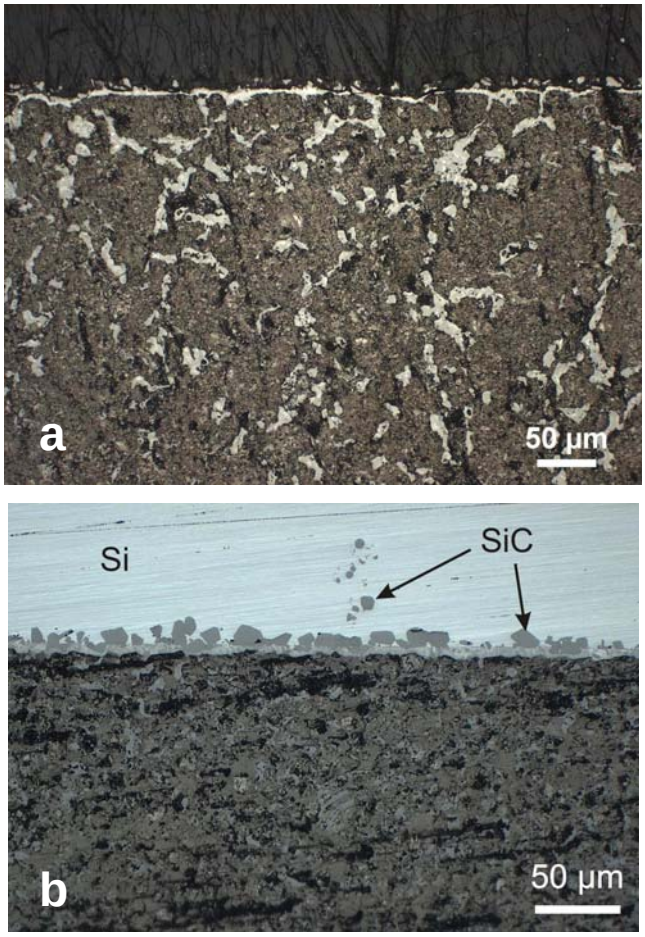

Figure 4.41: Light microscopy analysis of the substrates after wetting experiments; (a) ISEM3, (b) ISO88.

Chapter 5

DISCUSSION

Settling of SiC particles in molten silicon, filtration of inclusions in top-cut silicon scrap and, wettability of molten silicon with graphite materials are discussed. Several important topics are included. Thus, pushing and engulfment of SiC particles by a planar S/L solidification front, breakage of the planar S/L front into a cellular S/L front and its effect on pushing of particles are treated together with settling of SiC particles in molten silicon.

The mechanisms of filtration for SiC particles includes removal by interception and settling. Various filtration models are discussed, and a novel model for ceramic foam filters is developed and compared with experimental data.

Since wetting is important for filtration of molten silicon with the filter material, and for selection of graphite materials for use as refractories, wetting of graphites by molten silicon, and formation of a SiC layer in the interface between silicon and carbon materials is also dealt with. Finally, selection of graphite materials for use in the solar cell silicon industry is discussed.

5.1 Settling of SiC particles and pushing by the solidification front

5.1.1 Settling of SiC particles in molten silicon

As shown in Chapter 2, settling of solid particles in molten metals is described employing the Stokes law. In this ideal case particles are taken to be spheres, far enough from each other so that there is no interaction between them. Wall effects are neglected. and, it is assumed that there is complete mixing in the liquid.

Settling velocity, u_r (Equation 2.9), is taken as the mass transfer coefficient from melt to solid for the particle size distribution which is then given by the Equation 5.1 [Øvrelid *et al*. 2006].

$$\frac{f_N(d,t)}{f_N(d,t=0)} = \exp\left(-\frac{(\rho_{SiC} - \rho_{Si(l)})g}{18\mu h} t \cdot d^2\right) \tag{5.1}$$

where $f_N(d, t = 0)$ is the size distribution of the particles before the settling experiments at $t = 0$. $f_N(d, t)$ is the size distribution at time t. ρ_{SiC} is the density of SiC, $\rho_{Si(l)}$ is the density of molten silicon, g is the gravitational constant and, μ is the viscosity of molten silicon.

For a given settling time, Equation 5.1 gives:

$$\ln\left(\frac{f_N(d,t)}{f_N(d,t=0)}\right) = -k \cdot d^2 \tag{5.2}$$

where $k = \frac{(\rho_{SiC} - \rho_{Si(l)})g}{18\mu h} t$ (5.3)

The parameters used in the calculations are presented in Table 5.1. Viscosity of molten silicon is calculated using equation 5.4 [Rhim & Ohsaka, 2000]. The melting point of Si, T_m, is 1414°C.

$$\mu = 0.75 - 1.22 \times 10^{-3} (T - T_m) \text{ mPa s} \tag{5.4}$$

Density of molten silicon is obtained from the following equation [Handbook of Chemistry and Physics, 85th Edition, 2005]:

$$\rho(t) = \rho_m - 9.36 \times 10^{-4} (T_m - T) \tag{5.5}$$

As described in the experimental set-up, the settling step lasted for about 9 hours. Therefore, this time is considered as the settling time. An average temperature 1487°C is used in the calculation of viscosity.

Table 5.1: Data used in the calculation of *k*

Parameter	Value
μ	6.6×10^{-4} kg m^{-1} s^{-1}
$\rho_{Si(l)}$	2502 kg m^{-3}
ρ_{SiC}	3160 kg m^{-3}
h	0.1 m
g	9.8 m s^{-2}
t	32400 s

The particle size distributions in Solsilc silicon *before* the settling experiments (Figure 3.34) and *after* settling experiments shown in Figure 4.4 and 4.5 are plotted in the graph in Figure 5.1 and 5.2 for the cast FS-4A and FS-4B respectively. Only particles within the size range of 10 - 30 μm from the middle (17 – 76 mm) of the ingots are considered. This range of particle size is selected since secondary inclusions smaller than 10 μm may be present after settling. Samples are taken from the middle part of the ingot as the bottom part is contaminated with Si_3N_4 particles from the coating layer of the crucible, and the top part is enriched with impurities pushed by the solidification front. Results from the first 2 measurements are summed. Average values of particle sizes are employed in the graphs.

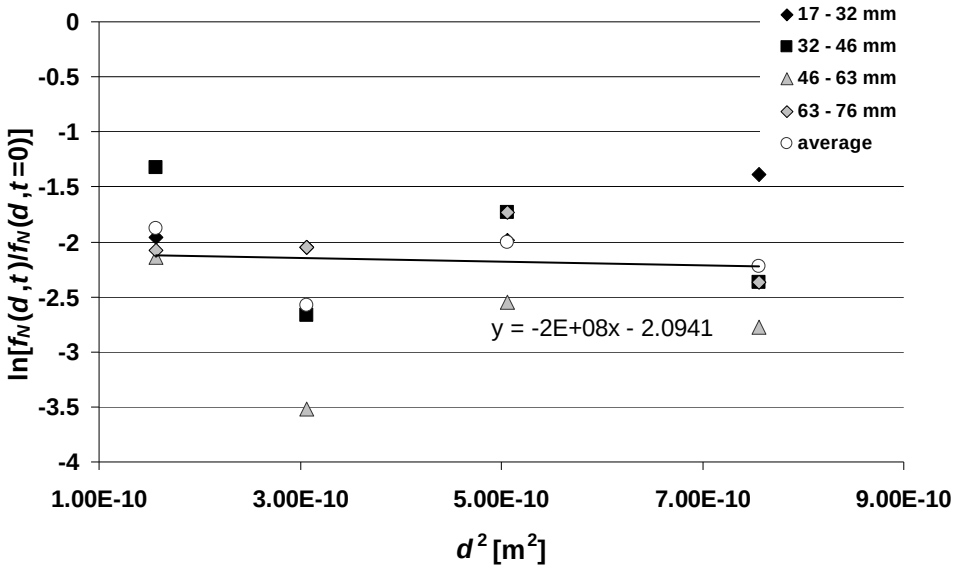

Figure 5.1: Plot of size distribution of SiC particles before and after settling experiments in the middle of the ingot FS-4A.

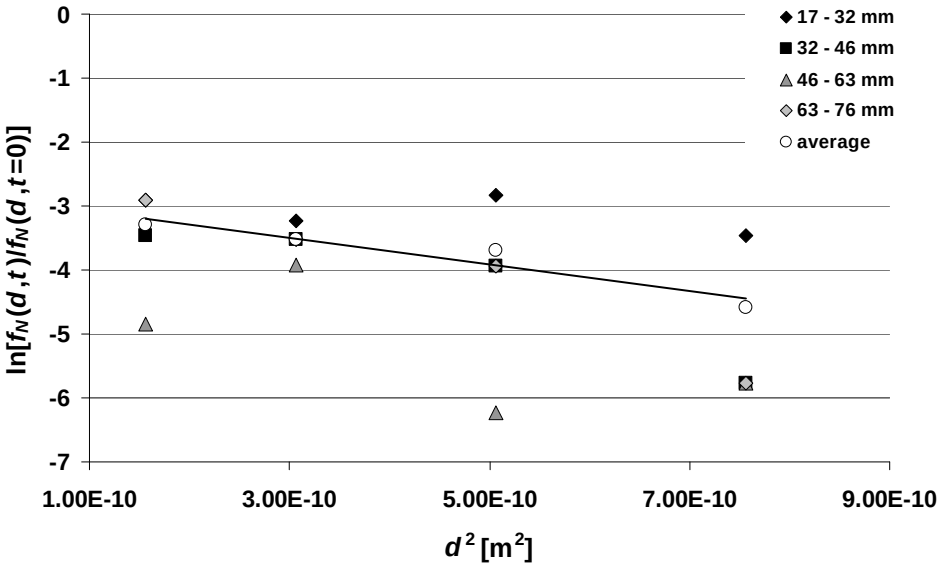

Figure 5.2: Plot of size distribution of SiC particles before and after settling experiments in the middle of the ingot FS-4B.

As it is seen from Figure 5.1 and 5.2 the plot of the experimental data does not satisfy Equation 5.2 indicating that the removal of SiC does not depend only on settling. Other mechanisms must play a role. Tables 5.2 and 5.3 give the data plotted in the

graphs in Figure 5.1 and 5.2 for the ingot FS-4A and FS-4B, respectively. The theoretical and the experimental values of *k* are given in Table 5.4.

Table 5.2: Number size distribution of particles in the middle of ingot FS-4A in 2 cm^2 before settling and engulfment.

d **(range) [μm]**	**Before settling**	**17 – 32 mm**	**32 – 46 mm**	**46 – 63 mm**	**63 – 76 mm**	**Average after**
12.5 (10 – 15)	128	18	34	15	16	21
17.5 (15 – 20)	101	13	7	3	13	9
22.5 (20 – 25)	51	7	9	4	9	7
27.5 (25 – 30)	32	8	3	2	3	4

Table 5.3: Number size distribution of particles in the middle of ingot FS-4B in 2 cm^2 before settling and engulfment.

d **(range) [μm]**	**Before settling**	**17 – 32 mm**	**32 – 46 mm**	**46 – 63 mm**	**63 – 76 mm**	**Average after**
12.5 (10 – 15)	128	7	4	1	7	5
17.5 (15 – 20)	101	4	3	2	3	2
22.5 (20 – 25)	51	3	1	0	1	1
27.5 (25 – 30)	32	1	0	0	0	0

Table 5.4: The calculated and experimental values of *k*.

k	**Value [m^{-2}]**
Calculated	1.8×10^{11}
FS-4A	2×10^{8}
FS-4B	2×10^{9}

For ingot FS-4B, *k* is two orders lower than the value calculated from the Equation (5.3). This indicates that removal of SiC inclusions by settling is less efficient than Stokes' law predicts. The molten silicon was directionally solidified, and indication is that SiC particles are pushed back by the solidification front towards the top of the ingot. Both pushing and engulfment are discussed in the following.

5.1.2 Pushing and engulfment of SiC particles by solidification front

As described in section 2.3.3, when a solidification front intercepts a solid particle, it can either push it or engulf it. Engulfment occurs through growth of the solid over and around the particle, followed by enclosure of the particle in the solid. As suggested in calculations from Søiland [2004] (Section 2.3.3), SiC particles with size smaller than 1.2×10^{-3} m are pushed by the planar solidification moving with a velocity of 5.5×10^{-6} m s^{-1}. In the Equation (2.15) formulated by Stefanescu *et al*. [1988] and used by Søiland [2004] to calculate pushing of SiC particles by a planar S/L front, the critical velocity, u_c, is derived from the interaction of two forces, the repulsive force between a particle and a S/L interface, F_r, and the drag force of a fluid on the particle, F_d. Thus, the Stokes force exerted on the particles and the lift force produced by the liquid flow parallel to the interface are not considered. The model is valid for non-terrestrial experiments under zero gravity and for very pure metals. Terrestrial experiments give rise to three additional forces on the particle which often mask the influence of those two fundamental forces, F_r and F_d, [Bune *et al*. 2000]. First, the gravitational (buoyancy) force on the particle is determined by the difference in density between the particle and the melt, $\Delta\rho$ and the g-level. Secondly, the particle experiences a lift force known as the Saffman force, F_S, due to the difference in melt velocity in the gap between the particle and the interface and that on the opposite side of the particle. Finally, the particle can experience an additional lift force due to particle rotation. This force is defined as the Magnus force, F_M [Bune *et al*. 2000], [Mukherjee *et al*. 2004].

Shangguan *et al*. [1992] argue that under the influence of gravity forces, the velocity of the particle itself does not significantly affect the critical velocity, because the particle velocity is very small compared to the critical interface velocity. The settling velocities for SiC particles within the size range of 1.0×10^{-6} - 4.0×10^{-5} m (1 – 40 μm) are given in Table 5.5. Comparing these velocities with the respective critical interface velocities, u_c, as calculated by Søiland [2004] (see Figure 2.10), we conclude that for particles larger than 15 μm the particle velocity affects the critical velocity of the pushing / engulfment process. Therefore, the critical velocity it is lower than what the model predicts.

The difficulty in verifying and applying the models by experiments lies in the fact that these models are valid for pure metals. Predictions made by the models fail in the case of impure matrices as the critical velocity suffers an extreme reduction even for impurities in the ppm region [Hecht & Rex, 1997].

Table 5.5: Settling and critical velocities of SiC particles in molten silicon calculated for experimental conditions.

d [m]	u_r [m s^{-1}]	u_c [m s^{-1}]
1×10^{-6}	5×10^{-7}	7×10^{-3}
5×10^{-6}	1×10^{-5}	1×10^{-3}
1.0×10^{-5}	5×10^{-5}	7×10^{-4}
1.5×10^{-5}	1×10^{-4}	5×10^{-4}
2.0×10^{-5}	2×10^{-4}	4×10^{-4}
3.0×10^{-5}	5×10^{-4}	2×10^{-4}
4.0×10^{-5}	9×10^{-4}	1×10^{-4}

The main metallic impurities present in the Solsilc silicon are Al, Fe and Ti, but exact data on their concentration levels is missing. The carbon content is around 700 mass ppm. The partition ratio for these elements is given in Table 5.6. These impurities together with the SiC inclusions pushed by the solidification front will accumulate in the upper part of the ingot.

Table 5.6: Partition ratio for the main impurities in Si [Hull, 1999].

Element	k_0
C	0.07
Al	2.0×10^{-3}
Fe	8.0×10^{-6}
Ti	3.6×10^{-4}

When the concentration of impurities ahead of the S/L interface reaches a certain level, engulfment of particles will occur. The situation will resemble that of an alloy where the critical interface velocity is much lower than for the pure melts [Kim & Rohatgi, 1998]. The difference in thermal conductivity, which is the driving force for pushing of particles in pure melts, will not have any effect in pushing of the particles in alloys because it is much higher than the diffusivity of the solute in the liquid. According to Schvezov & Weinberg [1985] the thermal gradient at the S/L interface has no measurable effect on the critical velocity when the particle size is smaller than 5×10^{-4} m (500 μm).

If the planar solidification front breaks down into cells, two solidification fronts can converge on the particle. In this case, if the particle is not engulfed by one of the fronts, it will be pushed in between the solidification fronts at the tips of the cells, and finally be entrapped at cell boundaries (see Figure 2.9) [Stefanescu *et al*. 1988]. The results for cast FS-4B are shown again in Figure 5.3 together with a picture of a vertical cut of ingot FS-4B. The pattern of the grain boundaries that can be seen from this picture indicates that the breakage of solidification front from planar to cellular has occured in the upper 3 centimeters of the ingot. In this region the content of SiC particles is high.

Figure 5.4 shows the aluminum and iron precipitates in the upper part of the ingot, giving another proof of the breakage of the S/L interface from planar to cellular. As mentioned in Section 2.3.3.1, the interface breaks down due to accumulation of dissolved elements [Juel, 2008] and pushed particles ahead of solidification front. Figure 5.5 shows a SiC particle entrapped between two cellular fronts in ingot FS-4B.

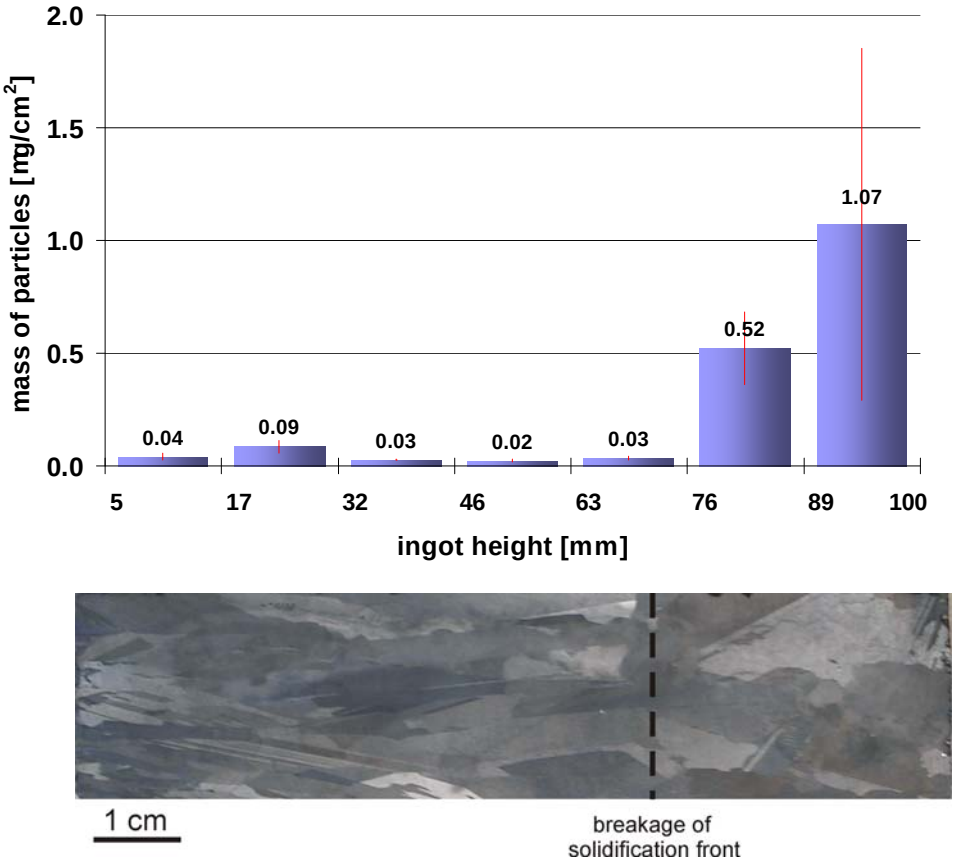

Figure 5.3: Breakage of the planar solidification front to cellular front in the upper 2 centimeters of the ingot FS-4B.

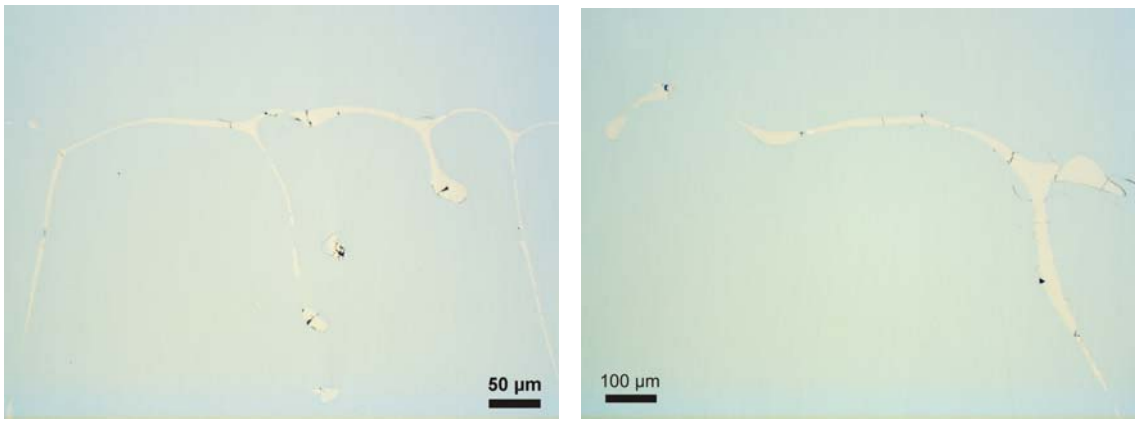

Figure 5.4: Precipitates of impurities, mainly Al and Fe, along grain boundaries in the top of the ingot FS-4B.

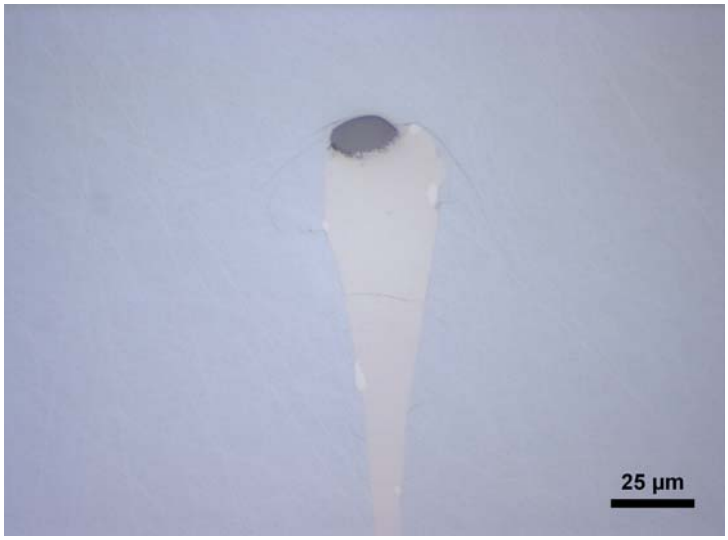

Figure 5.5: Entrapment of a SiC particle in the cell boundaries

This could explain the presence of SiC particles in the upper part of the ingot. All the particles counted and measured in the middle of the ingot (17 – 76 mm from the bottom of the ingot) are considered to be engulfed particles. All the particles counted and measured in the top of the ingot (76 – 100 mm from the bottom of the ingot) are considered as pushed by the S/L interface.

Taking into consideration settling, pushing and engulfment, a mass balance of the SiC particles could be formulated. Collision and growth of particles are neglected.

Mass of the particles before refining = Mass of settled particles (found in the bottom) + Mass of pushed particles (found in the top) + Mass of the engulfed particles (found in the middle of the ingot)

In terms of particle size distribution we have:

$$f_N(d) = f_{N,\,\text{settling}}(d) + f_{N,\,\text{pushing}}(d) + f_{N,\,\text{engulfment}}(d) \qquad (5.6)$$

The number size distribution of the particles at the top of the ingot (76 – 100 mm) in 2 cm^2 observed area are given in Table 5.7 and 5.8 for the ingot FS-4A and FS-4B respectively. Size distributions of the particles that have settled in the bottom of the ingots are not possible to measure because the SiC particle have agglomerated and formed clusters together with Si_3N_4 particles as shown in section 4.1.2, Figure 4.3. Data from 2 cm^2 of the samples before and after refining are given in Table 5.9 and 5.10.

Table 5.7: Number size distribution of pushed particles in 2 cm^2 of the upper part in the ingot FS-4A.

d **(range) [μm]**	**76 – 89 mm**	**89 – 100 mm**	**Average**
12.5 (10 – 15)	33	16	25
17.5 (15 – 20)	11	9	10
22.5 (20 – 25)	12	6	9
27.5 (25 – 30)	4	5	5

Table 5.8: Number size distribution of pushed particles in 2 cm^2 of the upper part in the ingot FS-4B.

d **(range) [μm]**	**76 – 89 mm**	**89 – 100 mm**	**Average**
12.5 (10 – 15)	13	13	13
17.5 (15 – 20)	5	5	5
22.5 (20 – 25)	8	4	6
27.5 (25 – 30)	2	1	2

Table 5.9: Number size distribution of particles before and after refining in ingot FS-4A.

d **(range) [μm]**	**Before settling**	**engulfed**	**pushed**
12.5 (10 – 15)	128	21	25
17.5 (15 – 20)	101	9	10
22.5 (20 – 25)	51	7	9
27.5 (25 – 30)	32	4	5

Table 5.10: Number size distribution of particles before and after refining in ingot FS-4B.

d **(range) [μm]**	**Before settling**	**engulfed**	**pushed**
12.5 (10 – 15)	128	2	13
17.5 (15 – 20)	101	2	5
22.5 (20 – 25)	51	1	6
27.5 (25 – 30)	32	0	2

Tables 5.9 and 5.10 indicate that pushing is more important than engulfment for the systems studied. The difference of the particles before settling and the particles pushed + engulfed by the S/L interface gives the settled particles.

5.1.3 Precipitation of SiC particles during solidification

The calculated value of *k* is 3 orders higher than the experimental value of ingot FS-4A (Table 5.4) indicating that for the ingot FS-4A removal of particles by settling is far less efficient than Stokes' law predicts. One of the reasons might be the SiC precipitates found in the ingot FS-4A. According to Möller *et al*. [2008] if the carbon content at the SL interface is above the maximum solubility limit, ~ 5×10^{18} cm^{-3} (~ 43 mass ppm) then SiC particles will precipitate at the SL interface. Möller [Möller *et al*. 2008] argue that there is formation of SiC planar layers along the grain boundaries. In the light microscopic analysis of the samples from the ingot FS-4A, many such SiC precipitates are observed. These are shown in Figure 5.6.

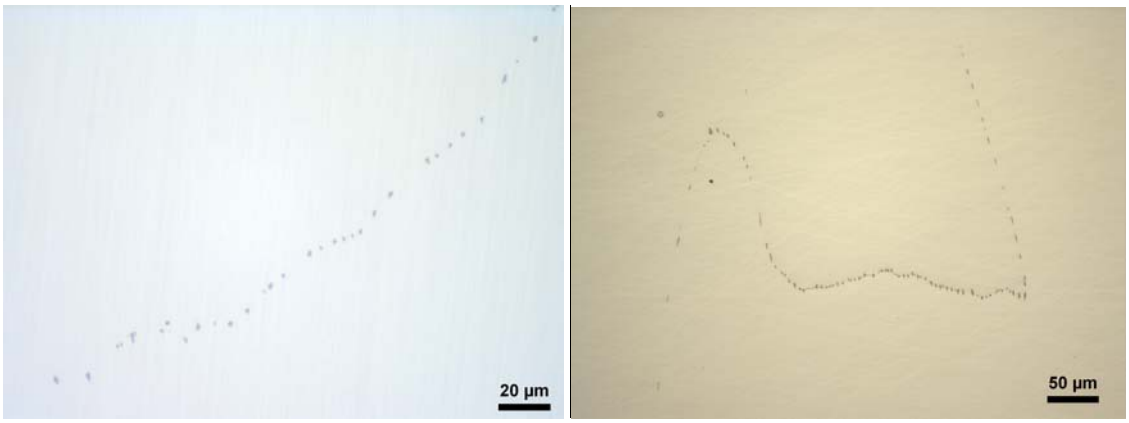

Figure 5.6: SiC precipitates along grain boundaries in the ingot FS-4A.

The presence of Si_3N_4 particles introduces an error in the measurements. As shown in Section 3.3.1 SiC particles are in many cases are found together with Si_3N_4 ones. This takes place in both ingots, but more often in ingot FS-4A. Figure 5.7 shows two pictures from ingot FS-4A where Si_3N_4 particles are present both as separated particles and as clusters with SiC inclusions. An estimate of the effect of this error on our results was not attempted.

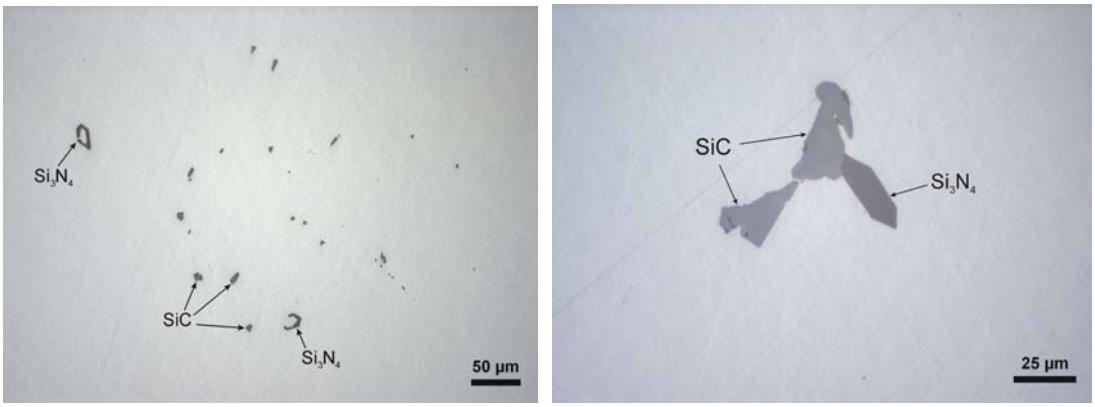

Figure 5.7: Si_3N_4 particles present in ingot FS-4A both as separated particles and as clusters with SiC inclusions.

5.2 Particle size distribution of inclusions in silicon

In particle size analysis often only a single property of the particle is measured and usually this property refers to a sphere [Rawle, 2008]. Then, the diameter of the sphere is calculated. This is often called “equivalent diameter” of the particle and the method is named as equivalent sphere theory. Many particle sizing techniques are based in this principle. They measure mass, volume, surface area, projected area, etc. of the particles and as a result give the equivalent diameter (size) or the particle [Etzler, 2004]. A summery on some common techniques used in particle size analysis is given in Table 5.11 [Shekunov *et al*. 2007].

Table 5.11: Characteristics of some commonly used particle sizing techniques [Shekunov *et al*. 2007].

Technique	Method	Equivalent particle diameter	Effective measuring range [μm]	Most representative PSD
Optical image	Direct imaging	Projected area	3 - 150	Number-weighted
SEM	Direct imaging	Projected area	0.01 – 150	Number-weighted
LD	Low-angle (Fraunhofer) diffraction ring measurement	Angular-averaged linear (Feret's)	0.5 – 1000	Volume-weighted
DLS	Measurement of light intensity correlations from particles in Brownian motion	Hydrodynamic	0.003 – 3	Volume-weighted
Coulter counter	Electrical zone-sensing	Volume	0.6 – 1200	Volume-weighted
TOF	Measurement of particle velocity in expanding air flow	Aerodynamic, ultra-Stokesian	0.5 – 200	Number-weighted
CI	Inertial particle impaction as a function of air velocity	Aerodynamic, ultra-Stokesian	0.5 - 10	Mass-weighted

SEM Scanning electron microscope; ***LD*** laser diffraction; ***DLS*** dynamic light scattering; ***TOF*** time-of-flight; ***CI*** cascade impactor.

The shape of the particles is very important for the size distribution [Harker *et al*. 2002], [Etzler, 2004]. For particles whose shape differs significantly from that of the sphere, for example needles and discs, the equivalent calculated diameters may vary using different techniques. An example of such particles is given in Figure 5.8. A picture of acetaminophen (AP) particles, and the data on the mean equivalent diameter on by three different techniques are shown. The large discrepancy in the mean equivalent diameter may be due to the fact that the instruments operate on different physical principles and are calibrated for spherical, nonagglomerated particles [Shekunov *et al*. 2007].

(a) 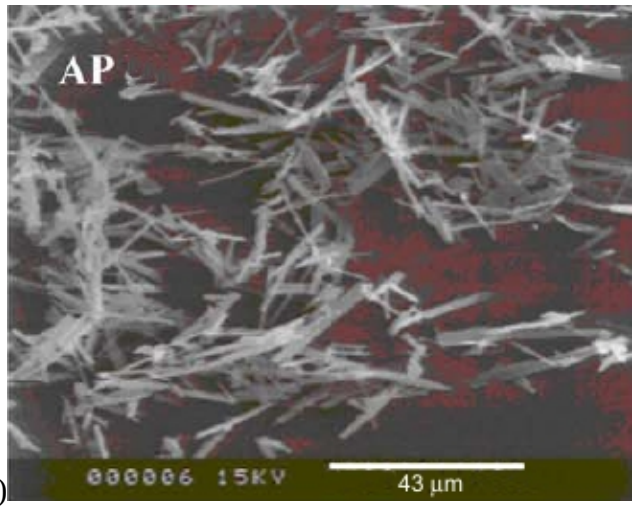

(b) 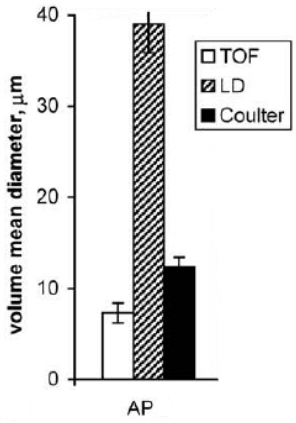

Figure 5.8: (a) Particle morphology of needle-like crystals of acetaminophen (AP) and (b) its mean volume equivalent diameter measured by time of flight (TOF, AeroSizer^{TM} with AeroDisperser, TSI Inc, USA), laser diffraction (LD, Helos/Rodos, Sympatec GmbH, Germany) and Coulter counter (Coulter Multisizer II, Coulter Electronics GmbH, Germany) instruments [Shekunov *et al*. 2007].

Among the techniques widely used, microscopy is often applied as an absolute particle sizing method because this is the only method where the individual particles can be observed, measured and their shape determined [Shekunov *et al*. 2007]. As shown in Chapter 3, light microscopes are employed to analyze the particle size distribution of inclusions in silicon. They measure the equivalent diameter based on the projected area

of the particles. As mentioned previously, the main error in the measurement of the equivalent diameter is due to the shape of the particle which differs from that of a sphere. Fortunately, SiC particles found in top cut silicon scrap and in Solsilc are almost round in shape. Therefore, their shape does not introduce a significant error in the particle size analysis. On the other hand Si_3N_4 inclusions found in top-cut silicon scrap before filtration have a needle-like shape. The equivalent sphere theory applied in this case is problematic to use and the equivalent diameter does not properly reflect their size. Considering that about half of the inclusions in top-cut silicon scrap before filtration are Si_3N_4 particles, the error in the particle size analysis of inclusions in scrap is quite large. However, Si_3N_4 particles are removed successfully by filtration of silicon already with 30 ppi SiC filters. Hence, determination of their accurate size distribution does not seem to be of great importance in this study. Nevertheless, it should be noted that another technique must be developed to analyze needle-like particles if it is desirable to obtain correct data on their size distribution.

5.3 Filtration of silicon with ceramic foam filters

The results shown in Section 4.2.2.1 suggest that the size and shape of the Si_3N_4 particles favor cake-type formation on the top surface of the filters. Due to the small quantity of the filtered silicon, the cakes cover only small parts of the top surface. If greater amounts of top-cut silicon scrap were to be filtered, the presence of Si_3N_4 particles would finally lead to blockage of the filter and the filtration process would stop. Figure 5.8, for filtration of magnesium, shows in a (m, t/m) diagram the typical behavior of ceramic foam filters [Bakke, 1992]. m is the filtered mass and t is the time required for that mass to pass through the filter. In the beginning t/m is constant, until a certain critical mass is filtered. Then, a sudden change occurs on the t/m curve corresponding to start of the cake build up in the top surface of the filter [Bakke, 1992].

To attain satisfactory filtration if a high pressure drop is not possible, cakes should not develop, and the inclusions must be deposited within the filter. This deep bed filtration may be the only practical route to remove inclusions from molten silicon [Engh, 1992]. Thus, ideally, the Si_3N_4 particles should be removed in a previous separation stage. One way to prevent formation of cakes is to use sandwich type filters with a large

pore size on the top. Below a filter with smaller pores is required to remove the small inclusions.

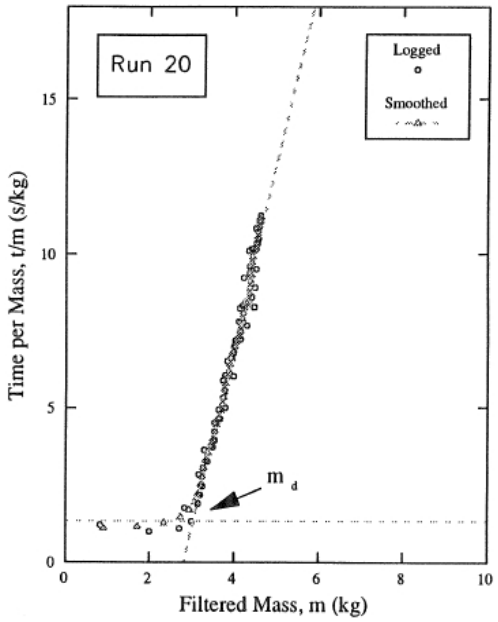

Figure 5.9: Inverse average flow as a function of filtered mass in filtration of magnesium with 20 ppi CFF [Bakke, 1992].

To describe removal of inclusions from ceramic foam filters we here focus only on the SiC particles. In this treatment it is assumed that SiC inclusions are spheres and that once they touch the wall of the filter, they adhere to it. A number balance over a differential depth of the filter gives (see Figure 5.10):

Flow of inclusions through the surface at position z = Flow of inclusions through the surface at position (z + Δz) + Number of inclusions transferred to the collector between z and (z + Δz) in unit time

or

$$c(z)Au\varepsilon = c(z+\Delta z)Au\varepsilon + k_t c a_s (A\Delta z)\varepsilon \qquad (5.7)$$

where c is the inclusion content in the melt per unit volume, u is the mean particle velocity in the z-direction, a_s is the surface area of collector per unit volume of melt, ε is the void fraction (porosity), A is the interfacial contact area, $A\Delta z$ is the control volume

and $A\Delta z\varepsilon$ is the melt volume. k_t is the coefficient for transfer of particles to the filter wall [Engh, 1992]. Equation (5.7) neglects collision of inclusions. The coefficient for transfer of particles to the filter wall, k_t, can be written:

$$k_t = \eta u b \tag{5.8}$$

where b is the ratio of the collector surface area projected in the z-direction to the total collector surface area and η gives the fraction of the particles moving towards the collector that are removed.

As already mentioned in Chapter 2, sedimentation (settling) and interception are the main mechanisms to affect inclusion transport to filter wall. For large particles settling is important. For small particles, settling will become negligible and interception will become the dominant factor.

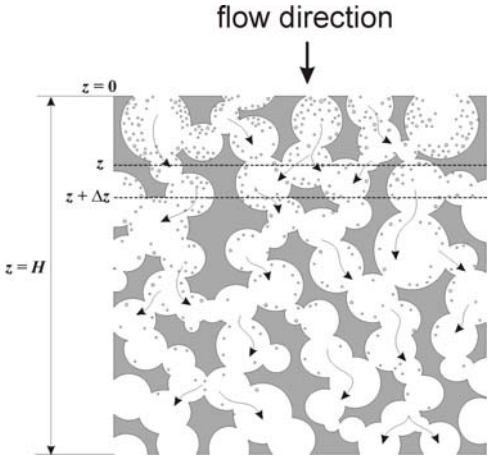

Figure 5.10: A differential slice (control volume) in a CFF filter.

Several researchers [Gauckler *et al*. 1985], [Conti & Netter, 1992], [Burganos *et al*. 1994], [Acosta *et al*. 1995], [Keegan *et al*. 1999], [Acosta *et al*. 2000a, 2000b] [Ni *et al*. 2006] approximated the geometry of the foam filter unit cell to that of two spherical pores overlapping each other (Figure 5.11). By considering the fluid flow inside these pores they attempted to predict the particle trajectory inside the filter and the sites where these particles are captured. Engh [1992], used the isolated sphere model to predict filtration efficiency for a filter made of a packed bed of spheres. Tien and his coworkers [Tien & Ramarao, 2007], used the constricted-tube model to describe deep bed filtration. Here we discuss all these models applying them to ceramic foam filters and

finally, develop a new model which should describe better the removal efficiency of foam filters.

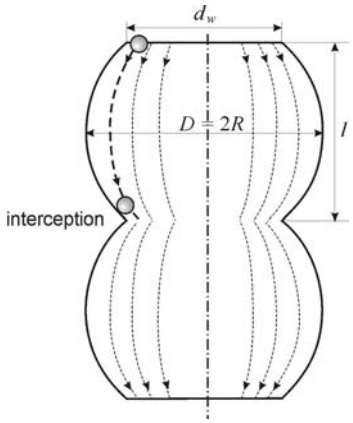

Figure 5.11: Schematic representation of unit cell for foam filters [Acosta *et al*. 1995].

Particle deposition by interception occurs because particles are finite in size. If all the forces acting on a particle in a fluid stream are negligible the particle will move along with the streamlines as shown in Figure 5.11. It is assumed that for the melt, any particle will be deposited that comes within one particle radius from the wall. Consequently, only those particles sufficiently close to the pore surface will be collected [Tien & Ramarao, 2007]. If we use the isolated sphere model (Figure 5.12) and assume potential flow, the collision efficiency for the interception mechanism [Engh, 1992] becomes:

$$\eta_i^E = \frac{3a}{R} \tag{5.9}$$

where a is the particle radius and R is the collector radius.

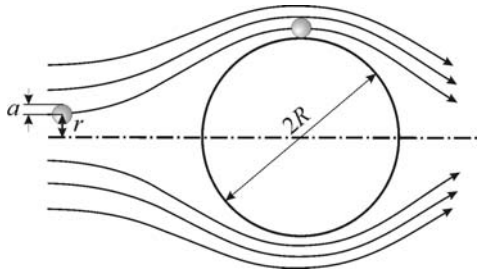

Figure 5.12: Model of interception mechanism used by Engh [1992] and Tien & Ramarao [2007] for the transfer of spherical particles to a spherical collector.

Tien & Ramarao [2007] for creeping flow suggest that the single-collector efficiency due to interception for the isolated sphere model is:

$$\eta_i^T = \frac{3}{2} N_R^2 \tag{5.10}$$

where $N_R = d_p/d_g$ (d_p is particle diameter = $2a$, d_g is grain (collector) diameter = $2R$.

Tien & Ramarao [2007] also used the constricted-tube model to represent filter media (Figure 5.13). The use of various geometries gives rise to different flow fields within the unit collector. This difference may be important in the application of the various geometries for the study of particle deposition in granular filters [Pendse & Tien, 1982]. In the original formulation of Payatakes *et al*. [1973a], the wall geometry of the constricted-tube is assumed to be parabolic. Fedkiew & Newman, [1977] proposed the sinusoidal geometry while Venkatesan & Rajagopalan, [1980] the hyperbolic geometry. Pendse & Tien [1982] estimated the flow field that corresponds to three different tube configurations and their results showed that for all three configurations the constricted-tube model give consistent values of η_i. Moreover, η_i is insensitive to minor variations of the flow field expressions [Pendse & Tien, 1982]. As a result, for creeping flow, the collector efficiency for this mechanism is:

$$\eta_i^P = N_R^2 \left(\frac{4}{d_c^{*2}} - \frac{4N_R}{d_c^{*3}} - \frac{N_R^2}{d_c^{*4}} \right) \tag{5.11}$$

where d_c is the constriction diameter as shown in Figure 5.13 and d_c^* is the dimensionless constriction diameter defined as $d_c/\langle d_g \rangle$ (or d_w/D) [Pendse & Tien, 1982], [Tien & Ramarao, 2007].

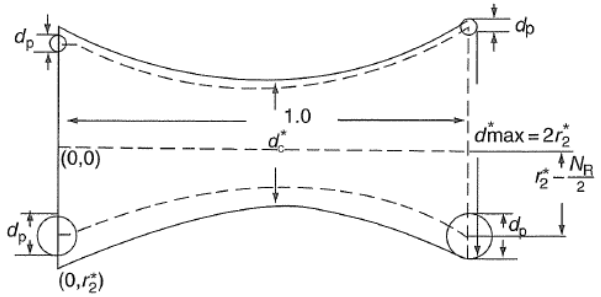

Figure 5.13: Schematic representation of the interception mechanism in the constricted-tube collector model [Tien & Ramarao, 2007].

The other collision mechanism that may be important is gravity. Since the particle density is different from that of the melt, inclusions will settle in the direction of the net gravitational force [Tien & Ramarao, 2007]. The settling velocity, given by Stokes' law, is already discussed in Section 5.1.1. For the isolated sphere model, the single-collector efficiency attributable to settling, η_s, is:

$$\eta_s = \frac{u_r \pi R^2}{\pi R^2 v} = \frac{u_r}{v} \tag{5.12}$$

where u_r is the settling velocity of particles as given in Equation (2.9), v is the relative velocity between the melt and collector [Engh, 1992], [Tien & Ramarao, 2007].

To estimate the velocity of the melt through the filter, v, we initially use the following equation valid for a tube with inner radius R:

$$v = \frac{Q}{\pi R^2} \tag{5.13}$$

where Q is the volume rate of flow given by Hagen-Poiseuille law [Bird *et al*. 2007]:

$$Q = \frac{\pi R^4 \Delta P_h}{8 \mu H} \tag{5.14}$$

Knowing that $\Delta P_h = \rho g \Delta h$ and using Equation (2.20) for the pressure head, Δh, required to fill a pore with diameter D, we get the expression for the relative velocity, v:

$$v = \frac{R^2 \Delta P_h}{8 \mu H} = \frac{R^2}{8 \mu H} \frac{4 \sigma^{lg} \cos\theta}{\rho_l g D} \rho_l g = \frac{1}{4} \frac{R \sigma^{lg} \cos\theta}{\mu H} \tag{5.15}$$

where μ and H are the viscosity of molten silicon and filter depth respectively. Using the data given in Table 5.12 for the calculations of the velocity of molten silicon through the 30 ppi SiC ceramic foam filter we get v = 8.67 m s^{-1}. The viscosity value given in Table 5.12 is the average of the values reported in the literature by Sato *et al*. [2003], Sasaki *et al*. [1995], Zhou *et al*. [2003] and Rhim & Ohsaka [2000].

Table 5.12: The parameters used in calculations for filtration of molten silicon with 30ppi SiC ceramic foam filter.

Parameter	Value
Mean filter pore diameter, $D = 2R$, (d_g, d_{max})	0.00206 [m]*
Mean filter window diameter, d_w, (d_c)	0.00093 [m]*
Mean filter branch diameter, d_b ($\frac{1}{10}$ of D)	0.00020 [m]
Mean pore height, l	0.00184 [m]
Filter depth, H	0.026 [m]
Porosity of 30 ppi CFF, ε	0.88*
Surface tension of molten Si, σ^{lg}	0.80 [J m^{-2}]
Wetting angle of $Si_{(l)}$ in $SiC_{(s)}$, θ ($\cos\theta$)	38° (0.79)
Density of molten Si at m.p.	2570 [kg m^{-3}]
Viscosity of molten Si at m.p., μ	7.0×10^{-4} [kg m^{-1} s^{-1}]

* Data taken from Acosta *et al*. [1995].

The velocity calculated by Equation (5.15) is valid only for a straight round tube. The friction factor, *f*, for flow in conduits is [Bird *et al*. 2007]:

$$f = \frac{1}{4}\left(\frac{D}{H}\right)\left(\frac{\Delta P_h}{\frac{1}{2}\rho_l v^2}\right) \tag{5.16}$$

The velocity then can be written:

$$v = \left(\frac{1}{2}\frac{D}{H}\frac{\Delta P_h}{\rho_l f}\right)^{1/2} \tag{5.17}$$

The Reynolds Number (Re) for our system is equal to 6.6×10^4 if we use v = 8.7 m s^{-1} (Re = $Dv\rho_l/\mu$). For this value the friction factor is equal to 0.008 [Bird *et al*. 2007]. Using this value for friction factor in Equation (5.17) the melt velocity through the filter becomes equal to 1.53 m s^{-1}. For our calculations we use the melt velocity value of 1.5 m s^{-1}. The high value of melt velocity through the filter can be explained by the capillary force. This force is basically described by two parameters: the radius of the capillary (pore in our case) and the interfacial surface energies of the solid-liquid-gas interface. The last parameter is characterized by the contact angle of molten silicon with filter material. The contact angle value for Si-SiC system is 40° indicating good wetting

(see Section 5.5). Therefore, it is good wetting of molten silicon with SiC filters that enables the melt to run fast through the filter. However, a better way to calculate the melt velocity through a ceramic foam filter should be found.

Table 5.13 gives calculated data on the collision efficiencies for interception and sedimentation mechanisms for various particle sizes. This is carried out in order to estimate the relative importance of each mechanism on removal of inclusions.

Table 5.13: Calculated data of η_i^E , η_i^T , η_i^P , and η_s for various particle sizes.

d **[m]**	η_i^E	η_i^T	η_i^P	η_s
1×10^{-6} (1 μm)	1.5×10^{-3}	3.5×10^{-7}	4.6×10^{-6}	3.0×10^{-7}
5×10^{-6} (5 μm)	7.5×10^{-3}	8.8×10^{-6}	1.2×10^{-4}	7.6×10^{-6}
1×10^{-5} (10 μm)	1.5×10^{-2}	3.5×10^{-5}	4.6×10^{-4}	3.0×10^{-5}
2×10^{-5} (20 μm)	3.0×10^{-2}	1.4×10^{-4}	1.8×10^{-3}	1.2×10^{-4}
3×10^{-5} (30 μm)	4.5×10^{-2}	3.2×10^{-4}	4.1×10^{-3}	2.8×10^{-4}
5×10^{-5} (50 μm)	7.5×10^{-2}	8.8×10^{-4}	1.1×10^{-2}	7.6×10^{-4}
1×10^{-4} (100 μm)	1.5×10^{-1}	3.5×10^{-3}	4.1×10^{-2}	3.1×10^{-3}

The settling velocity of SiC particles is much smaller than the melt velocity through the filter. This is the reason why the collision probability due to settling has small values. Nevertheless, Table 5.13 shows that removal due to settling is comparable to the collision probability due to interception for the isolated sphere model with creeping flow. Therefore, removal probability by settling has to be considered. Taking into account both mechanisms and assuming that they are independent of each other, the total collision probability, η, can be written:

$$\eta = \eta_i + \eta_s \tag{5.18}$$

Inserting Equation (5.8) into Equation (5.7) and for $\Delta z \to 0$ we obtain:

$$0 = \frac{\mathrm{d}c}{\mathrm{d}z} + \eta a_s b c \tag{5.19}$$

which is a first order homogeneous differential equation. After integration over the filter depth *H* we get:

$$\frac{c}{c_{in}} = \exp(-\eta a_s b H) \tag{5.20}$$

This gives the filtration efficiency [Engh, 1992]:

$$E = 1 - \frac{c}{c_{in}} = 1 - \exp(-\eta a_s b H) \tag{5.21}$$

So far, there are three models described based on the constricted-tube configuration and on the isolated sphere collector. The last one is used for the cases of two different flow regimes, potential flow [Engh, 1992] and creeping flow [Tien & Ramarao, 2007]. Based on Equation (5.21) the filtration efficiency that results from each of these cases is discussed separately in the following paragraphs.

For the isolated sphere model the void fraction is ε and the collector diameter is 2*R*. Hence, the specific surface area is [Engh, 1992]:

$$a_s = \frac{3(1-\varepsilon)}{R\varepsilon} \tag{5.22}$$

Finally, introducing the total removal probability for the isolated sphere model with potential flow, $\eta_{\text{sphere}}^{\text{pot. flow}}$, and knowing that for spheres b = ¼ we obtain:

$$E_{\text{sphere}}^{\text{pot. flow}} = 1 - \exp\left[-\frac{3}{4}\left(\frac{3a}{R} + \frac{u_r}{v} \right) \frac{(1-\varepsilon)}{R\varepsilon} H \right] \tag{5.23}$$

For the isolated sphere model with creeping flow the removal efficiency, $E_{sphere}^{creep.\ flow}$, becomes:

$$E_{\text{sphere}}^{\text{creep. flow}} = 1 - \exp\left[-\frac{3}{4}\left(\frac{3N_R^2}{2} + \frac{u_r}{v} \right) \frac{(1-\varepsilon)}{R\varepsilon} H \right] \tag{5.24}$$

The product $a_s b$ can be written:

$$a_s b = \frac{\text{Surface area of collector}}{\text{Volume of melt}} \times \frac{\text{Surface area in direction of flow}}{\text{Surface area of collector}} \Rightarrow$$

$$a_s b = \frac{\text{Surface area of collector}}{\text{Volume of collector}} \times \frac{\text{Volume of collector}}{\text{Volume of melt}} \times \frac{\text{Surface area in flow direction}}{\text{Surface area of collector}} \tag{5.25}$$

For the constricted-tube model where the unit cell is a one-sheeted hyperboloid the volume of collector is (see Figure 5.13):

$$V_h = \frac{1}{3}\pi l(\frac{d_c^2}{2} + \frac{d_{\max}^2}{4}) \tag{5.26}$$

where l is the pore height and the porosity can be written:

$$\varepsilon = \frac{\text{Volume of melt}}{\text{Volume of melt + Volume of collector}} \tag{5.27}$$

which then gives:

$$\frac{\text{Volume of collector}}{\text{Volume of melt}} = \frac{1-\varepsilon}{\varepsilon} \tag{5.28}$$

After calculating the surface area in flow direction and replacing Equations (5.26) and (5.28) in Equation (5.25) we have:

$$a_s b = \frac{\frac{\pi}{4}(d_{\max}^2 - d_c^2)}{\frac{1}{3}\pi l\left(\frac{d_c^2}{4} + \frac{d_{\max}^2}{2}\right)} \times \frac{1-\varepsilon}{\varepsilon}$$

or:
$$a_s b = \frac{3}{2}\frac{(d_{\max}^2 - d_c^2)}{\left(\frac{d_c^2}{2} + d_{\max}^2\right)l} \times \frac{1-\varepsilon}{\varepsilon} \tag{5.29}$$

Now we can write the expression for filtration efficiency for this model:

$$E_{cons-tube} = 1 - \exp\left[-\frac{3}{2}\left(\frac{4N_R^2}{d_c^{*2}} - \frac{4N_R^3}{d_c^{*3}} - \frac{N_R^4}{d_c^{*4}} + \frac{u_r}{v}\right)\frac{(d_{\max}^2 - d_c^2)}{\left(\frac{d_c^2}{2} + d_{\max}^2\right)}\frac{(1-\varepsilon)}{l\varepsilon}H\right] \tag{5.30}$$

The parameters used in the three models described above are employed for the 30 ppi ceramic foam filter. Thus, d_{max} is equal to D, d_c is equal to d_w and l is the pore height = $\sqrt{D^2 - d_w^2}$ (see Figure 5.11 and 5.13). Table 5.12 summarizes the parameters used in the calculations for the filtration efficiencies.

In the models described above the collectors of the particles are considered as spheres and tubes. However, ceramic foam filters, as seen in Figure 5.14, do not consist of spheres, tubes or empty pores as depicted in Figure 5.11. Looking closely at the structure of the filter it seems to be reasonable to assume that the filter consists of many small branches that form a network. These branches, which collect the particles, are

considered as cylinders. For a cylinder with diameter d_b (= $2R_b$) and height L the stream function for potential flow is [Bird *et al*. 2007]:

$$\psi(r,\theta) = v_\infty \sin\theta\left(r - \frac{R_b^2}{r}\right) \tag{5.31}$$

where v_∞ is the approach velocity of flow, r is the distance from the axis and θ is the polar angle. The curves ψ = constant are streamlines and for $r = R_b$, $\psi = 0$. The flow of liquid towards the cylinder is $2L\psi$. Particles with radius a will collide with the branch if they lie within a distance $r = R_b + a$. The volume flow approaching the branch is $2v_\infty R_b L$. Thus, the collision probability due to interception, η_i^b, is:

$$\eta_i^b = \frac{2L\psi}{2v_\infty R_b L} = \frac{2Lv_\infty \sin\theta}{2v_\infty R_b L}\left(R_b + a - \frac{R_b^2}{R_b + a}\right) \approx \frac{2a}{R_b}\sin\theta \tag{5.32}$$

For $\theta = \pi/2 \rightarrow \sin\theta = 1$, thus:

$$\eta_i^b = \frac{2a}{R_b} \tag{5.33}$$

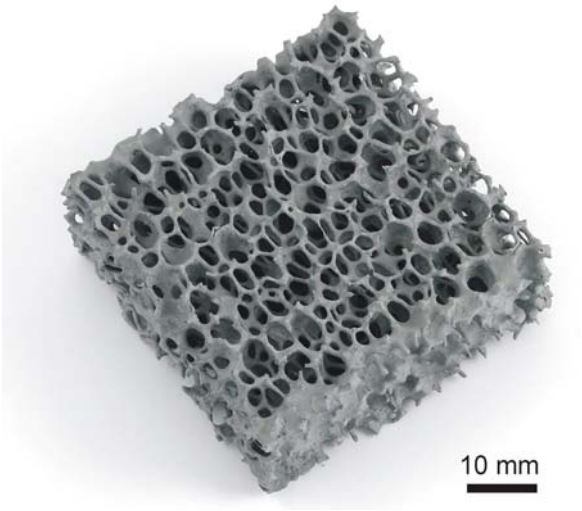

Figure 5.14: View of a SiC ceramic foam filter used in filtration experiments (photo M. Gaal).

According to Equation (5.25), the product $a_s b$ can be written:

$$a_s b = \frac{2R_b L}{\pi R_b^2 L} \times \frac{1-\varepsilon}{\varepsilon} = \frac{2(1-\varepsilon)}{\pi R_b \varepsilon} \tag{5.34}$$

Finally, Equation (5.21) for this model becomes:

$$E_b = 1 - \exp\left(-\frac{4a(1-\varepsilon)}{\pi R_b^2 \varepsilon} H\right) \tag{5.35}$$

This time we do not need to consider the collision probability due to gravity as it is much smaller than the interception.

All the four models are plotted in Figure 5.15 as filtration efficiency *versus* particle size together with experimental results. The experimental data are given in Table 5.14 and give the number size distribution of inclusions before and after filtration with the 30 ppi SiC filter. Analysis of all the samples after filtration showed a very high content of particles smaller than 10 μm. By comparing it with that in silicon before filtration we conclude that these particles are secondary inclusions created during filtration experiments. Therefore the results for particles smaller than 10 μm are not plotted in the graph. As the Figure 5.15 shows, filtration efficiency given by Equation (5.35) agrees reasonably well with the experimental results for particle sizes larger 2.5×10^{-5} m (25 μm). Engh [2009] argues that the model may be optimistic because it considers the branches as lying perpendicular to the melt flow. Also the effect of the boundary layer is neglected. A boundary layer reduces the filtration efficiency.

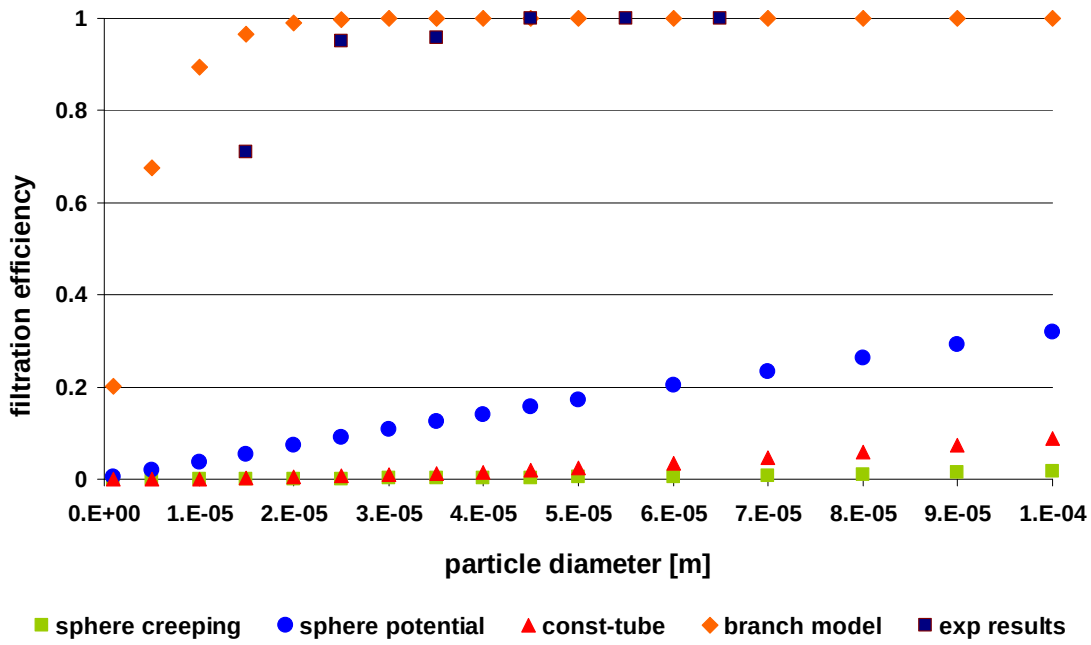

Figure 5.15: Curves of filtration efficiencies versus particle size for various models and experimental results.

Table 5.14: Particle size distribution of inclusions before and after filtration with 30ppi SiC filter in 1 cm^2 surface area.

***d* [m] (range/μm)**	**Before Filtration**	**Exp.13**	**Exp.14**	**Exp.15**	**Exp.16**	**Mean after fil.**	**Efficiency**
5×10^{-6} (0 – 10)	41	227	314	-	-	-	-
1.5×10^{-5} (10 – 20)	43	1	37	5	7	12.5	0.71
2.5×10^{-5} (20 - 30)	26	0	0	0	5	1.25	0.95
3.5×10^{-5} (30 – 40)	12	0	0	0	2	0.5	0.96
4.5×10^{-5} (40 – 50)	4	0	0	0	0	0	1.00
5.5×10^{-5} (50 – 60)	5	0	0	0	0	0	1.00
6.5×10^{-5} (60 – 70)	4	0	0	0	0	0	1.00

A problem with this model is that it does not consider the presence of a boundary layer on the cylinder walls. This layer is formed because the fluid in contact with the filter walls must have zero velocity. Removal efficiency will depend on the thickness of the boundary layer. For a cylinder of radius R_b the boundary layer thickness as given by Faber [1995] is:

$$\delta^2(\chi) \approx 11.6 \frac{R_b^2}{\mathrm{Re}} X(\chi) \tag{5.36}$$

where Re is the Reynolds Number (= $2\rho_l R_b v/\mu$) and where

$$X(\chi) = \frac{\left(\frac{8}{15} - \cos\chi + \frac{2}{3}\cos^3\chi - \frac{1}{5}\cos^5\chi\right)}{\sin^6\chi} \tag{5.37}$$

χ is the polar angle ($0 < \chi < \pi$). At $\chi = 0$ the boundary layer is zero and for small χ it is independent of χ. Figure 5.16 gives an idea of the boundary layer behavior. Beyond χ = 115° its value is scarcely relevant because, normally before χ reaches 115°, the boundary layer is found in practice to separate from the cylinder. Since interception is maximum at the equator ($\chi = \pi/2$) in potential flow, it is important to know the boundary layer thickness here. Taking $R_b = 1 \times 10^{-4}$ m ($\frac{1}{10}$ of the pore radius), χ = 90° and for Re = 1112, the boundary layer thickness is $\delta = 7.5 \times 10^{-6}$ m (7.5 μm). Therefore,

the removal efficiency for particles smaller than 7.5 μm is smaller than what our model predicts.

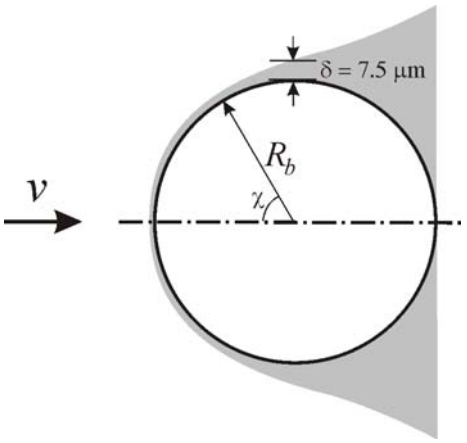

Figure 5.16: The boundary layer (lighted shaded area) with a thickness δ described by Eq. (5.36) for flow past a cylinder with radius R_b.

5.4 Contamination of silicon from the crucible and the filter

The graphite crucible used in filtration may be a source of contamination of silicon. Solid particles and various elements such as Al, Fe and C may enter the liquid silicon during the filtration process creating inclusions and contaminating the silicon (see Figure 5.17). Pure graphite particles have been found inside the matrix of the silicon indicating that molten silicon has torn off graphite particles from the crucible. The content of several elements before and after filtration is shown in Figure 5.18 and Table 5.15. The SiC filters used in the study contains 85% SiC with the rest being a binder mainly composed of Al_2O_3. Thus, contamination from the filter may occur and alumina particles may find their way to the filtered silicon.

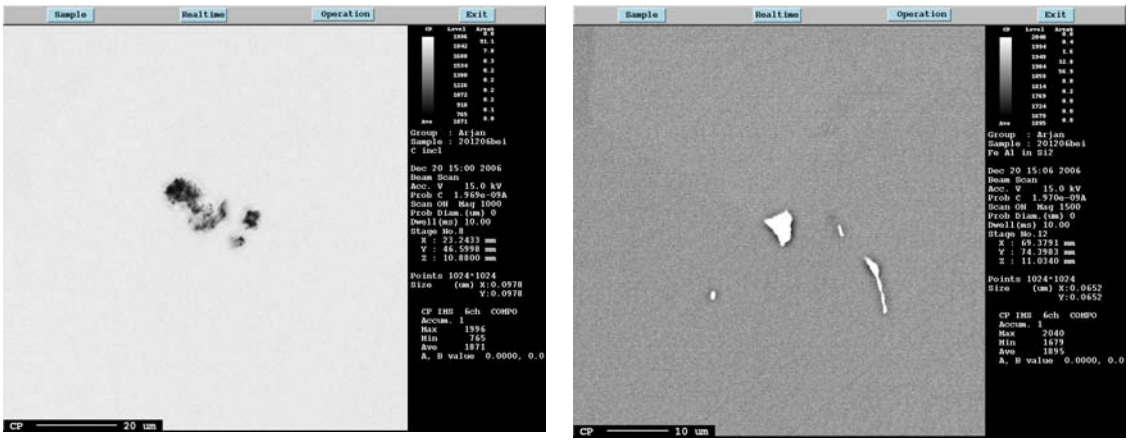

a) b)

Figure 5.17: Inclusions inside the filtered silicon. (a) Carbon inclusion; (b) Fe and Al.

Table 5.15: Impurities in silicon scrap before and after filtration with various filters (GDMS analysis).

Element [mass ppm]	Before filtration	C filter 10ppi	SiC filter 10ppi	SiC filter 20ppi	SiC filter 30ppi
P	0.089	5.042	0.356	0.449	0.540
Ca	0.842	45.115	0.114	0.602	12.356
Ti	0.018	-	0.009	0.090	0.616
Fe	0.267	2.094	0.273	1.328	27.037
Zr	-	2.021	0.003	0.005	0.032
Mg	0.007	10.078	0.029	0.165	0.850
Al	1.244	168.431	0.468	14.267	38.874

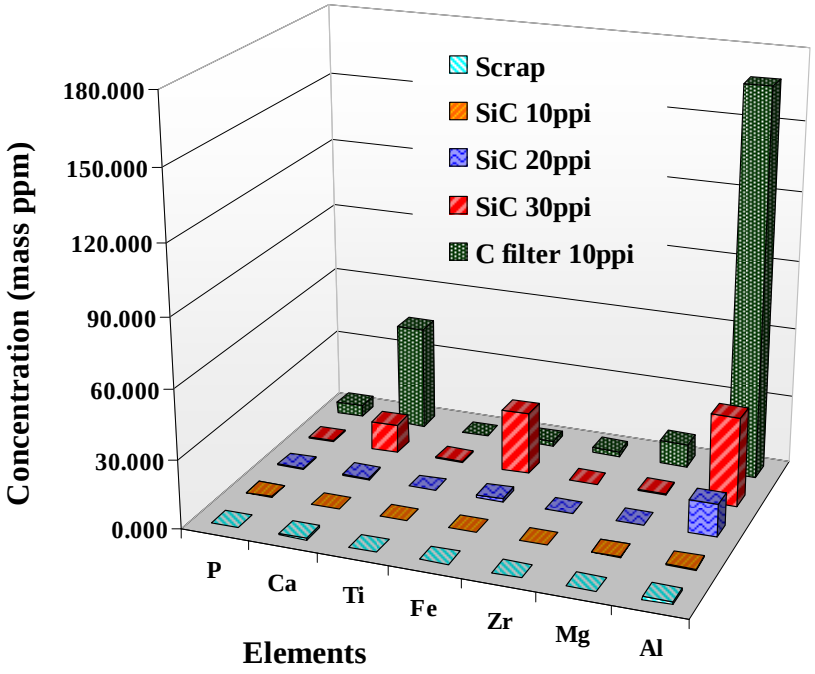

Figure 5.18: Plot of impurity data given in Table 5.16.

To study the contamination of silicon from the graphite crucible and the filter, pure poly-crystalline silicon was filtered with a 30 ppi SiC filter. GDMS results are given in Table 5.16.

Table 5.16: Impurity content in poly-crystalline silicon before and after filtration with 30ppi SiC filter (GDMS analysis).

Element [mass ppm]	Before filtration	After fil. 10ppi SiC
P	0.025	0.531
Ca	0.213	0.229
Ti	0.002	0.014
Fe	0.004	0.830
Zr	0.000	0.006
Mg	0.016	0.030
Al	0.148	2.359

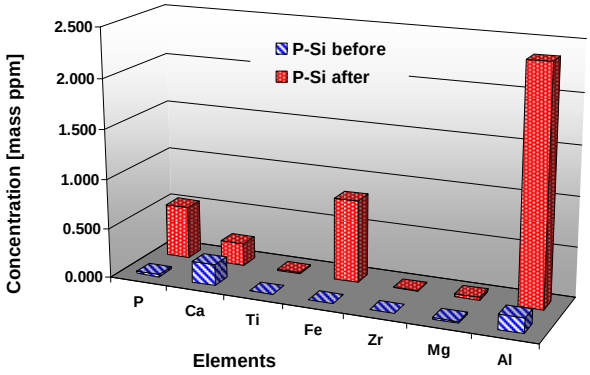

As can be seen from Figure 5.17, carbon filters introduce more impurities in silicon than SiC filters. Contamination in silicon increases with increasing ppi number (or decreasing filter pore size). This is due to the fact that residence time of silicon in the filter increases with decreasing filter pore size. Therefore, impurities have more time to diffuse into molten silicon.

The number of inclusions in silicon after filtration is more than in silicon scrap before filtration (see Table 4.6). Almost 75% of these inclusions are SiC particles within the size range 0 - 5 μm. This leads to conclusion that molten silicon, in contact with the graphite crucible is saturated with carbon. According to Dalaker & Tangstad [2008], saturation of silicon with carbon is very fast, about 1 min. The dissolved carbon, after cooling down of silicon, has precipitated as small SiC particles. This is confirmed from filtration with the pure poly-crystalline silicon since large numbers of SiC particles within that range are found after filtration of poly-crystalline silicon (see Figure 5.17). Silicon samples after filtration are analyzed by LECO for the total carbon content. Results are given in Table 5.17. Assuming that all the SiC particles in top-cut silicon scrap are removed, then the total carbon content measured in silicon after filtration is the carbon dissolved in molten silicon at 1414 - 1450°C. This is another way of measuring solubility of carbon in silicon. Taking the average value from all experiments, carbon solubility in top-cut scrap silicon scrap at 1414ºC – 1450°C is about 100 mass ppm according to this approach.

Table 5.17: Total carbon content in silicon after filtration (LECO-Analyzer).

	Exp.6 10ppi	**Exp.7 10ppi**	**Exp.8 10ppi**	**Exp.9 20 ppi**	**Exp.15 30ppi**	**Exp.16 30ppi**
C [mass ppm]	82 /83 /106	97 /98 /86	78 /102 /92	93 /76 /97	160 /99 /92	105 /98 /105
Average	90	94	91	89	150	103
STDV	14	7	12	11	47	4

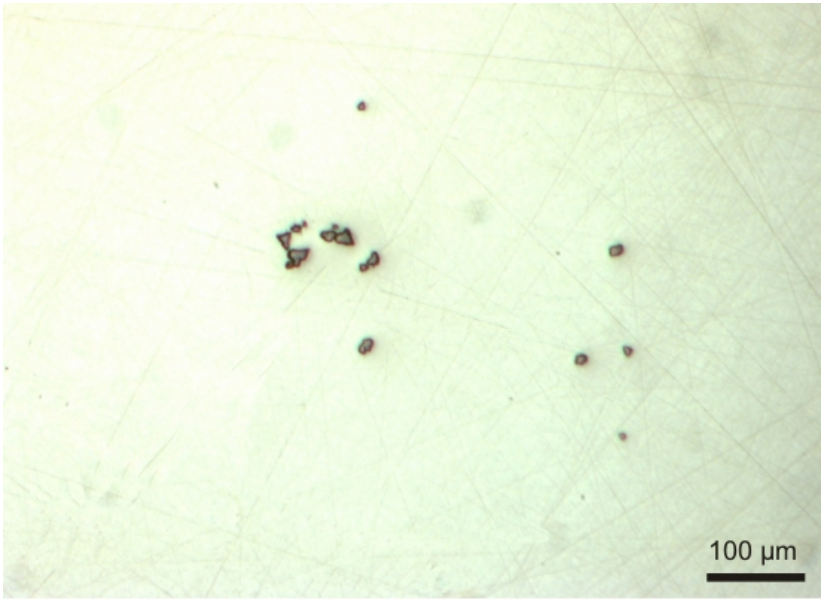

Figure 5.17: Secondary SiC particles in pure poly-crystalline silicon after filtration with a 30 ppi SiC filter.

5.5 Wetting and infiltration of silicon in graphite materials

As mentioned in the previous section, wetting of silicon with filter material is important for the filtration process. Good wetting of filters by molten metal lowers, removes or gives a negative pressure head and increases the adhesion of the inclusions with the filter walls.

Wettability of silicon with refractories is another important factor that has to be considered in metallurgical refining of silicon. The materials most frequently used to date in contact with molten silicon are fused silica (commonly referred to as quartz) and various carbons and graphites. The carbon and graphite is usually chosen because of ease of machining, high temperature stability and moderate ease of purification. During the preliminary filtration experiments, noted as NF1 to NF9 in Chapter 4, it was hard to collect the filtered silicon in the copper bowl. Due to very good wetting of silicon with the graphite, after flowing through the hole at the bottom of the crucible, the silicon did not fall straight to the copper bowl. Instead, it leaked at the bottom surface of the crucible and dripped outside afterwards. Dalaker [2008] have reported similar problems due to good wettability of silicon with graphite materials. In his experiments, the molten

silicon reached to the top of the crucible and dripped outside. In spite of these technical problems, the main issue is the contamination of silicon by graphite materials.

Molten silicon is very corrosive, even to the point of being labeled a “universal solvent”. A major problem with molten silicon contact materials is dissolution, which results in detrimental levels of impurity contamination of the silicon and reaction to form silicides. In order to avoid severe contamination, ideally inert refractories that are not wetted by silicon should be used. However, in the absence of such materials, one should try to minimize wetting and infiltration of molten silicon into the refractories. Graphite crucibles are commonly used in silicon industry. As shown in Section 4.2.3 wetting and infiltration of silicon depend on the physical properties of materials and on their surface finish. Here we discuss the results with the aim to gain more information on wetting, spreading and infiltration of molten silicon on the graphite substrates.

The system C-Si is a reactive one [Dezellus *et al*. 2005], [Eustathopoulos, 1998]. Initially molten silicon does not wet carbon materials. The initial contact angles measured in this study are approximately 120º as shown in Section 4.23. Several researchers have reported even higher contact angles (~ 146º) [Dezellus *et al*. 2005], [Li & Hausner, 1996]. As soon as silicon melts, it starts to react with C to form β-SiC. The contact angles decline with time and spreading of silicon on the graphite surface occurs. In the end, a final value of wetting angle is reached often called equilibrium value. Eustathopoulos [1998] claims that for reactive systems the Young’s equation for contact angle can be written:

$$\cos\theta_F = \cos\theta_P = \frac{\gamma^{\mathrm{Pg}} - \gamma^{\mathrm{Pl}}}{\sigma^{\mathrm{lg}}} \tag{5.31}$$

where θ_F is the final contact angle, θ_P is the contact angle of the reaction product, σ^{lg} is the surface tension of liquid silicon, γ^{Pg} is the surface energy between the reaction product (solid state) and gas phase, γ^{Pl} is the surface energy between reaction product (solid state) and liquid phase [Landry *et al*. 1997]. An example of an analogous to C-Si system is CuSi alloy on vitreous carbon [Landry *et al*. 1996]. Pure copper does not wet vitreous carbon (at 1150°, θ = 137°), but a Cu – 40at.% Si alloy wets this surface very well due to the formation of a continuous, submicron layer of SiC at the interface. In the experiments with glassy (vitreous) carbon as substrate, the final contact angles are

reported to be between 30 - 50° [Li & Hausner, 1996], [Whalen & Anderson, 1975], [Dezellus *et al*. 2005]. These values agree with the contact angles of Si-βSiC system. For Si-βSiC system the reported contact angles are around 40°.

For graphite materials (monocrystal, pyrolitic graphite, or polycrystalline graphite), the equilibrium contact angle value should be the same as in the case of glassy carbon because it is characteristic of the liquid silicon on SiC reaction product layer. However, most studies in the literature performed with carbon materials report equilibrium contact angles of between 5° and 35° [Li & Hausner, 1995, 1996], Dezellus *et al*. 2005]. Our experimental values of θ_F are in agreement with the reported values in the literature. The contact angle values obtained for the graphites studied can be explained by:

- the average roughness R_a of the substrates that ranges from 0.06 μm to 1.5 μm. High values of θ_F are reported for low R_a. Li & Hausner [1995] reported a contact angle value of about 30° for R_a = 0.005 μm. For the graphite ISO88 and for a surface roughness of R_a = 0.06 μm, this value is 31º. Dezellus *et al*. [2005] have reported a value of θ = 35º for R_a = 0.005 μm.
- as seen in the results (Section 4.2.3) and reported in the literature [Li & Hausner, 1995, 1996], [Zhou & Singh, 1995], [Deike & Schwerdtfeger, 1995], [Dezellus *et al*. 2005] liquid silicon infiltrates the substrates thereby decreasing the volume of liquid silicon remaining above the surface. Therefore, in this case, receding rather than advancing contact angles are measured.

Graphite materials are characterized by high porosity. Liquid silicon penetrates into the graphite and reacts to form silicon carbide in the pores. Li & Hausner [1995] argue that the open porosity is the main difference between graphites. According to them, this difference is reflected in the depths of penetration which is ~1000 μm in a graphite with 11% porosity and ~200 μm in a graphite with 8% porosity. Results here show that even in graphite with high porosity, such as ISO88 (porosity = 12.1%) infiltration depth is relatively low, about 350 μm. Leipold *et al*. [1980] suggests that it is necessary to use polycrystalline graphite with a density greater than 1750 kg m^{-3} to prevent infiltration of the silicon into the graphite pores. Results here indicate no clear

dependence of substrate density with infiltration depth. Infiltration happens to occur also for substrate IG11 which has a density of 1742 kg m^{-3}. The main factor that seems to affect infiltration depth of silicon in graphite materials is the average pore size (see Figure 4.35). For the graphites with both high average pore size and high values of R_a, final contact angles $\theta_F = 0$ are measured. In these cases, all the silicon on top of the substrate penetrated into the graphite material.

Singh & Behrendt [1992] argue that the infiltration depth depends not only on the physical properties of the graphite materials but also on the wetting behavior of the molten silicon. Since the surface roughness is the main actor that affects the wettability of the molten silicon on carbon materials, then, one would expect it to affect the infiltration depth too. The graphs in Figure 4.38 show the variation of the infiltration depth with the surface roughness. For the graphite SIC6, it is clear that the infiltration depth increases with increasing surface roughness. Results published by Li & Hausner [1995] (see Figure 2.21) show that the infiltration depth does not depend on the final contact angle.

At the interface between the graphite and the silicon the formation of the silicon carbide crystals began immediately after melting the silicon. For short reaction times, up to 20 min, the silicon carbide crystals grow nonuniformly in the form of islands. The silicon carbide formed in contact with graphite is present in two different morphologies [Deike & Schwerdtfeger, 1995].

- One form exists at the interface with graphite and within the pores of the graphite. The silicon carbide particles are very fine and intimately associated with silicon.
- The other form is found at the interface with the liquid silicon. Here, compact and large silicon carbide crystals are formed. Individual crystals may reach far into the silicon, or may even seem to be free, being surrounded completely by the silicon phase. Often, there are spaces between neighboring crystals filled with silicon [Deike & Schwerdtfeger, 1995].

Observations of the substrates after wetting experiments agree well with the reported results. Figure 4.41-b shows the morphology of the reaction formed SiC layer.

A full understanding of the reaction kinetics and mechanisms is important. However, there are only a few published data on the reaction kinetics, and the mechanisms are still far from being well understood. Fitzer & Gadow [1983] proposed a diffusion mechanism and derived a mathematical model to describe the rate of growth of SiC, which was based on the various mass transfer processes, such as mass transfer through the boundary layer in molten silicon, diffusion across the solid SiC layer, and reaction at the SiC/Si interface.

Spreading of silicon droplets on the carbon surface is reported by several authors [Eustathopoulos, 1998], [Eustathopoulos *et al*, 1999], [Dezellus *et al*. 2005]. For the Si-C system, chemical kinetics at the triple line should be rate-limiting because diffusion within the droplet is comparatively rapid [Eustathopoulos *et al*, 1999]. If the reaction does not change the global drop composition significantly so that the environment of the triple line is constant with time and if steady-state is established at the triple line during wetting, then the rate of reaction $U(\theta)$ and hence the triple line velocity are constant with time [Landry *et al*. 1996], [Dezellus *et al*. 1998]. This appears to be the case for the Si-C system [Dezellus *et al*. 1998], [Dezellus *et al*. 2005]. According to Dezellus *et al*. [2005] the spreading rate varies roughly as the cosine of the instantaneous contact angle with opposite sign:

$$\frac{U}{F(\theta)} = k_w \left(\frac{3V}{\pi} \right)^{\frac{1}{3}} \cdot (\cos\theta_F - \cos\theta) \qquad (5.32)$$

where $F(\theta)$ is a function of θ and k_w a kinetic constant related to the process of carbon atom transfer occurring at the C/Si interface. Figure 518 gives two experiments for the spreading rate U divided by $F(\theta)$ *versus* the cosine of the contact angle for liquid silicon on glassy carbon at 1430°C.

The data agree with the linearity of predictions of Equation (5.32) in a wide range of contact angles from $\theta \sim 102°$ to 50°. Extrapolating to zero spreading rate gives a θ_F around 30°, which is in good agreement with the equilibrium contact angle values measured for molten silicon on SiC. For graphite substrates this graphic representation cannot be made because of the roughness effect and liquid infiltration.

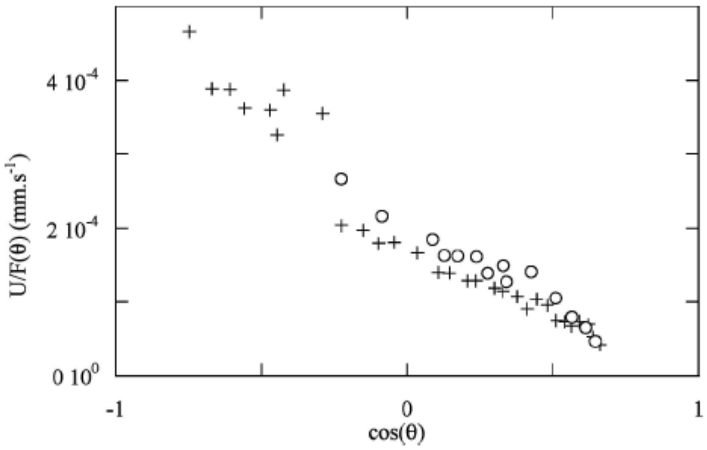

Figure 5.18: Experimental results of spreading rate $U(\theta)$ divided by the function $F(\theta)$ *versus* the cosine of contact angle for two experiments performed with liquid silicon on glassy carbon at 1430°C under vacuum [Dezellus, 2005].

Zhou & Singh [1995] placed emphasis on investigation of the reaction kinetics and mechanisms in the Si-C reaction over a temperature range of 1430° to 1510°C. They studied the reaction kinetics of liquid silicon with solid carbon using a variety of carbon materials including polycrystalline graphite and glassy carbon. Reaction of liquid Si with polycrystalline graphite showed that liquid silicon physically penetrated into the pores of the graphite and reacted with the graphite. Once the surface pores of the graphite were closed upon the formation of SiC, the penetration of liquid silicon stopped, but the reaction carried on to make this layer grow due to the diffusion of reactants through the reaction-formed SiC barrier layer. Obviously, two independent processes of infiltration and reaction were involved in this reaction. In practice, however, these two processes were not separable at the temperature of this study, which made it impossible to study only the kinetics of the Si-C reaction. Therefore, the graphite materials make it difficult to study the reaction kinetics [Eustathopoulos, 1998], Dezellus *et al*. [2005].

Glassy carbon plates, with a density of 1420 kg m^{-3}, were used by Zhou & Singh [1995] as a carbon source for a kinetics study of reaction with pure Si melt. The variation in the thickness of the reaction-formed SiC layer with exposure time is used as a measure of the reaction kinetics. The continuous solid SiC layer formed on the carbon surface prevents the molten silicon from directly contacting carbon. Therefore, either

silicon or carbon has to diffuse through the SiC layer to sustain the reaction. Since the reaction of carbon with the silicon melt proceeds extremely fast compared to the diffusion in solid, the diffusion of the silicon and/or the carbon is considered to be the rate-limiting step for the whole process. The growth rate of the continuous SiC layer seems to obey a $\frac{1}{4}$-power rate law for the reaction of glassy carbon with a pure Si melt. The $\frac{1}{4}$-power rate law can be expressed as:

$$\delta = kt^{1/4}$$

where δ is the average thickness of the continuous SiC layer, t is the reaction time, and k is a constant [Zhou & Singh, 1995]. In the temperature range of 1430° to 1510°C, k is almost always equal to 3 for the Si-C system, which indicates that the temperature has little influence on the reaction kinetics [Pampuch *et al*. 1986].

Chapter 6

CONCLUSIONS

The goal of this study was to gain a deeper understanding of the removal of inclusions from silicon. One aim was to allow metallurgical silicon to be refined to feedstock for photovoltaics. Then, two different processes were considered: removal of SiC by settling followed by directional solidification, and removal of SiC and Si_3N_4 particles by filtration with ceramic foam filters. Wetting was studied due to its importance for filtration and in the use of graphite refractories in the PV industry.

Removal of SiC inclusions by settling; effect of pushing and engulfment

Settling is an effective way to remove SiC inclusions from molten silicon. The number of inclusions in the middle of the ingots was less than in the bottom and top. A light microscopic study showed a removal efficiency of above 96% in the middle part of an ingot. The difference in density between the particles and the melt gives the SiC particles a relatively high settling velocity leading to a high removal efficiency.

Directional solidification of silicon pushes the particles to the top of the ingot. Even though the calculated critical velocity for engulfment of SiC particles in silicon is higher than the SL interface velocity, some engulfment of the large particles takes place. This may explain the presence of SiC particles in the middle of the ingot. Small SiC

precipitates that form during and after solidification (secondary inclusions) were found in the ingots.

Accumulation of impurities and solid particles ahead of SL interface will increase the chances for engulfment and may even cause breakage of the interface. In this case SiC particles could be entrapped between two solidification fronts. Therefore, both engulfment and entrapment may occur leading to a high content of SiC particles in the top 2 – 3 cm of the ingot.

Results from two ingots differ from each other by a factor 5 to 10, indicating the need for further experiments. Investigation of removal by settling should be studied separately from the pushing / engulfment process that takes place during casting.

Filtration of silicon with ceramic foam filters

The current study investigated the removal of inclusions from top-cut solar cell silicon scrap by filtration with ceramic foam filters. Inclusions in top-cut solar cell silicon scrap are needle-like Si_3N_4 particles and round SiC inclusions. A high filtration efficiency of more than 99% for 30 ppi SiC filters is achieved. In filtration with 30 ppi filters, no Si_3N_4 inclusions are found. The inclusions remaining are mainly SiC particles smaller than 10 μm. There are probably secondary inclusions formed during solidification. Experiments show that the filtration efficiency increases with decreasing filter pore size. Some filter cakes that mainly consist of large Si_3N_4 inclusions are found. They may entrap particles that come later by cake mode filtration. Since a high pressure drop can not be provided, cake filtration is not an alternative. Therefore inclusions must be removed by deep bed filtration. Si_3N_4 inclusions and most SiC particles attach directly to the inner walls of the filter and may even create bridges around the filter material. They will then favor entrapment of other inclusions by the filter.

Two mechanisms for the removal of inclusions by deep bed filtration are investigated. The main mechanisms that play a role in deep bed filtration seem to be interception and sedimentation (settling). Various models were considered to estimate removal efficiency of foam filters by these mechanisms. They include the isolated sphere model with potential flow and creeping flow, the constricted-tube model with creeping flow and a novel one here named branch model with potential flow.

The first conclusion that can be drawn after study of the models is that interception seems to be the main removal mechanism of inclusions in silicon. Settling appears to play a minor role for our system. It should be considered only in the isolated sphere model with creeping flow and in the constricted-tube model. The reason for such a weak affect of settling can be explained by the high melt velocity of molten silicon inside the filter which results in a very small collision probability attributable to settling ($= u_r/v$). Due to the low wetting angle between molten metal and the filter material, capillary forces drive the melt through the filter. Hence, good wetting of molten silicon with SiC filters ($\theta = 40°$) is the reason for the high velocity.

Among the models treated in this thesis, the proposed branch model gives the highest filtration efficiency, and agrees best with the experimental results. The single sphere model and the constricted-tube do not seem to apply successfully to filtration with high void fraction foam filters. The potential flow assumption is justified by the high melt velocity through the filter. High melt velocity increases the Reynolds number of the system which in turn decreases the boundary layer thickness thus approaching potential flow case. Potential flow gives a high removal efficiency.

A boundary layer thickness of say 7.5 μm will strongly reduce the removal efficiency of particles with size ≤ 7.5 μm. It is desired to remove inclusions in solar cell silicon down ≤ 1 μm. Smaller pore size filters should be used.

Wettability of molten silicon and contamination by graphite refractories

It is shown that molten silicon may be contaminated in contact with the refractories. Since purity for solar cell silicon is crucial, contamination must be minimized. Graphite crucibles may be a source of for relatively high levels of Al, Fe, and P.

Spreading and infiltration of molten silicon into the graphite substrates was investigated. Molten silicon does not initially wet carbon materials. However, due to the chemical reaction between Si and C, a SiC layer is formed in the interface between molten silicon and the graphite. Formation of this layer lowers the contact angles finally reaching equilibrium wetting angles of molten silicon with SiC materials. Spreading of molten silicon is affected not only by the reaction formed SiC layer, but also by the

surface finish. The final contact angles, also called equilibrium contact angles, decrease with increasing surface roughness of the graphites. For a smooth surface (R_a < 0.1 μm) the final contact angle is about 30° which is in agreement with the literature published. As the surface becomes rougher, the final contact angle decreases down to 0°.

Infiltration of silicon into graphites is mainly attributed to the average pore size of graphite materials. When molten silicon enters the pores, it reacts with carbon and forms SiC. After a time this SiC layer will block the pore. Materials with large pores are penetrated deeper by the liquid silicon. Zero contact angles of the silicon with graphites are found in materials with both high surface roughness and large average pore size.

These results indicate that graphites for use in the PV industry should have a small average pore size. The surface of the graphite in direct contact with silicon should be smooth (low roughness).

References

Abe, T., and Harada, H. (1986). *Nippon Kessho Seicho Gakkaishi*, 13(2-3), 122-130.

Acosta G, F. A., and Castillejos E, A. H. (2000a). "A Mathematical Model of Aluminum Depth Filtration with Ceramic Foam Filters: Part I. Validation for Short Term Filtration." *Metallurgical and Materials Transactions B*, 31B(June), 491-502.

Acosta G, F. A., and Castillejos E, A. H. (2000b). "A Mathematical Model of Aluminum Depth Filtration with Ceramic Foam Filters: Part II. Aplication to Long Term Filtration." *Metallurgical and Materials Transactions B*, 31B(June), 503-514.

Acosta G, F. A., Castillejos E, J. M., Almanza, R., and Flores V, A. (1995). "Analysis of Liquid Flow through Ceramic Porous Media Used for Molten Metal Filtration." *Metallurgical and Materials Transactions B*, 26B(February), 159-171.

Ahmad, R., and Marshall, R. I. (2004). "Controlling Inclusions Through Filtration in Investment Casting Process." *Proc. Pakistan Acad. Sci.*, 41(2), 121-128.

Ali, S., Mutharasan, R., and Apelian, D. (1985). "Physical Refining of Steel Melts by Filtration." *Metallurgical Transactions B*, 16B, 725-742.

Alkiviades C. Payatakes, C. T. R. M. T. (1973). "A new model for granular porous media: Part I. Model formulation." *AIChE Journal*, 19(1), 58-67.

Apelian, D., and Choi, K. K. (1988). "Metal Refining by Filtration." Foundry Process-Their Chemistry and Physics, S. Katz and C. F. Landefeld, eds., Plenum Press, New York-London, 467-494.

Bakke, P. (1992). "Filtration of Magnesium with Ceramic Foam Filters," NTNU, Trondheim.

Bakke, P., Engh, T. A., Bathen, E., Ã¸ymo, D., and Nordmark, A. (1994). "Magnesium Filtration with Ceramic Foam Filters and Subsequent Quantitative Microscopy of the Filters." *Materials and Manufacturing Processes*, 9(1), 111 - 138.

Bean, A. R., and Newman, R. C. (1971). "The solubility of carbon in pulled silicon crystals." *Journal of Physics and Chemistry of Solids*, 32(6), 1211-1219.

Bird, R. B., Stewart, W. E., and Lightfoot, E. N. (2007). *Transport Phenomena*, John Wiley & Sons, Inc.

Boettinger, W. J., and A. Warren, J. (1999). "Simulation of the cell to plane front transition during directional solidification at high velocity." *Journal of Crystal Growth*, 200(3-4), 583-591.

Bradford, S. A., Bettahar, M., Simunek, J., and van Genuchten, M. T. (2004). "Straining and Attachment of Colloids in Physically Heterogeneous Porous Media." *Vadose Zone J.*, 3(2), 384-394.

Braga, A. F. B., Moreira, S. P., Zampieri, P. R., Bacchin, J. M. G., and Mei, P. R. (2008). "New processes for the production of solar-grade polycrystalline silicon: A review." *Solar Energy Materials and Solar Cells*, 92(4), 418-424.

Bultman, J., and Geerligs, B. (2005). "Solar Grade Silicon: show stopper or infinite source." Solar Cell R&D Seminar, ECN.

Bune, A. V., Sen, S., Mukherjee, S., Catalina, A., and Stefanescu, D. M. (2000). "Effect of melt convection at various gravity levels and orientations on the forces acting on a large spherical particle in the vicinity of a solidification interface." *Journal of Crystal Growth*, 211(1-4), 446-451.

Buonassisi, T., Istratov, A. A., Pickett, M. D., Marcus, M. A., Ciszek, T. F., and Weber, E. R. (2006). "Metal precipitation at grain boundaries in silicon: Dependence on grain boundary character and dislocation decoration." *Applied Physics Letters*, 89, 042102-1-3.

Burganos, V. N., Paraskeva, C. A., Christofides, P. D., and Payatakes, A. C. (1994). "Motion and deposition of non-Brownian particles in upflow collectors." *Sep. Technol.*, 4, 47-54.

Cao, X., and Jahazi, M. (2005). "Examination and verification of the filtration mechanism of cake mode during the pressure filtration tests of liquid Al–Si cast alloys." *Materials Science and Engineering A*, 408, 234–242.

Catalina, A., Mukherjee, S., and Stefanescu, D. (2000). "A dynamic model for the interaction between a solid particle and an advancing solid/liquid interface." *Metallurgical and Materials Transactions A*, 31(10), 2559-2568.

Chithambaranadhan, D. (2005). "Refining of recycled PV-silicon by filtration," Norwegian University of Science and Technology, Trondheim.

Conti, C., and Netter, P. (1992). "Deep filtration of liquid metals: Application of a simplified model based on the limiting trajectory method." *Sep. Technol.*, 2(January), 46-56.

Dalaker, H. (2008). "The solubility of nitrogen in liquid silicon equilibrated with silicon nitride." SINTEF Materials and Chemistry, Trondheim.

Dalaker, H., and Tangstad, M. (2008). "The solubility of caron in liquid silicon and its dependence on the boron levels." NREL, ed., NREL, Vail, Colorado.

Davies, G., and Newman, R. C. (1994). "Carbon in Monocrystalline Silicon." Handbook of Semiconductors, T. S. Moss and S. Mahajan, eds., Elsevier Science, 1557-1635.

Davis, J. J., Rohatgi, A., Hopkins, R. H., Blais, P. D., Rai-Choudhury, P., McCormick, J. R., and Mollenkopf, H. C. (1980). "Impurities in Silicon Solar Cells." *IEEE Transactions on Electron Devices*, ED-27, 677-687.

Deike, R., and Schwerdtfeger, K. (1995). "Reactions between liquid silicon and different refractory materials." *Journal of Electrochemical Society*, 142(2), 609-614.

Dezellus, O., Jacques, S., Hodaj, F., and Eustathopoulos, N. (2005). "Wetting and infiltration of carbon by liquid silicon." *Journal of Materials Science*, 40, 2307–2311.

Dhindaw, B. (2000). "Materials science research in microgravity – Current status and an experimental case study." *Current Science*, 79(3), 341-347.

Dolloff, R. T. (1960). "Research study to determine the phase equilibrium relations of selected metal carbides at high temperatures." Pages: 28.

Du, G., Chen, N., and Rossetto, P. (2008). "On-wafer investigation of SiC and Si3N4 inclusions in multicrystalline Si grown by directional solidification." *Solar Energy Materials and Solar Cells*, 92(9), 1059-1066.

Durand, F., and Duby, J. (2000). "Solid-liquid equilibria in the silicon-rich corner of the Si-O-C system." *Journal of Phase Equilibria*, 21(2), 130-135.

Eikevik, T. K. (2008). "Kimdanning og vekst av silisiumkarbid i flytende Si for solcelleformål," NTNU, Trondheim.

Engh, T. A. (1992). "Removal of inclusions." Principle of Metal Refining, Oxford University Press, Oxford, New York, Tokyo, 219-279.

Engh, T. A. (2008). "Deep bed filtration." NTNU, Trondheim.

Engh, T. A. (2009). "A model of ceramic foam filters." NTNU, Trondheim.

Etzler, F. M. (2004). "Particle Size Analysis: A Comparison of Methods." Americal Pharmaceutical Review.

Eustathopoulos, N. (1998). "Dynamics of wetting in reactive metal/ ceramic systems." *Acta Materialia*, 46(7), 2319-2327.

Eustathopoulos, N., Nicholas, M. G., and Drevet, B. (1999). *Wettability at High Temperatures*, Pergamon.

Faber, T. E. (1995). *Fluid Dynamics for Physicists*, Press Syndicate of the University of Cambridge.

Fedkiw, P., and Newman, J. (1977). "Mass transfer at high Péclet numbers for creeping flow in a packed-bed reactor." *AIChE Journal*, 23(3), 255-263.

Fitzer, E., and Gadow, R. "Investigationsof the reactivity of different carbons with liquid silicon." *Proceedings of the International Symposioum on Ceramic Components for Engines*, Tokyo, Japan, 561-572.

Flamant, G., Kurtcuoglu, V., Murray, J., and Steinfeld, A. (2006). "Purificaiton of metallurgical grade silicon by a solar process." *Solar Energy Materials & Solar Cells*, 90, 2099-2106.

Fujiwara, K., Nakajima, K., Ujihara, T., Usami, N., Sazaki, G., Hasegawa, H., Mizoguchi, S., and Nakajima, K. (2002). "In situ observations of crystal growth behavior of silicon melt." *Journal of Crystal Growth*, 243(2), 275-282.

Gauckler, J. K., Waeber, M. M., Conti, C., and Jakob-Duliere, M. (1985). "Industrial Application of Open Pore Ceramic Foam for Molten Metal Filtration." Light Metals, The Metallurgical Society, 1261-1283.

Hall, R. N. (1958). "Electrical Contacts to Silicon Carbide." *Journal of Applied Physics*, 29(6), 914-917.

Han, Q., and Hunt, J. D. (1995). "Redistribution of Particles during Solidification." *ISIJ Int.*, 35(6), 693-699.

Hari Rao, C. V., Bates, H. E., and Ravi, K. V. (1976). "Electrical effects of SiC inclusions in EFG silicon ribbon solar cells." *Journal of Applied Physics*, 47(6), 2614-2619.

Harker, J. H., Coulson, J. M., Backhurst, J. R., and Richardson, J. F. (2002). *Chemical Engineering*, Elsevier Science & Technology.

Hecht, U., and Rex, S. (1997). "On the transition from pushing to engulfment during directional solidification of the particle-reinforced aluminum-based metal-matrix composite 2014 + 10 Vol Pct Al2O3." *Metallurgical and Materials Transactions A*, 28(3), 867-874.

Herrmann, M., and Goeb, O. (2001). "Colour of gas-pressure-sintered silicon nitride ceramics Part I. Experimental data." *Journal of the European Ceramic Society*, 21, 303-314.

Hubschen, B., Kruger, J. G., Keegan, N. J., and Schneider, W. (2000). "A new approach for the investigation of the fluid flow in ceramic foam filters." Light Metals 2000, TMS, 809-815.

Hull, R. (1999). *Properties of Crystalline Silicon*, INSPEC, The Institution of Electrical Engineers, London.

Iguchi, Y., and Narushima, T. (1993). "Solubility of oxygen, nitrogen and carbon in liquid silicon." First International Conference on Processing Materials for Properties, TMS, ed., TMS, 437-440.

Istratov, A. A., Buonassisi, T., Pickett, M. D., Heuer, M., and Weber, E. R. (2006). "Control of metal impurities in "dirty" multicrystalline silicon for solar cells." *Materials Science and Engineering: B*, 134(2-3), 282-286.

Jackson, K. A. (2004). "Constitutional supercooling surface roughening." *Journal of Crystal Growth*, 264(4), 519-529.

Juel, M. (2008). "Refining of solar grade silicon by directional solidification." NTNU, Trondheim.

Juel, M., Øvrelid, E., Bellmann, M., and Tuffour, B. (2008). "Refining of solar grade silicon by directional solidification." Norwegian-German group seminar on solar cell materials, NTNU, Trondheim.

Juretzko, F., Stefanescu, D., Dhindaw, B., Sen, S., and Curreri, P. (1998). "Particle engulfment and pushing by solidifying interfaces: Part 1. Ground experiments." *Metallurgical and Materials Transactions A*, 29(6), 1691-1696.

Kaiser, W., and Thurmond, C. D. (1959). "Nitrogen in Silicon." *Journal of Applied Physics*, 30(3), 427-431.

Kaptay, G. (2001). "Interfacial criterion of spontaneous and forced engulfment of reinforcing particles by an advancing solid/liquid interface." *Metallurgical and Materials Transactions A*, 32(4), 993-1005.

Keegan, N. J., Schneider, W., and Krug, H. P. "Evaluation of the Efficiency of Fine Pore Ceramic Foam Filters." *Light Metals 1999*, 1031-1041.

Kim, J. K., and Rohatgi, P. K. (1998). "Interaction between moving cellular solidification front and graphite particles during centrifugal casting." *Materials Science and Engineering A*, 244(2), 168-177.

Kocaefe, D., Murray-Chiasson, A., Kocaefe, Y., and Waite, P. (2004a). "Modelling of Inclusion Re-entrainment During Filtration." *The Canadian Journal of Chemical Engineering*, 82, 1191-1201.

Kocaefe, D., Murray-Chiasson, A., Kocaefe, Y., and Waite, P. (2004b). "Study of Inclusion Re-Entrainment in a Filter Bed." *Metallurgical and Materials Transactions B*, 35B, 999-1009.

Koch, W., Endros, A. L., Franke, D., Haessler, C., Kalejs, J. P., and Moeller, H. J. (2003). "Bulk crystal growth and wafering for PV." Handbook of Photovoltaic Science and Engineering, A. Luque and S. Hegedus, eds., Wiley, 205-254.

Kolbesen, B. O., and Mühlbauer, A. (1982). "Carbon in silicon: Properties and impact on devices." *Solid-State Electronics*, 25(8), 759-775.

Kurz, W., and Fisher, D. J. (1989). *Fundamentals of Solidification*, Trans Tech Aedermannsdorf, Switzerland.

Kvande, R. (2008). "Incorporation of Impurities during Directional Solidification of Multi-crystalline Silicon for Solar Cells," Norwegian University of Science and Technology, Trondheim.

Kvande, R., Mjøs, Ø., and Ryningen, B. (2005). "Growth rate and impurity distribution in multicrystalline silicon for solar cells." *Materials Science and Engineering: A*, 413-414, 545-549.

Laé, E., Duval, H., Rivière, C., Le Brun, P., and Guillot, J. B. "Experimental and Numerical Study of Ceramic Foam Filtration." *Light Metals 2006*, 753-758.

Landry, K., Rado, C., and Eustathopoulos, N. (1996). "Influence of interfacial reaction rates on the wetting driving force in metal/ceramic systems." *Metallurgical and Materials Transactions A*, 27(10), 3181-3186.

Landry, K., Rado, C., Voitovich, R., and Eustathopoulos, N. (1997). "MECHANISMS OF REACTIVE WETTING: THE QUESTION OF TRIPLE LINE CONFIGURATION." *Acta Materialia*, 45(7), 3079-3085.

Lee, J., and Koplik, J. (2001). "Network model for deep bed filtration." *Physics of Fluids*, 13(5), 1076-1086.

Leipold, M. H., O'Donnell, T. P., and Hagan, M. A. (1980). "Materials of construction for silicon crystal growth." *Journal of Crystal Growth*, 50(1), 366-377.

Li, J.-G., and Hausner, H. (1995). "Wetting and infiltration of graphite materials by molten silicon." *Scripta Metallurgica et Materialia*, 32(3), 377-382.

Li, J.-G., and Hausner, H. (1996). "Reactive Wetting in the Liquid-Silicon/Solid-Carbon System." *Journal of American Ceramic Society*, 79(4), 873-880.

Li, J. G., and Hausner, H. (1991). "Wettability of silicon carbide by gold, germanium and silicon " *Journal of Materials Science Letters*, 10, 1275-1276.

Li, J. G., and Hausner, H. (1992). "Influence of Oxygen Partial Pressure on the Wetting Behaviour of Silicon Nitride by Molten Silicon." *Journal of the European Ceramic Society*, 9, 101-105.

Ludwig, A., and Kurz, W. (1996). "Direct observation of solidification microstructures around absolute stability." *Acta Materialia*, 44(9), 3643-3654.

Mjøs, Ø. (2006). "Directional Solidification of Silicon for Solar Cells," NTNU, Trondheim.

Moeller, H. J., Wuerzner, S., Bellmann, M., and Scholz, S. (2008). "Improving solar grade silicon by controlling extended defect generation and foreign atomic defect interactions." NTNU, Trondheim.

Mukai, K., and Yuan, Z. (2000). "Wettability of ceramics with molten silicon at temperatures ranging from 1693 to 1773 K." *Materials Transactions, JIM*, 41(2), 338-345.

Mukherjee, S., Sharif, M., and Stefanescu, D. (2004). "Liquid convection effects on the pushing-engulfment transition of insoluble particles by a solidifying interface: Part II. Numerical calculation of drag and lift forces on a particle in parabolic shear flow." *Metallurgical and Materials Transactions A*, 35(2), 623-629.

Mukherjee, S., and Stefanescu, D. (2004). "Liquid convection effects on the pushing-engulfment transition of insoluble particles by a solidifying interface: Part I. Analytical calculation of the lift forces." *Metallurgical and Materials Transactions A*, 35(2), 613-621.

Naidich, Y. V. (1981). "The wettability of solids by liquid metals." *Progress in Surface and Membrane Science*, 14, 353-484.

Naidich, Y. V., Zhuravlev, V., and Krasovskaya, N. (1998). "The wettability of silicon carbide by Au – Si alloys." *Materials Science and Engineering A*, 245, 293–299.

Narushima, T., Ueda, N., Takeuchi, S., Ishii, F., and Iguchi, Y. (1994). "Nitrogen Solubility in Liquid Silicon." *Materials Transactions, JIM*, 35(11), 821-826.

Narushima, T., Yamashita, A., Ouchi, C., and Iguchi, Y. (2002). "Solubilities and Equilibrium Distribution Coefficients of Oxygen and Carbon in Silicon." *Materials Transactions*, 43(8), 2120-2124.

Newman, R. C. (1996). "Light impurities and their interactions in silicon." *Materials Science and Engineering B*, 36(1-3), 1-12.

Ni, H., Yu, Z., Mingyu, H., Weibiao, G., and Sun, B. (2006). "Purifying effects and mechanism of a new composite filter." *Materials Science and Engineering A: Structural Materials: Properties, Microstructure and Processing (2006)*, A426(1-2), 53-58.

Nikolopoulos, P., Agathopoulos, S., Angelopoulos, G. N., Naoumidis, A., and Grobmeier, H. (1992). "Wettability and interfacial energies in SiC-liquid metal systems." *Journal of Materials Science*, 27, 139-145.

Nozaki, T. (1974). "Behavior of light impurity elements in the production of semiconductor silicon." *Journal of Radioanalytical Chemistry*, 19(1), 109-128.

Nozaki, T., Yatsurugi, Y., and Akiyama, N. (1970). "Concentration and Behavior of Carbon in Semiconductor Silicon." *Journal of The Electrochemical Society*, 117(12), 1566-1568.

Oden, L., and McCune, R. (1987). "Phase equilibria in the Al-Si-C system." *Metallurgical and Materials Transactions A*, 18(12), 2005-2014.

Ottem, L. (1993). "Løselighet og termodynamiske data for oksygen og karbon i flytende legeringer av silisium og ferrosilisium." SINTEF, Trondheim.

Pampuch, R., Walasek, E., and Bialoskórski, J. (1986). "Reaction mechanism in carbon-liquid silicon systems at elevated temperatures." *Ceramics International*, 12(2), 99-106.

Payatakes, A. C., Tien, C., and Turian, R. M. (1973a). "A new model for granular porous media: Part I. Model formulation." *AIChE Journal*, 19(1), 58-67.

Payatakes, A. C., Tien, C., and Turian, R. M. (1973b). "A new model for granular porous media: Part II. Numerical solution of steady state incompressible Newtonian flow through periodically constricted tubes." *AIChE Journal*, 19(1), 67-76.

Pendse, H., Chiang, H.-w., and Tien, C. (1983). "Analysis of transport processes with granular media using the constricted tube model." *Chemical Engineering Science*, 38(8), 1137-1150.

Pendse, H., and Tien, C. (1982). "General correlation of the initial collection efficiency of granular filter beds." *AIChE Journal*, 28(4), 677-686.

Raiber, K., Hammerschmid, P., and Janke, D. (1995). "Experimental Studies on Al2O3 Inclusion Removal from Steel Melts Using Ceramic Filters." *ISIJ Int.*, 35(4), 380-388.

Rawle, A. (2008). "Basic Principles of Particle Size analysis." Select Science, 1-8.

Rhim, W.-K., and Ohsaka, K. (2000). "Thermophysical properties measurement of molten silicon by high-temperature electrostatic levitator: density, volume expansion, specific heat capacity, emissivity, surface tension and viscosity." *Journal of Crystal Growth*, 208(1-4), 313-321.

Rutter, J. W., and Chalmers, B. (1953). "A prismatic substructure formed during solidification of metals." *Canadian Journal of Physics*, 31, 15-39.

Ryningen, B. (2008). "Formation and growth of crystal defects in directionally solidified multicrystalline silicon for solar cells," NTNU, Trondheim.

Ryningen, B., Sultana, K. S., Stubhaug, E., Lohne, O., and Hjemås, P. C. (2008). "Dislocation Clusters in Multicrystalline Silicon." NTNU, Trondheim.

Raaness, M. P. (2005). "Electron probe micro analyzer (EPMA)." NTNU - EM Lab, Trondheim.

Safarian-Dastjerdi, J. (2007). "Kinetics and Mechanisms of Reduction of MnO-Containing Silicate Slags by Selected Forms of Carbonaceous Materials," NTNU, Trondheim.

Sarasin. (2008). "Solar industry – Stormy weather will give way to sunnier periods." Bank Sarasin, Basel.

Sarti, D., and Einhaus, R. (2002). "Silicon feedstock for the multi-crystalline photovoltaic industry." *Solar Energy Materials & Solar cells*, 72, 27-40.

Sasaki, H., Tokizaki, E., Huang, X. M., Terashima, K., and Kimura, S. (1995). "Temperature dependence of the viscosity of molten silicon measured by the oscillating cup method." *Japanese Journal of Applied Physics, Part 1: Regular Papers, Short Notes & Review Papers* 34(7A), 3432-3436.

Sato, Y., Kameda, Y., Nagasawa, T., Sakamoto, T., Moriguchi, S., Yamamura, T., and Waseda, Y. (2003). "Viscosity of molten silicon and the factors affecting measurement." *Journal of Crystal Growth*, 249(3-4), 404-415.

Scace, R. I., and Slack, G. A. (1959). "Solubility of Carbon in Silicon and Germanium." *The Journal of Chemical Physics*, 30(6), 1551-1555.

Schvezov, C. E., and Weinberg, F. (1985). "Interaction of iron particles with a solid-liquid interface in lead and lead alloys." *Metallurgical Transactions B*, 16(2), 367-375.

Sen, S., Juretzko, F., Stefanescu, D. M., Dhindaw, B. K., and Curreri, P. A. (1999). "In situ observations of interaction between particulate agglomerates and an advancing planar solid/liquid interface: microgravity experiments." *Journal of Crystal Growth*, 204(1-2), 238-242.

Shangguan, D., Ahuja, S., and Stefanescu, D. (1992). "An analytical model for the interaction between an insoluble particle and an advancing solid/liquid interface." *Metallurgical and Materials Transactions A*, 23(2), 669-680.

Sharafat, S., Ghoniem, N., Sawan, M., Ying, A., and Williams, B. (2006). "Breeder foam: an innovative low porosity solid breeder material." *Fusion Engineering and Design*, 81(1-7), 455-460.

Sharon M. Snorek, J. F. B. N. C. W. H. D. E. P. D. F. M. E. R. N. K. J. J. L. R. L. M. H. (2007). "PQRI recommendations on particle-size analysis of drug substances used in oral dosage forms." *Journal of Pharmaceutical Sciences*, 96(6), 1451-1467.

Shekunov, B., Chattopadhyay, P., Tong, H., and Chow, A. (2007). "Particle Size Analysis in Pharmaceutics: Principles, Methods and Applications." *Pharmaceutical Research*, 24(2), 203-227.

Singh, M., and Behrendt, D. R. (1992). "Studies on the reactive melt infiltration of silicon and silicon-molybdenum alloys in porous carbon." United States, Pages: (11 p).

Snorek, S. M., Bauer, J. F., Chidambaram, N., Doub, W. H., Duffy, E. P., Etzler, F. M., Kelly, R. N., Lane, J. J., Mueller, R. L., Prasanna, H. R., Pujara, C. P., Reif, V. D., Scarlett, B., Stowell, J. G., and Toma, P. H. (2007). "PQRI recommendations on particle-size analysis of drug substances used in oral dosage forms." *Journal of Pharmaceutical Sciences*, 96(6), 1451-1467.

Stefanescu, D., Dhindaw, B., Kacar, S., and Moitra, A. (1988). "Behavior of ceramic particles at the solid- liquid metal interface in metal matrix composites." *Metallurgical and Materials Transactions A*, 19(11), 2847-2855.

Stefanescu, D., Juretzko, F., Catalina, A., Dhindaw, B., Sen, S., and Curreri, P. (1998). "Particle engulfment and pushing by solidifying interfaces: Part II. Microgravity experiments and theoretical analysis." *Metallurgical and Materials Transactions A*, 29(6), 1697-1706.

Stein, H. J. "A perspective on nitrogen in silicon." *Materials Research Society Symposium Proceedings*, 15-16.

Stokkan, G. (2004). "Characterisation of Multicrystalline Silicon Solar Cells; Development of characterisation method for the combined effect of dislocations and grain boundaries on the minority carrier lifetime," NTNU, Trondheim.

Stølen, S., and Grande, T. (2004). "Surfaces, Interfaces and Adsorbtion." Chemical Thermodynamics of Materials: Macroscopic and Microscopic Aspects, John Wiley and Sons Ltd, 171-172.

Swanson, R. M. "Developments in Silicon Solar Cells." *Electron Devices Meeting, 2007. IEDM 2007. IEEE International*, 359-362.

Syvertsen, M., Frisvold, F., Engh, T. A., and Voss, D. S. "Development of a Compact Deep Bed Filter for Aluminium." *Light Metals 1999*, 1049-1055.

Søiland, A. K. (2004). "Silicon for Solar Cells," NTNU, Trondheim.

Søiland, A. K., Øvrelid, E. J., Engh, T. A., Lohne, O., Tuset, J. K., and Gjerstad, Ø. (2004). "SiC and Si3N4 inclusions in multicrystalline silicon ingots." *Materials Science in Semiconductor Processing*, 7, 39-43.

Tien, C., and Ramarao, B. V. (2007). *Granular Filtration of Aerosols and Hydrosols*, Elsevier, Amsterdam.

Uemura, K.-i., Takahashi, M., Koyama, S., and Nitta, M. (1992). "Flltration Mechanismof Non-metallic Inclusions In Steel by Ceramic Loop Filter." *ISIJ International,*, 32(1), 150-156.

Vassallo, P., and Symolon, P. (2008). "Friction Factor Measurements in an Equally Spaced Triangular Array of Circular Tubes." *Journal of Fluids Engineering*, 130(4), 041105-5.

Venkatesan, M., and Rajagopalan, R. (1980). "A hyperboloidal constricted tube model of porous media." *AIChE Journal*, 26(4), 694-698.

Whalen, T. J., and Anderson, A. T. (1975). "Wetting of silicon carbide, silicon nitride, and carbon by silicon and binary silicon alloys." *Journal of the American Ceramic Society*, 58(9-10), 396-399.

Wieser, P. F. (1988). "Filtration of Irons and Steels." Foundry Process-Their Chemistry and Physics, S. Katz and C. F. Landefeld, eds., Plenum Press, New York-London, 495-512.

Wyers, G. P. (2007a). "Photovoltaics: an overview of technologies and market potentials." ECN Solar Energy, 3.

Wyers, P. (2007b). "The PV Roadmap and Prospects for Silicon Technology." ECN Solar Energy.

Wærnes, A. N., Raaness, O. S., Øvrelid, E. J., Geerligs, L. J., Wyers, G. P., Santén, S., and Wiersma, B. (2005). "New Feedstock Materials." Freiberg Solartage, ECN, Freiberg, Germany, 5.

Yanaba, K., Matsumura, Y., Narushima, T., and Iguchi, Y. (1998). "Effect of Alloying Elements on Carbon Solubility in Liquid Silicon Equilibrated with Silicon Carbide." *Materials Transactions, JIM*, 39(8), 819-823.

Yatsurugi, Y., Akiyama, N., Endo, Y., and Nozaki, T. (1973). "Concentration, Solubility, and Equilibrium Distribution Coefficient of Nitrogen and Oxygen in Semiconductor Silicon." *Journal of The Electrochemical Society*, 120(7), 975-979.

Yuan, Z., Huang, W. L., and Mukai, K. (2004). "Wettability and reactivity of molten silicon with various substrates." *Applied Physics A – Materials Science & Processing*, 78, 617–622.

Yupko, V. L., and Gnesin, G. G. (1973). "Contact interaction of silicon carbide with liquid silicon." *Poroshkovaya Metallurgiya*, 13(10), 97-101.

Zhou, H., and Singh, R. N. (1995). "Kinetics Model for the Growth of Silicon Carbide by the Reaction of Liquid Silicon with Carbon " *Journal of American Ceramic Society*, 78(9), 2456-2462.

Zhou, M., Shu, D., Li, K., Zhang, W. Y., Ni, H. J., Sun, B. D., and Wang, J. (2003). "Deep Filtration of Molten Aluminum using Ceramic Foam Filters and Ceramic Particles with Active Coatings." *Metallurgical and Materials Transactions A*, 34A(May), 1183-1191.

Øvrelid, E., Geerligs, B., Wærnes, A., Raaness, O., Solheim, I., Jensen, R., Tang, K., Santeen, S., and Wiersma, B. (2006). "Solar Grade Silicon by a Direct Metallurgical Process." Silicon for the Chemical Industry VIII, Trondheim, Norway.